BILINGUAL PUBLISHING CO.
Pioneer of Global Academics Since 1984

Journal of Atmospheric Science Research

Volume 5 • Issue 4 • October 2022 ISSN 2630-5119(Online)

Volume 5 Issue 4 • October 2022 • ISSN 2630-5119 (Online)

Journal of Atmospheric Science Research

BILINGUAL PUBLISHING CO.
Pioneer of Global Academics Since 1984

BILINGUAL PUBLISHING CO.
Pioneer of Global Academics Since 1984

Volume 5 | Issue 4 | October 2022 | Page1-49
Journal of Atmospheric Science Research

Contents

Articles

BILINGUAL PUBLISHING CO.
Pioneer of Global Academics Since 1984

Journal of Atmospheric Science Research
https://ojs.bilpublishing.com/index.php/jasr

ARTICLE

Forage Monitoring and Prediction Model for Early Warning Application over the East of Africa Region

Jully Ouma[1,2*] Dereje Wakjira[2] Ahmed Amdihun[3] Eva Nyaga[2] Franklin Opijah[1] John Muthama[1] Viola Otieno[3] Eugene Kayijamahe[3] Solomon Munywa[2] Guleid Artan[3]

1. Department of Meteorology, University of Nairobi, 30197 - 00100, Nairobi, Kenya
2. IGAD Centre for Pastoral Areas and Livestock Development (ICPALD), 47824 - 00100, Nairobi, Kenya
3. IGAD Climate Prediction and Applications Centre (ICPAC), 10304 - 00100, Nairobi, Kenya

ARTICLE INFO

Article history
Received: 18 June 2022
Accepted: 21 September 2022
Published Online: 8 October 2022

Keywords:
Prediction
Forage biomass
Rangelands
Pastoralism
Early warning
East Africa

ABSTRACT

Rangelands dominate arid and semi-arid lands of the Greater Horn of Africa (GHA) region, whereby pastoralism being the primary source of livelihood. The pastoral livelihood is affected by the seasonal variability of pasture and water resources. This research sought to design a grid-based forage monitoring and prediction model for the cross-border areas of the GHA region. A technique known as Geographically Weighted Regression was used in developing the model with monthly rainfall, temperature, soil moisture, and the Normalized Difference Vegetation Index (NDVI). Rainfall and soil moisture had a high correlation with NDVI, and thus formed the model development parameters. The model performed well in predicting the available forage biomass at each grid-cell with March-May and October-December seasons depicting a similar pattern but with a different magnitude in ton/ha. The output is critical for actionable early warning over the GHA region's rangeland areas. It is expected that this mode can be used operationally for forage monitoring and prediction over the eastern Africa region and further guide the regional, national, sub-national actors and policymakers on issuing advisories before the season.

1. Introduction

The Greater Horn of Africa (GHA) region is one of the regions in the world that are most vulnerable to climate change and extreme climate events. This is particularly so in the arid and semi-arid lands (ASALs). The ASALs are dominated by rangelands home to pastoralist and agro-pastoralist communities who are dependent on livestock for their livelihoods. It receives a bimodal rainfall pattern, that is, March to May (MAM), known as the long rain season [1], and October to December (OND) as the short rain season. These rainfall seasons are mostly modulated by the Inter-Tropical Convergence Zone (ITCZ) [1-3].

*Corresponding Author:
Jully Ouma,
Department of Meteorology, University of Nairobi, 30197 - 00100, Nairobi, Kenya; IGAD Centre for Pastoral Areas and Livestock Development (ICPALD), 47824 - 00100, Nairobi, Kenya;
Email: jully.ouma@gmail.com

DOI: https://doi.org/10.30564/jasr.v5i4.4809

The rainfall variability over the GHA region has also been linked to the variability of the sea surface temperatures over Tropical Pacific and Western Indian Ocean basins [4-7]. The two rainy seasons are followed by a dry season, characterized by a shortage of natural forage/pasture and water resources, especially if a season's rainfall (amount and distribution) is below the long-term average. Consequently, reducing animal feeds availability within the rangelands in the region affects the livestock sector's operation and sustainability [8]. This further impact severely the pastoral livelihood, thus the need for natural pasture forage prediction for an effective Early Warning System (EWS).

The GHA region remains the largest producer of traditional livestock globally [9], with major export of animals to the Middle East countries and Gulf States [10]. Livestock in this region is the primary source of livelihood [11,12] and is currently experiencing several challenges due to scarcity of water and feed. Governments have reduced the grazing areas within the rangelands through the creation of conservation schemes, game reserves, and national parks [11]. This restricts seasonal mobility and prevents pastoralists from accessing these areas, which leads to conflict with the security personnel during the period of scarcity. Non-Governmental Organizations (NGOs) operating in ASALs also introduced crop cultivation in the pastoral range areas, which deprived pastoralists of valuable pasture [11]. In addition to these challenges is drought, which is the significant devastating hazard over the GHA region that depletes pasture and widespread death of livestock and humans in extreme cases [10,12]. Hence, it is critical to manage and monitor the remaining grazing areas for pastoral communities in the region.

Seasonal livestock mobility is central in the pastoralist way of life [10], and such mobility largely disregards national and international boundaries. Their seasonal movement is mainly dictated by climate conditions which affect pasture and water availability, and sociocultural conditions [10,11]. The seasonal movement is critical in terms of ecosystem preservation and sustainable use of pastoral resources over the ASALs. For example, transhumant pastoralists within Kenya and Ethiopia's cross-border area are influenced by the rainfall pattern, causing them to live half of the year in Kenya and the other half in Ethiopia [11]. Pastoralist mobility sometimes induces conflict related to resource use, and the conflicts intensify during the periods of drought and famine [10-12]. Thus, areas with permanent pasture need to be identified and managed to act as a safety net for pastoralists during the periods of drought in the ASALs. Managed dry season grazing combined with forage prediction will help in early action before a major catastrophe in the ASALs of the region. This is critical as a shrink in natural pasture can worsen conflicts in the region.

Opio [8] gives the current practice in the livestock sector within the East Africa region. The paper formulated a feed resource sharing plan across communities and countries where the pastoralist faces similar challenges. This plan is critical in resilience building for the livestock sector in the Horn of Africa [8], which can improve significantly with the incorporation of fodder/forage prediction for early warning. The work of range fodder early warning in some of the Inter-Governmental Authority on Development (IGAD) Member States so far depends on instant rangeland feed assessment, without projection into the future, which has a limitation in providing advance early warning for preparedness and response. The Kenyan National Drought Management Authority (NDMA) monitors drought in the ASALs of the country through the Standardized Precipitation Index (SPI) [13,14] and Vegetation Condition Index (VCI) [14,15]. This only gives the state of situations, reporting time, in the counties without anticipating the future using climatic conditions. Thus, in most cases reactive measures are taken instead of proactive measures.

Matere [14] attempted to develop a Predictive Livestock Early Warning System (PLEWS) for Kenya in terms of forage status. This is an upgrade of the Livestock Early Warning System known as LEWS [16]. The PLEWS use PHYGROW (Phytomass Growth Model) model and the Auto-Regressive Integrated Moving Averages (ARIMA) model with a moving average to forecast forage condition. This is still at a pilot stage, and it is worth noting that the PHYGROW model used is not freely available. This system's output is based on administrative boundaries [14], which is a limitation since vegetation/forage condition knows no political boundary. Climate as a driver of vegetation condition should be considered in forage prediction [17,18] which is not the case in the used ARIMA model.

Rainfall over time has been documented as a variable for predicting forage in rangelands [17,19] due to the strong correlation between rainfall and the Normalized Difference Vegetation Index (NDVI) [17] with NDVI being the dependent variable. While confirming the strong relationship, Georganos [18] indicated that the relationship is somewhat complex and non-linear. Thus, for modeling, there is a need to develop a regression model that allows the relationship between rainfall, temperature, soil moisture, and NDVI to vary in space other than traditional Ordinary Least Squares (OLS) regression [18]. The development of the forage prediction model in this study is based on the Gray System theory [20], which solves a time-varying non-linear system [21-23]. It provides an approach to investigate the input-output process's relationships with unclear inner relationships, uncertain mechanisms, and insufficient information [22,23]. This technique will be used in achieving the research objective which is to design and customize a grid-based prototype rangeland feed monitoring and prediction system for the cross-border areas of the GHA region.

2. Material and Methods

2.1 Study Area

The study covers transboundary areas along Ethiopia, Kenya, Somalia, South Sudan, and Uganda borders. These areas are known as Karamoja Cluster (along Uganda, South-Sudan, Kenya, Ethiopia border), also known as IGAD Cluster 1; IGAD's Cluster 2 and 3 (cross-border area shared by Kenya, Ethiopia, and Somalia). The clusters specifically cover the districts in the Karamoja region of Uganda; West Pokot, Turkana, Marsabit, Wajir, and Mandera counties in Kenya; South Omo, Borana, and Liben Zones in Ethiopia; and Gedo region in Somalia (Figure 1). Much of the study area is covered by shrubs and grassland, which defines the area as a pastoral zone (Figure 1). The study area receives a similar rainfall pattern in two seasons: March to May and October to December. This rainfall pattern and amount directly link to vegetation distribution over the study area.

2.2 Data Source

The datasets used in the study were: land cover (LC), NDVI, rainfall, temperature, soil moisture, and livestock mobility. The administrative boundary data used in the study were taken from the Global Administrative boundary (GADM) database (www.gadm.org), version 3.4. The LC data adopted here are the "S2 prototype LC map at 20 m of Africa 2016" released by the European Space Agency (ESA) on the 2nd of October 2017 (https://www.esa-landcover-cci.org/). Climatic and environmental datasets, i.e. rainfall and NDVI, were obtained from the IGAD Climate Prediction and Applications Centre (ICPAC). ICPAC is a specialized institution of IGAD located in Nairobi-Kenya with the mandate of providing climate related services to eleven-member countries.

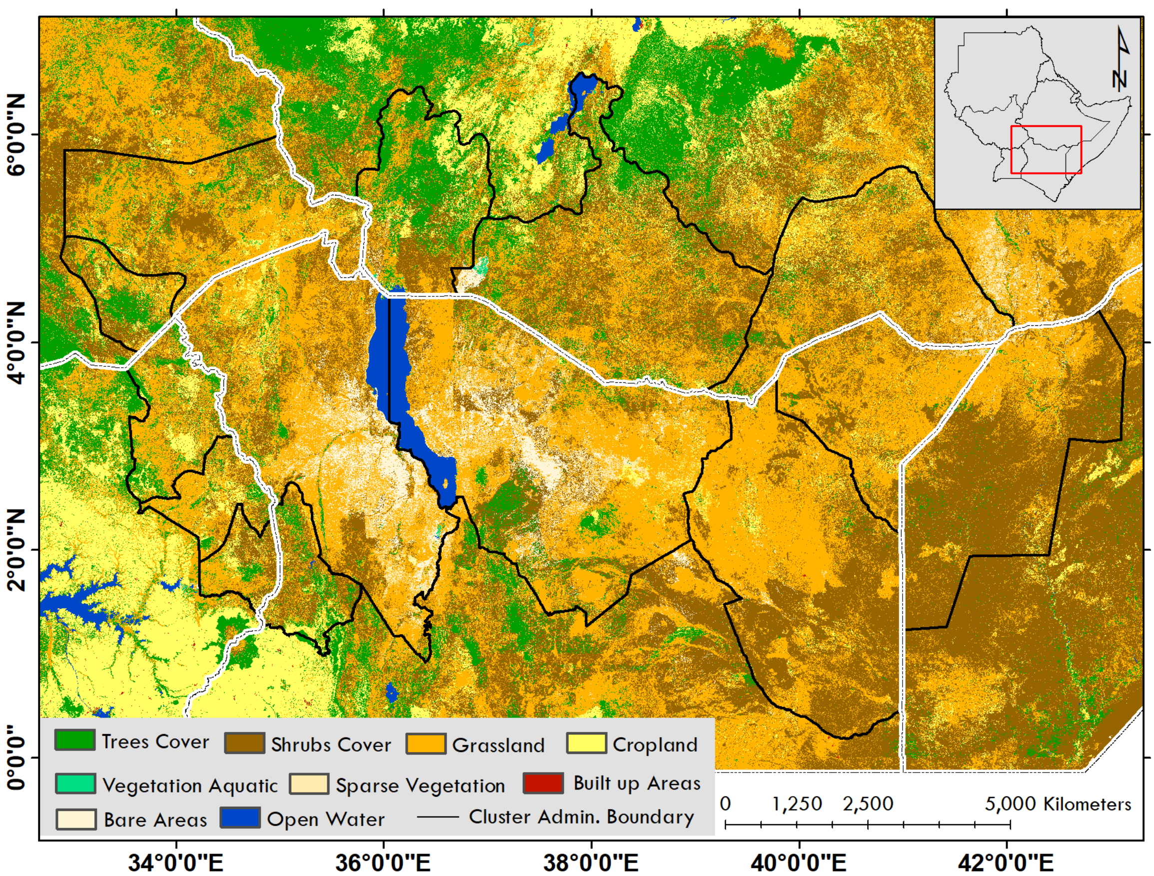

Figure 1. Land cover types over the study area, which covers the IGAD Cluster 1 (cross border area shared by Uganda, South-Sudan, Kenya and Ethiopia), IGAD Clusters 2 and 3 (cross-border area shared by Kenya, Ethiopia, and Somalia)

The NDVI data was available from 1999 to the near-present (http://gmes.icpac.net/data-center) at a spatial resolution of 0.01° and monthly temporal resolution. This is preferred over MODIS data since they are cloud-free [17] and used as an indicator for biomass production. Rainfall data known as Climate Hazards Group InfraRed Precipitation with Station data (CHIRPS) monthly dataset [24] was obtained from the ICPAC database at a spatial resolution of 0.05°. The dataset is available from 1981 to the near present, originally from the Climate Hazard Group (CHG). This dataset has been used over the region in past studies and shown to perform well [24-27]. Temperature is a variable that does not significantly vary in space and was obtained from the National Oceanic and Atmospheric Administration (NOAA) database, with a spatial resolution of 0.05° at a monthly temporal resolution from 1948 to near present. Soil Moisture data adopted here is the Soil Moisture Active Passive (SMAP) data from the National Aeronautics and Space Administration (NASA) database launched in January 2015 [28]. The SMAP covers have a global extent and can be obtained at 3 km spatial resolution [28].

2.3 Methods

As a prerequisite for modeling, all the datasets were grouped into three sets, that is, fifteen years for model development (1999-2013), four years to bias correct the model (2014-2017), and the remaining two years for model validation (2018-2019) at a seasonal time scale. This is because livestock mobility is based on seasonal rainfall. These seasons are March-May (MAM), which has the highest amount of rainfall over the study area, thus more forage production, and October-December (OND), known as the short rain season. These datasets were subjected to a multicollinearity test which is a critical step before developing a model with more than one independent variable. The collinearity test helps improve model performance and has been used and discussed in several studies [29-32].

An experimental technique known as Geographically Weighted Regression (GWR) was used in developing a prototype rangeland feed prediction model. The GWR technique is preferred over the Ordinary Linear Regression (OLR) method due to its capability of examining the existence of spatial non-stationarity in the relationship between a dependent variable and a set of independent variables [18,33-35]. This technique is fully described by Fotheringham [33]. This method allows estimation of the local parameter by considering the location of observation as shown by the equation below;

$$\boldsymbol{y_i = a(u_i, v_i) + b(u_i, v_i)x_i + \varepsilon_i, \quad i = 1 : n}$$

In the model above, the coordinates of location $\boldsymbol{i}$ are represented by $\boldsymbol{ui, vi}$ while $\boldsymbol{a}$ and $\boldsymbol{b}$ are local parameters to be estimated, particularly at location $\boldsymbol{i}$ [18]. In brief, the technique uses a moving window over the data, estimating one set of coefficient values at every chosen "fit" point [36]. The fit points are often the grid points at which observations were made, and if the local coefficients vary in space, it is taken as an indication of non-stationarity [37]. The prediction model's output was converted to total forage biomass using the technique described by Hobbs [38] and its output in Kg/ha. The unit was then converted to tonnes per hectare (ton/ha) i.e. 1 ton/ha = 1000 kg/ha. Available forage biomass was computed from the total forage biomass using a factor presented by Toxopeus [39] as in the equation below.

Available Forage = Total.Forage.Biomass * 45%

2.3.1 Model Skill Assessment and Validation

The "eyeball" method is still the most commonly used method in spatial verification [40] and was adopted in this study to compare the results side by side and uses human judgment to discern forecast errors. However, this method is not quantitative [40]. In addition to this, quantitative methods were also used in model skill assessment, i.e., the Mean Error (ME) also known as bias and Relative Mean Absolute Error (RMAE). Both of these methods estimate the average prediction error [35], and give a perfect score when the value is zero [41]. Reliability diagram [42] also known as attribute diagram was used to determine the model's skill. A model's reliability is indicated by the proximity of the plotted curve to the diagonal line [42-44]. The deviation of this curve from the diagonal line gives a conditional bias. If the curve lies below the diagonal line, this indicates over-prediction; but above the line means under-prediction.

3. Results and discussion

3.1 Result from the Multicollinearity Test

A multicollinearity test on the dataset was done at each grid point for the two seasons (MAM and OND) using the diagnostic test. The result of the diagnostic test was then subjected to the variance inflation factor (VIF) with a cut point of 2.5 to determine collinearity and the Klein rule to give the location of collinearity. The results (Table 1) show no multicollinearity in the dataset, hence no need for data filtering.

In addition to this, seasonal rainfall and soil moisture were well correlated spatially with maximum NDVI over the study area for the two seasons. Few places had a negative correlation, especially with rainfall. This was attributed to the growth of the vegetation's with a continuous increase of rain in rainless areas [45]. On the other hand, the temperature gave poor correlation with maximum NDVI, temperature was thus dropped from the prediction model development. Hence, seasonal rainfall and soil moisture were considered as predictands of NDVI.

Table 1. Seasonal multicollinearity diagnostic to determine the location of collinearity for rainfall, temperature and soil moisture, for March to May and October to December seasons

	MAM		OND	
	VIF	Klein	VIF	Klein
Rainfall	1.4355	0	1.1556	0
Temperature	1.7686	0	1.4565	0
Soil Moisture	2.2734	0	1.6415	0

3.2 Results of the Model Output

The model constants differ for each season and this is attributed to different rainfall drivers for the two seasons [1,3,46]. Hence, each season had its independent model, which was used to predict seasonal forage biomass. The prediction for MAM 2018 showed that forage biomass greater than 2 ton/ha was observed over much of the study area with high values over the western, northern, and eastern parts of the study area and much in the northern part in 2019 (Figure 2). A closer pattern to this was observed for the OND season (Figure 3) with different magnitudes in ton/ha since the two are important seasons over the study area in terms of rainfall amount. The observed pattern in the model output is attributed to rainfall and soil moisture patterns over the region. These outputs were then compared with observed forage biomass for verification purposes using the "eyeball" verification method [40], which examines the prediction and observation side by side. The model generally performs well in all the seasons (Figures 2 and 3) with few pocket areas of under-prediction in the eastern part and over-prediction in the western part, which was also evident in spatial analysis of ME and RMAE. The over-prediction areas were noted to be high altitude areas, and the converse is true for areas with under-prediction.

In order to manage livestock resources effectively, the model can be run with a one moth lead time for each season using predicted seasonal rainfall and soil moisture data from ICPAC. The prediction of rainfall and soil moisture is done using the Weather and Research Forecasting (WRF) model run operationally by ICPAC at seasonal time scale with a one-month lead time.

3.3 Reliability Diagram

The diagram was used to determine how well the predicted events correspond to their observed frequency and is said to be reliable if the curve falls on the diagonal line and skillful if it falls on the gray area of the plot [42-44]. The prediction models for MAM and OND were found to be reliable, with small parts of the curve fall outside the gray area; thus, the model has good skill in predicting forage biomass. An example for OND season is shown in Figure 4. This result gives confidence in using the model for seasonal prediction.

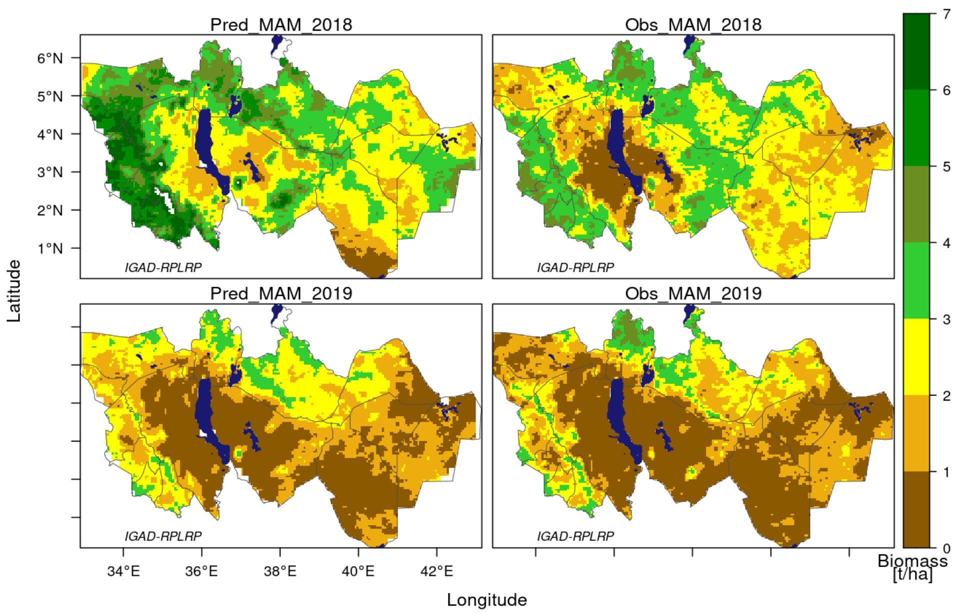

Figure 2. Bias corrected predicted forage biomass compared with observed forage biomass for the March to May seasons from 2018 to 2019

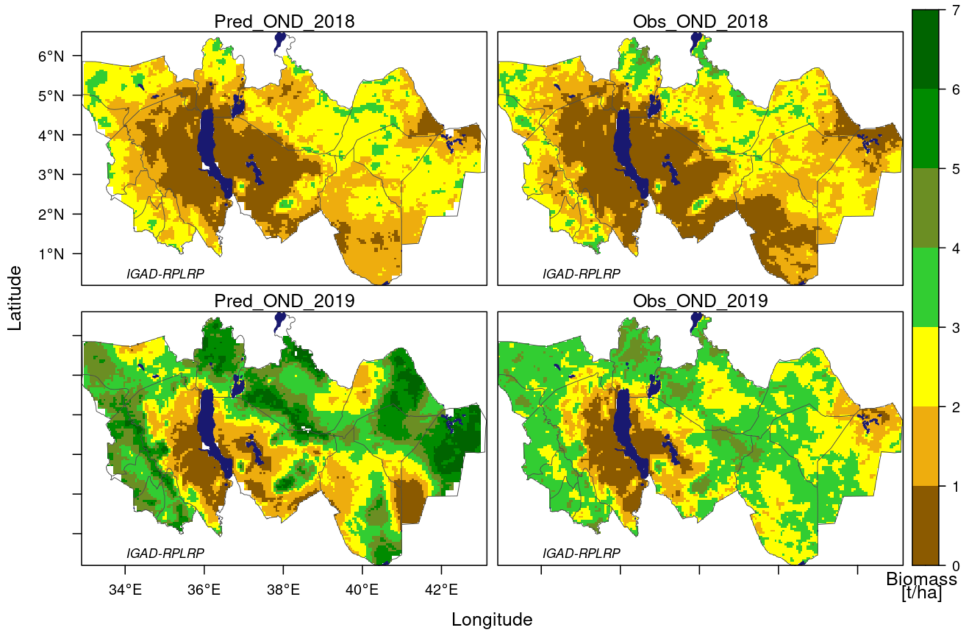

Figure 3. Bias corrected predicted forage biomass compared with observed forage biomass for the October to December seasons from 2018 to 2019

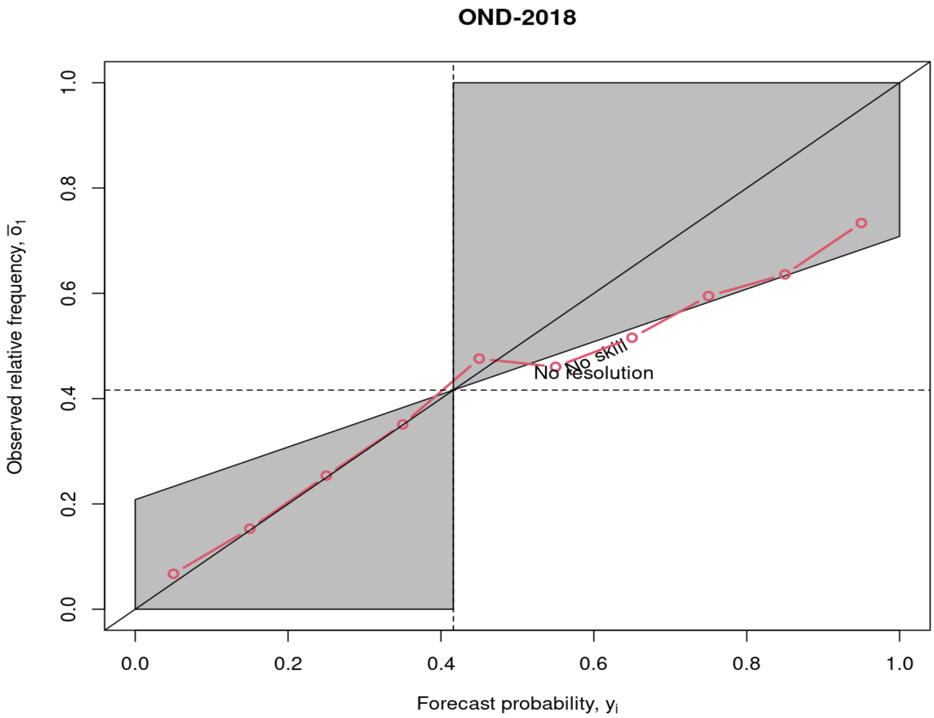

Figure 4. Reliability diagram for observed relative frequency against predicted probability for October-December 2018 season. It is reliable if the curve falls on the diagonal line and skillful if it falls on the gray area of the plot

4. Conclusions

Pastoralists in the Horn of Africa adapted to the temporal and spatial variability of critical resources (water and rangeland forage) in their landscape by practicing seasonal mobility with livestock (transhumance) to optimally utilize scarce resources. Such transhumance primarily crosses political boundaries. It is essential to develop early warning tools covering international borders; hence, a grid-based prediction is critical as it gives information across borders. This prototype prediction model is grid-based and performs well in forage biomass prediction over the study area, with rainfall and soil moisture being the significant drivers. It is currently running operationally at IGAD and at a seasonal time scale. This model's output informs the livestock sector group discussion at the Greater Horn of Africa Climate Outlook Forum (GHACOF), a regional early warning platform organized by ICPAC three times a year. This model contributes to timely and actionable early warning information for the rangeland, critical to pastoralists, sub-national key actors (government and NGOs), and other relevant policymakers within the region.

Author Contributions

Jully Ouma: Conceptualization, Methodology, Software, Formal analysis, Data Curation, Writing - Original Draft. **Dereje Wakjira**: Conceptualization, Validation, Resources, Writing - Review & Editing, Project administration. **Ahmed Amdihun**: Conceptualization, Methodology, Formal analysis, Writing - Review & Editing. **Eva Nyaga**: Methodology, Validation, Resources, Data Curation. **Eugene Kayijamahe** and **Viola Otieno**: Data Curation, Validation, Resources. **Franklin Opija**: Conceptualization, Methodology,Validation,Writing - Review & Editing. **John Muthama**: Validation, Writing - Review & Editing. **Solomon Munywa**: Resources, Supervision. **Guleid Artan**: Resources, Supervision.

Competing Interest

All authors consent with one accord that there is no conflict of interest for this publication.

Funding

This study was supported by the World Bank International Development Association (IDA) Grant No.: H9190, under the Regional Pastoral Livelihoods Resilience Project (RPLRP). This work is part of a PhD work at the University of Nairobi, Kenya, Department of Meteorology. We also acknowledge the contribution of ICPAC's climate team as well as the Global Monitoring for Environment and Security and Africa (GMES and Africa) program at ICPAC.

References

[1] Gudoshava, M., Misiani, H.O., Segele, Z.T., et al., 2020. Projected effects of 1.5 °C and 2 °C global warming levels on the intra-seasonal rainfall characteristics over the Greater Horn of Africa. Environmental Research Letters. 15(3). DOI: https://doi.org/10.1088/1748-9326/ab6b33

[2] Ongoma, V., Chen, H., Omony, G.W., 2018. Variability of extreme weather events over the equatorial East Africa, a case study of rainfall in Kenya and Uganda. Theoretical and Applied Climatology. 131(1-2), 295-308. DOI: https://doi.org/10.1007/s00704-016-1973-9

[3] Ayugi, B., Tan, G., Gnitou, G.T., et al., 2020. Historical evaluations and simulations of precipitation over East Africa from Rossby centre regional climate model. Atmospheric Research. 232. DOI: https://doi.org/10.1016/j.atmosres.2019.104705

[4] Ogallo, L.J., 1988. Relationships between seasonal rainfall in East Africa and the southern oscillation. Journal of Climatology. 8(1), 31-43.

[5] Saji, N.H., Goswami, B.N., Vinayachandran, P.N., et al., 1999. A dipole mode in the tropical Indian Ocean. Nature. 401, 360-363.

[6] Indeje, M., Semazzi, F.H.M., Ogallo, L.J., 2000. ENSO signals in East African rainfall seasons. International Journal of Climatology. 20(1), 19-46.

[7] Beherea, S.K., Yamagata, T., 2001. Subtropical SST dipole events in the southern Indian Ocean. Geophysical Research Letters. 28(2), 327-330. DOI: https://doi.org/10.1029/2000GL011451

[8] Opio, P., Makkar, H.P.S., Tibbo, M., et al., 2020. Opinion paper: A regional feed action plan – one-of-a-kind example from East Africa. Animal. 14(10), 1999-2002. DOI: https://doi.org/10.1017/S1751731120001056

[9] Amutabi, M.N., 2001. Resource Conflict in the Horn of Africa. Canadian Journal of African Studies. 35(2), 398-400.

[10] Bouslikhane, M., 2015. Cross Border Movements of Animals and Animal Products and Their Relevance to the Epidemiology of Animal Disease in Africa.

[11] Amutabi, M.N., 2010. Land and Conflict in the Ilemi Triangle of East Africa. Kenya Studies Review. 1(2), 20-36.

[12] de Oto, L., Vrieling, A., Fava, F., et al., 2019. Exploring improvements to the design of an operational seasonal forage scarcity index from NDVI time series for livestock insurance in East Africa. International Journal of Applied Earth Observation and Geoinformation. 82. DOI: https://doi.org/10.1016/j.jag.2019.05.018

[13] Mckee, T.B., Doesken, N.J., Kleist, J., 1993. The relationship of drought frequency and duration to time scales. Eighth Conference on Applied Climatology. 17(22), 179-183.

[14] Matere, J., Simpkin, P., Angerer, J., et al., 2020. Predictive Livestock Early Warning System (PLEWS): Monitoring forage condition and implications for animal production in Kenya. Weather and Climate Extremes. 27.
DOI: https://doi.org/10.1016/j.wace.2019.100209
[15] Kogan, F.N., 1995. Application of vegetation index and brightness temperature for drought detection. Space Res. 15(11), 273-1177.
[16] Stuth, J., Angerer, J., Kaitho, R., et al., 2003. The Livestock Early Warning System (LEWS): Blending technology and the human dimension to support grazing decisions. Arid Lands Newsletter. 53.
[17] Makuma-Massa, H., Majaliwa, J.G.M., Isubikalu, P., et al., 2012. Vegetation biomass prediction in the Cattle Corridor of Uganda. African Crop Science Journal. 20(2), 533-543.
[18] Georganos, S., Abdi, A.M., Tenenbaum, D.E., et al., 2017. Examining the NDVI-rainfall relationship in the semi-arid Sahel using geographically weighted regression. Journal of Arid Environments. 146, 64-74.
DOI: https://doi.org/10.1016/j.jaridenv.2017.06.004
[19] Duncan, D.A., Woodmansee, R.G., 1975. Society for Range Management Forecasting Forage Yield from Precipitation in California's Annual Rangeland. 28.
[20] Ju-Long, D., 1982. Control problems of grey systems. Systems & Control Letters. 1(5), 288-294.
[21] Min, J.J., Chen, P.Y., Sun, J.M., 1999. The Gray Prediction Search Algorithm for Block Motion Estimation. IEEE Transactions on circuits and systems for video technology. 9(6), 843-848.
[22] Trivedi, H.V., Singh, J.K., 2005. Application of grey system theory in the development of a runoff prediction model. Biosystems Engineering. 92(4), 521-526.
DOI: https://doi.org/10.1016/j.biosystemseng.2005.09.005
[23] Liu, G., Yu, J., 2007. Gray correlation analysis and prediction models of living refuse generation in Shanghai city. Waste Management. 27(3), 345-351.
DOI: https://doi.org/10.1016/j.wasman.2006.03.010
[24] Funk, C., Peterson, P., Landsfeld, M., et al., 2015. The climate hazards infrared precipitation with stations - A new environmental record for monitoring extremes. Scientific Data. 2.
DOI: https://doi.org/10.1038/sdata.2015.66
[25] Katsanos, D., Retalis, A., Michaelides, S., 2016. Validation of a high-resolution precipitation database (CHIRPS) over Cyprus for a 30-year period. Atmospheric Research. 169, 459-464.
DOI: https://doi.org/10.1016/j.atmosres.2015.05.015
[26] Agutu, N.O., Awange, J.L., Zerihun, A., et al., 2017. Assessing multi-satellite remote sensing, reanalysis, and land surface models' products in characterizing agricultural drought in East Africa. Remote Sensing of Environment. 194, 287-302.
DOI: https://doi.org/10.1016/j.rse.2017.03.041
[27] Dinku, T., Funk, C., Peterson, P., et al., 2018. Validation of the CHIRPS satellite rainfall estimates over eastern Africa. Quarterly Journal of the Royal Meteorological Society. 144, 292-312.
DOI: https://doi.org/10.1002/qj.3244
[28] Das, N.N., Entekhabi, D., Dunbar, R.S., et al., 2019. The SMAP and Copernicus Sentinel 1A/B microwave active-passive high resolution surface soil moisture product. Remote Sensing of Environment. 233.
DOI: https://doi.org/10.1016/j.rse.2019.111380
[29] Wichers, C.R., 1975. The Detection of Multicollinearity: A Comment. The Review of Economic and Statistics. 57(3), 366-368.
[30] Kovács, P., Petres, T., Tóth, L., 2005. A New Measure of Multicollinearity in Linear Regression Models. 73.
[31] Adeboye, N.O., Fagoyinbo, I.S., Olatayo, T.O., 2014. Estimation of the Effect of Multicollinearity on the Standard Error for Regression Coefficients. 10. www.iosrjournals.org.
[32] Imdadullah, M., Aslam, M., Altaf, S., 2016. mctest: An R Package for Detection of Collinearity among Regressors. The R Journal. 8(2), 495-502.
[33] Fotheringham, S., Brunsdon, C., Charlton, M., 2003. Geographically Weighted Regression: The Analysis of Spatially Varying Relationships. John Wiley & Sons.
[34] Matthews, S.A., Yang, T.C., 2012. Mapping the results of local statistics: Using geographically weighted regression. Demographic Research. 26, 151-166.
DOI: https://doi.org/10.4054/DemRes.2012.26.6
[35] Wang, K., Zhang, C., Li, W., 2013. Predictive mapping of soil total nitrogen at a regional scale: A comparison between geographically weighted regression and cokriging. Applied Geography. 42, 73-85.
DOI: https://doi.org/10.1016/j.apgeog.2013.04.002
[36] Charlton, M., Fotheringham, S., 2009. Geographically Weighted Regression. White Paper.
[37] Roger Bivand, M., 2022. Package "spgwr" Geographically Weighted Regression. http://gwr.nuim.ie/.
[38] Hobbs, T.J., 1995. The use of NOAA-AVHRR NDVI data to assess herbage production in the arid rangelands of central Australia. International Journal of Remote Sensing. 16(7), 1289-1302.
DOI: https://doi.org/10.1080/01431169508954477

[39] Toxopeus, A.G., 2000. Spatial and Temporal Modelling for Sustainable Management of Semi-Arid Rangelands: The Wildlife versus Livestock Issue in the Amboseli Ecosystem, Southern Kenya.

[40] Stanski, H.R., Wilson, L.J., Burrows, W.R., 1989. Survey of Common Verification Methods in Meteorology. 89.

[41] Mausio, K., Miura, T., Lincoln, N.K., 2020. Cultivation potential projections of breadfruit (Artocarpus altilis) under climate change scenarios using an empirically validated suitability model calibrated in Hawai'i. PLoS ONE. 15(5).
DOI: https://doi.org/10.1371/journal.pone.0228552

[42] Wilks, D.S., 1995. Statistical Methods in the Atmospheric Sciences. Vol 59. (Dmowska R, Holton JR, eds.). Academic Press.

[43] Hamill, T.M., 1997. Reliability Diagrams for Multicategory Probabilistic Forecasts. Weather and Forecasting. 12, 736-741.

[44] Bröcker, J., Smith, L.A., 2007. Increasing the reliability of reliability diagrams. Weather and Forecasting. 22(3), 651-661.
DOI: https://doi.org/10.1175/WAF993.1

[45] Leilei, L., Jianrong, F., Yang, C., 2014. The relationship analysis of vegetation cover, rainfall and land surface temperature based on remote sensing in Tibet, China. IOP Conference Series: Earth and Environmental Science. Vol 17. Institute of Physics Publishing.
DOI: https://doi.org/10.1088/1755-1315/17/1/012034

[46] Nicholson, S.E., 2017. Climate and climatic variability of rainfall over eastern Africa. Reviews of Geophysics. 55(3), 590-635.
DOI: https://doi.org/10.1002/2016RG000544

Journal of Atmospheric Science Research
https://ojs.bilpublishing.com/index.php/jasr

ARTICLE

A Diagnostic Method for Fog Forecasting Using Numerical Weather Prediction (NWP) Model Outputs

Aditi Singh* **R.S. Maheskumar** **Gopal R. Iyengar**

Ministry of Earth Sciences, Lodi Road, New Delhi, 110003, India

ARTICLE INFO

Article history
Received: 16 September 2022
Revised: 12 October 2022
Accepted: 13 October 2022
Published Online: 19 October 2022

Keywords:
Fog
Diagnostic method
Northern plains
Winter
Threshold

ABSTRACT

An attempt has been made in the present study to forecast fog with a diagnostic method using the outputs of global NWP model. The diagnostic method is based on the combination of thresholds of meteorological variables involved in fog formation. The thresholds are computed using the observations during fog. These thresholds are applied to the output of a global NWP model for forecasting fog. The occurrence of fog is a common phenomenon during winter season over the northern plains of India. The diagnostic method is used to predict fog occurrences over three stations in north India. The proposed method is able to predict both occurrences and non-occurrences of fog at all the three stations. It is found that 94% of the fog events forecasted by the model using the diagnostic method have been actually observed at the selected stations. The performance of method in predicting fog is found best over Delhi with the highest accuracy (0.61) and probability of detection (0.60). The study signifies that diagnostic approach based on the output of a global model is a useful tool for predicting fog over a single location.

1. Introduction

Fog formation over any region causes low visibility conditions leading to hazardous conditions worldwide and disrupting the normal life and all the modes of transport such as road, rail, air and marine traffic [1-5]. The aviation sector suffers economic losses in different parts of the world due to fog [6-10]. Thus, several climatological studies and field campaigns have been conducted focusing on some of the busiest airports around the world [11-14]. In addition, numerous field and numerical studies have been conducted worldwide [15-21,23-27] to understand the formation and development of fog. The studies indicated that a number of factors such as near surface radiative cooling profiles, topography, land surface characteristics, pollution, boundary layer temperature, humidity, wind speed and wind direction are responsible for fog formation over any surface. The understanding of local weather conditions that lead to fog, plays a major role in the operational forecasting of fog. Fog is a suspension of water droplets in the

*Corresponding Author:
Aditi Singh,
Ministry of Earth Sciences, Lodi Road, New Delhi, 110003, India;
Email: aditi.singh76@gov.in

DOI: https://doi.org/10.30564/jasr.v5i4.5068

atmosphere near the surface which are formed due to low temperature, high relative humidity and stable conditions. The water droplets condense on aerosols under polluted conditions. The prevalence of stable atmospheric conditions over the northern plains of India during winter season aids in formation of fog. The northern plains of India frequently experience western disturbances (WDs), low pressure systems observed in midlatitude westerlies which move from west to east in all seasons but are most prominent over Himalayas during the months of December to March. In winter season WDs provide sufficient moisture and stable conditions required for formation of fog over the northern plains of India [28,29]. The plains of north India are invariably affected by fog every year between the end of December to beginning of January due to typical prevailing meteorological and terrain conditions [30,31]. The studies conducted over India suggest an increase in fog events over the Indo-Gangetic basin (IGB) encompassing northern plains of India during the last decade [32,33] in the winter months. The airports, road and rail networks located in this region of India are affected by fog in winter months of December and January. According to a study [34], Indira Gandhi International Airport (IGIA) in Delhi suffered a total economic loss of approximately $3.9 million during 2011-2016 due to fog. Thus, the prediction of fog over the northern plains of India is significant for safe and efficient operations of all the modes of travel/transport. However, the accurate prediction of fog has long been a challenge for both the operational forecasters and the present numerical weather prediction (NWP) models. The present NWP models are not able to predict the fog due to lack of appropriate fog physics. The cloud schemes used in the operational NWP models are designed to represent the high-level clouds and precipitation and not the ground level fog. Also, the processes such as gravitational settling on the ground and surface layer turbulence involved in formation of fog are not included in the cloud scheme. Another reason is the coarse resolution of NWP models. The local weather conditions are not well represented in the coarse grid models and thus these models fail to accurately predict fog which is a local phenomenon. The third reason is that operational fog forecasting is based upon the model post processor and is not directly obtained from the model. The evolution of fog is a complex process and is related to turbulence [35] and the impact of turbulence cannot be represented in model post processor. Thus, a fog diagnostic method based on the model post processor output has been developed for fog prediction. One of the diagnostic methods used to predict fog with model post processor output is visibility diagnosis method. According to World Meteorological Organization (WMO), fog is a surface weather condition and occurs when surface visibility is less than 1000 meters (m). Thus, the visibility one of the variables diagnosed from the model postprocessor output is used to predict fog. Most of the operational model uses the Kunkel [36] fog visibility formulation based on surface liquid water content (LWC) to determine the visibility during fog. The verification studies conducted over different parts of world such as East China, North America and India [37-39] indicate a low performance of visibility diagnosis method. The multi-rule fog diagnosis method [40,37,41] was developed as the visibility diagnosis method exhibit poor performance in predicting fog. The study conducted by Zhou and Du [37] used the liquid water content (LWC), cloud base/top rule and surface relative humidity (RH)-wind rule. The study concluded that RH-wind rule with 2 m RH > 90%-95% and wind speed at 10 m < 2 m·s^{-1} works better when both the parameters are considered together than any of the parameters LWC or cloud base/top on individual basis. Another study by Payra and Mohan [41] mentioned that cloud base/top rule is good for coastal or marine fog and not for shallow or ground fog and utilized the two-level approach using RH-wind rule along with temperature gradient rule. Radiation and advection, two types of fog are generally observed in India. The advection fog occurs in the forward sector whereas the radiation fog occurs in the rear sector of a western disturbance. Radiation fog occurs due to radiative cooling of earth's surface during nighttime with favorable meteorological conditions of low wind speed, high relative humidity, clear sky and stable conditions.

The present study focuses on the prediction of radiation fog over the northern plains of India using the diagnostic method based on the threshold values of relative humidity at 2 m, dew point depression at 2 m and wind speed at 10 m. The threshold values of the variables are obtained from the observations during fog. The output of a global non-hydrostatic NWP model is used in the diagnostic method to predict fog in winter months of 2018-2019. The study is divided into different sections. The next section describes the diagnostic method for fog forecast. Section 3 describes the global model. Section 4 describes the results of the study and summary with conclusions is given in section 5.

2. Diagnostic Method for Fog Forecast

The diagnostic method used in the present work is based on the combination of meteorological variables involved in fog formation such as temperature, humidity and wind speed. The study considers the following criteria to derive fog forecast:

Surface relative humidity over an appropriate threshold

Difference between surface temperature and surface dew point temperature .i.e. dew point depression under an appropriate threshold

Wind speed at 10 m between two appropriate thresholds.

The thresholds of these variables are obtained from the observations during fog during three years (2016-2019) in winter months at three stations Amritsar, Delhi and Lucknow situated in north India. The presence of fog is identified based on the observed values of visibility from METAR observations at all the three sites. Fog is considered when the observed visibility is reported less than 1000 m.

The analysis of visibility observations for the months of December, January and February during 2016-2019, suggests that fog observed for 1071, 1851 and 823 hours at Amritsar, Delhi and Lucknow respectively. The frequency of dense fog hours with observed values of visibility <200 m was highest over Amritsar and comparable over Delhi and Lucknow. The meteorological conditions during the fog hours were analyzed using the METAR observations of surface temperature (T), dew point depression (T-Td), wind speed (WS)and specific humidity (SH). The values of relative humidity (RH) and specific humidity (SH) are obtained using the following equations.

$$RH = 100 - 5 \times (T - T_d) \tag{1}$$

$$SH = 6..1 \times 10^{\frac{(7.5 \times T_d)}{(237.3 + T_d)}} \tag{2}$$

During the fog hours, Amritsar observed high values of relative humidity close to 100% for maximum number of hours whereas the observed values of relative humidity lie in the range of 90%-100% for most of the hours over Delhi. Similarly, over Lucknow the observed values of relative humidity were 95%-100% for majority of hours. The dew point depression (difference between the temperature (T) and dew point temperature (T_d), T-T_d) was found zero at all the stations for majority of hours. The analysis of wind speed shows that weak surface winds of magnitude less than 2 $m \cdot s^{-1}$ prevailed at all the stations during the fog hours. The mean (M) and standard deviation (STDEV) values of the variables, calculated using Equation (3) and Equation (4) respectively are given in Table 1.

$$M = \frac{\Sigma x}{n} = \bar{x} \tag{3}$$

$$STDEV = \frac{\sqrt{(x - \bar{x})^2}}{n} \tag{4}$$

where x denotes any of the variable such as RH, T-Td, WS, T, SH and n is the total number of observations available at any station.

The mean values indicate the highest relative humidity, lowest dew-point depression, temperature and specific humidity over Amritsar. The mean value explains the tendency of the data to assume certain values and the quantification of dispersion of data is given in terms of the value of standard deviation. The thresholds values of T-Td, RH and WS required for fog formation are computed using the mean and standard deviation values of these variables at each station. The threshold of RH and minimum WS is obtained as mean minus standard deviation while the threshold of T-Td and maximum WS as mean plus standard deviation and are given in Table 2. The threshold of relative humidity is highest over Amritsar and lowest over Delhi, whereas the threshold of dew point depression is lowest over Amritsar and highest over Delhi. However, in case of wind speed the minimum and maximum wind speed required for fog formation is the lowest and highest over Delhi.

Table 1. Mean, standard deviation for surface relative humidity (RH), dew point depression (T-T_d) and wind speed (WS) during fog hours at Amritsar, Delhi and Lucknow

Amritsar					
	RH (%)	**T-Td (°C)**	**WS ($m \cdot s^{-1}$)**	**T (°C)**	**SH (g/kg)**
Mean	98.02	0.39	0.31	9.23	11.61
Standard Deviation	4.81	0.96	0.76	3.46	2.73
Delhi					
	RH (%)	**T-Td (°C)**	**WS ($m \cdot s^{-1}$)**	**T (°C)**	**SH (g/kg)**
Mean	92.23	1.55	1.55	11.36	12.30
Standard Deviation	8.37	1.67	3.22	3.19	2.21
Lucknow					
	RH (%)	**T-Td (°C)**	**WS ($m \cdot s^{-1}$)**	**T (°C)**	**SH (g/kg)**
Mean	95.55	0.89	0.51	10.47	12.56
Standard Deviation	5.43	1.09	0.83	8.35	2.86

Table 2. Thresholds for surface relative humidity, T-T_d and wind speed at Amritsar, Delhi and Lucknow

	Amritsar	**Delhi**	**Lucknow**
RH (%)	93.23%	83.86	90.12
T-Td (°C)	1.35	3.22	1.97
WS10 ($m \cdot s^{-1}$)	0.44-1.07	0.21-2.88	0.32-1.33

Thus, fog will be observed over Amritsar, Delhi and Lucknow whenever the values of relative humidity, dew point depression and wind speed will be probably equal to their respective thresholds.

3. Model Details

The operational global Unified Model (UM) of NCMRWF, (NCUM), used in the present study is developed at United Kingdom's Meteorological Office (UKMO). The model has a horizontal resolution of 17 km and 70 vertical levels with model top at 80 km. The dynamical core of the model uses semi-implicit, semi-Lagrangian formulation to solve the non-hydrostatic, fully compressible, deep atmospheric equations of motion [42]. The primary atmospheric prognostic variables are three-dimensional (3-D) wind components, virtual dry potential temperature, Exner pressure and dry density, whilst the moist prognostic variables such as mass mixing ratio of water vapor, prognostic cloud fields and other atmospheric loadings are advected as free tracers. The Arakawa C-grid staggering [43] is used for horizontal discretization of prognostic fields on to a regular latitude-longitude, whereas Charney-Philips staggering [44] using terrain following hybrid height coordinated is used for vertical discretization. The 4D-Var data assimilation scheme is used to prepare initial conditions four times (00, 06, 12 and 18 UTC) a day [45]. A deterministic ten-day forecast is generated daily based on 00 UTC initial conditions. The physical processes in the model are parameterized using different parameterization schemes. The radiation scheme of Edward and Slingo [46] with nine bands in long wave and six bands in short wave region is used to parameterize the radiative processes. The atmospheric boundary layer is parameterized with turbulence closure scheme of Lock et al. [47], which is further modified as described in Lock [48] and Brown et al. [49]. The Joint UK Land Environment Simulator (JULES) surface model [50,51] is used to model the land surface and its interactions with atmosphere. Convection in the model is represented through a mass flux scheme based on Gregory and Rowntree [52]. The prognostic cloud fraction and prognostic condensate (PC2) scheme is used for clouds and large-scale precipitation is represented using Wilson and Ballard [53]. The details of terrain such as soil properties, land use, vegetation albedo and the distribution of natural and anthropogenic emissions at lower boundary are specified using ancillary files from different sources Walters et al. [54].

4. Results & Discussion

The forecasted values of relative humidity, dew point depression and wind speed from NCUM are utilized in the diagnostic method to predict fog over the three stations. Thus, the performance of the model is first analyzed by comparing these meteorological variables obtained from model with the observations. Secondly, the thresholds obtained from the observations are applied to the output of model to forecast fog over a region. The output of the meteorological variables and the diagnostic method for fog forecast is verified during December 2018 through February 2019 over three stations Amritsar, Delhi and Lucknow.

4.1 Performance Analysis of NCUM

The forecast of temperature, dew point temperature, relative humidity and wind speed from NCUM are compared with observations at Amritsar, Delhi and Lucknow. The model output for the first 30 hours of the run is evaluated at each station for the fog hours during December 2018 to February 2019. The number of fog hours reported at Amritsar, Delhi and Lucknow are 134, 321 and 118, respectively. Fog at each station is reported between 18 UTC -23 UTC and 00 UTC- 06 UTC. Thus, the forecast of 18 hours to 30 hours based on 00 UTC initial conditions are compared with observations at each station.

The scatter diagram for observed and predicted surface temperature at three sites is shown Figure 1. The temperature over Amritsar (Figure 1 a) and Lucknow (Figure 1c) is over predicted by NCUM, whereas both under prediction and over prediction is observed over Delhi (Figure 1b).

Similarly, for dew point temperature the forecasted values are both over and under predicted over Amritsar (Figure 2a) and under predicted for majority of hours at Delhi (Figure 2b) and Lucknow (Figure 2c).

The forecast of relative humidity is highly under predicted at all the stations (Figure 3), whereas the forecast of wind speed is over predicted at all the stations (Figure 4).

The statistical scores such as bias, mean absolute error (MAE), root mean square error (RMSE) and correlation coefficient (R) are computed for each station and are given in Table 3. The scores indicate the highest correlation between the observed and forecasted values of temperature and dew point temperature. The values of RMSE are comparable for temperature, dew point temperature and wind speed whereas very high values are obtained for relative humidity at all the stations.

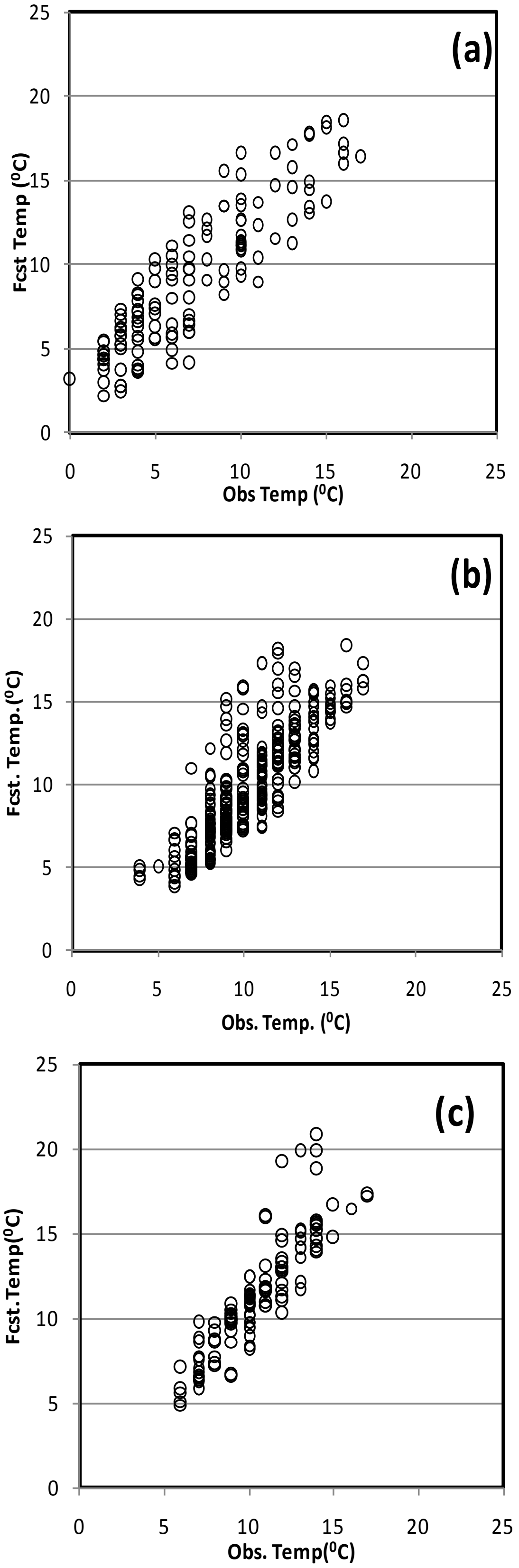

Figure 1. Scatter diagram of observed (Obs) (METAR) and forecasted (Fcst) (NCUM) temperature (Temp) at (a) Amritsar (b) Delhi and (c) Lucknow

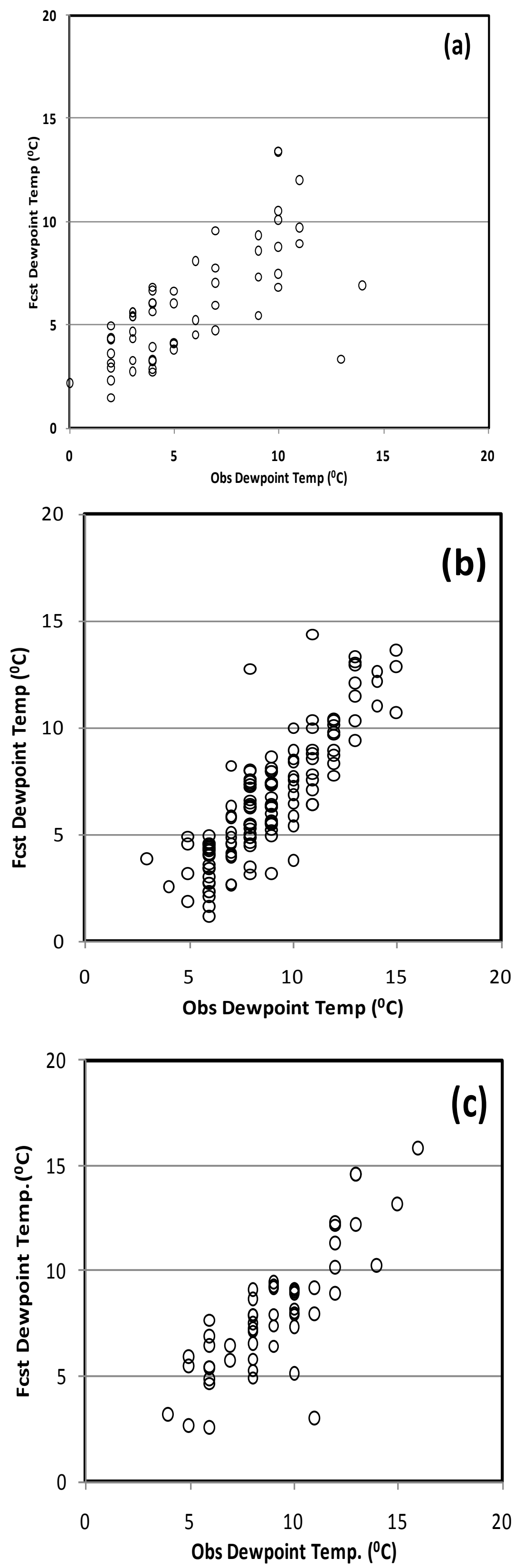

Figure 2. Scatter diagram of observed (Obs) (METAR) and forecasted (Fcst) (NCUM) dew point temperature at (a) Amritsar (b) Delhi and (c) Lucknow

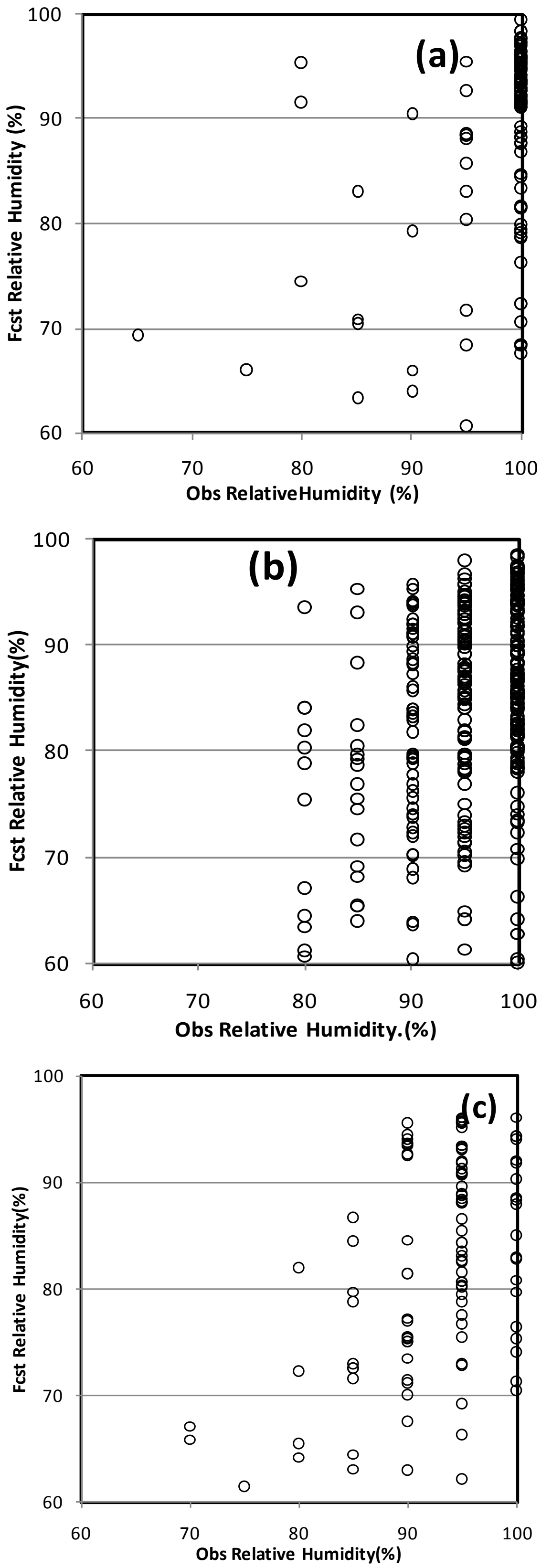

Figure 3. Scatter diagram of observed (Obs) (METAR) and forecasted (Fcst) (NCUM) relative humidity at (a) Amritsar (b) Delhi and (c) Lucknow

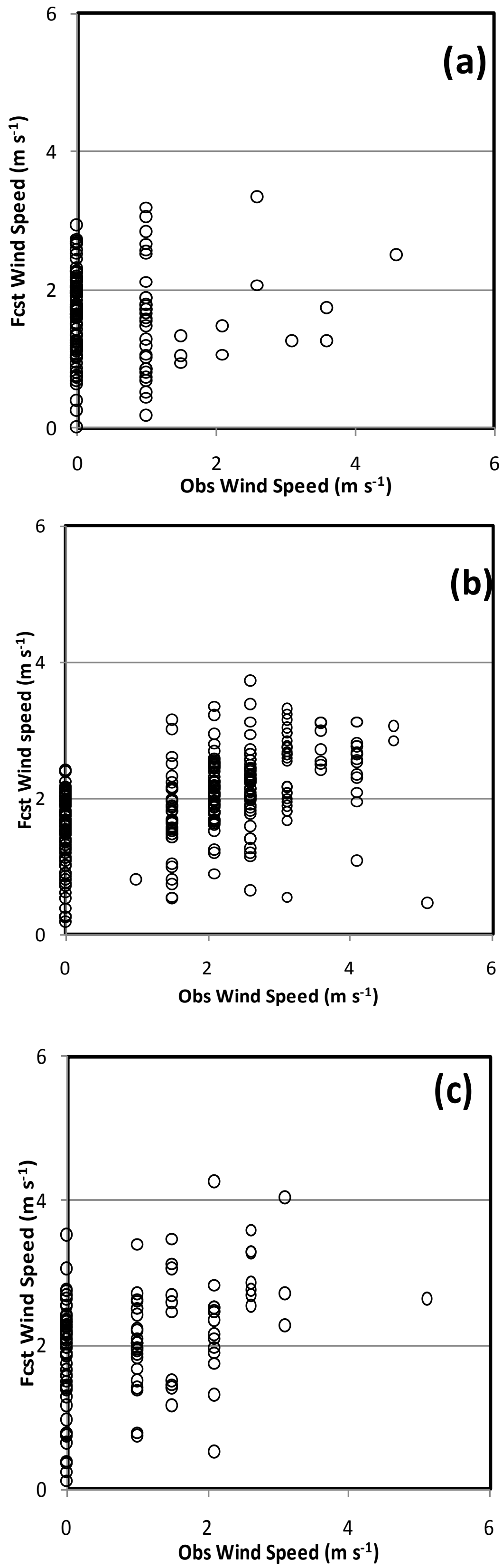

Figure 4. Scatter diagram of observed (Obs) (METAR) and forecasted (Fcst) (NCUM) wind speed at (a) Amritsar (b) Delhi and (c) Lucknow

Table 3. Statistical analysis of NCUM performance at three stations

Amritsar				
	Bias	**RMSE**	**Correlation**	**MAE**
Temperature	1.93	2.77	0.88	2.28
Dew-Point Temperature	0.16	2.41	0.71	1.80
Relative Humidity	–12.04	16.60	0.53	12.51
Wind Speed	1.14	1.62	0.14	1.43
Delhi				
	Bias	**RMSE**	**Correlation**	**MAE**
Temperature	–0.34	1.93	0.83	1.49
Dew-Point Temperature	–2.23	2.74	0.84	2.40
Relative Humidity	–11.90	15.62	0.49	12.50
Wind Speed	0.38	1.22	0.54	0.96
Lucknow				
	Bias	**RMSE**	**Correlation**	**MAE**
Temperature	0.83	1.86	0.88	1.29
Dew-Point Temperature	–1.14	2.05	0.82	1.52
Relative Humidity	–11.50	14.97	0.54	12.13
Wind Speed	1.22	1.60	0.36	1.35

A positive bias for temperature with higher values over Amritsar than Lucknow indicates an over-prediction which agrees with scatter plot (Figure 1a and 1c). Similarly, the lowest negative bias in temperature values over Delhi indicates the least under prediction. For dew point temperature the lowest bias is obtained for Amritsar. A positive bias is obtained for wind speed with comparable magnitude at all the stations. The values of MAE for temperature, dew point temperature and wind speed are comparable at all the stations and lowest MAE is obtained for wind speed over Delhi.

4.2 Performance of the Diagnostic Method in Predicting Fog

The diagnostic method is based on the threshold of relative humidity, dew point depression and wind speed obtained from observations at three selected stations. These thresholds are applied to the observed and forecasted values of relative humidity, dew point depression and wind speed over Amritsar, Delhi and Lucknow for the fog hours during 2018-2019.

The diagnostic method of fog forecast is evaluated by computing the statistical scores such as accuracy, probability of detection (POD), false alarm ratio (FAR), success ratio (SR) and threat score (TS) (WWRP) [55]. These indices are computed based on the frequency of positive and negative occurrences such as:

Hits are the events for which both the forecasted and observed values of variables are within the thresholds defined over any given station.

Correct Negatives (CN) are the events when both forecasted and observed values of variables are greater than or lower than the thresholds defined over the station.

False Alarms are those events when forecasted values are within the thresholds but not the observed values and **Misses** are the events when observed values are within the thresholds but not the forecasted values.

A perfect system should produce only hits and correct negatives (CN) and a positive event in the present work is represented by the correct detection/forecast of fog presence.

The forecast of fog over Amritsar, Delhi and Lucknow is verified using the Yes/No forecast and the statistical scores. For 134 hours of fog observed at Amritsar, the diagnostic method gave Hits for 55 hours, Misses for 59 hours, False Alarm for 01 hour and Correct Negative for 19 hours. Similarly, over Delhi the fog was observed for 321 hours and was predicted for 175 hours (Hits), not predicted for 119 hours (Misses), falsely predicted for 07 hour (false Alarm) and for 20 hours the fog was neither observed and nor predicted. In case of Lucknow, there were 118 hours of fog out of which the number of Hits were obtained for 08 hours, Misses for 63 hours, False Alarm for 01 hour and Correct Negatives for 46 hours.

The statistical scores are computed using the number of Hits, Misses, False Alarms and Correct Negatives over Amritsar, Delhi and Lucknow and are shown in Figure 5. The highest POD (0.60), threat score (0.58) and accuracy (0.61) with FAR of 0.04 is obtained over Delhi. The performance of diagnostic method in predicting fog over Amritsar is comparable to Delhi with POD of 0.48, threat score of 0.48, accuracy of 0.55 and FAR of 0.02. The scores over Lucknow indicate that diagnostic method failed to predict fog for majority of hours.

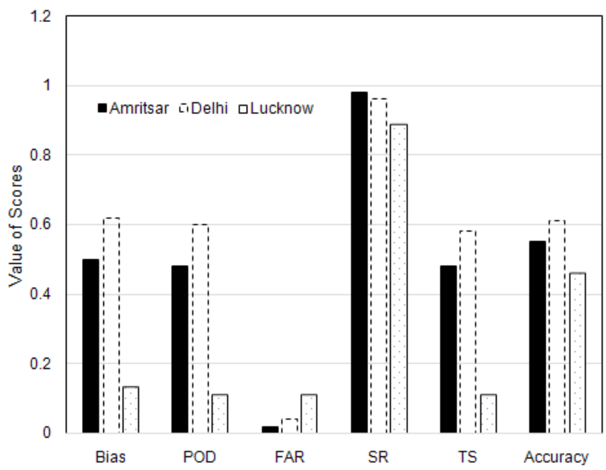

Figure 5. Statistical Scores at Amritsar, Delhi and Lucknow for performance of the diagnostic method

5. Conclusions

In this study, a diagnostic method is used for forecasting fog over three stations Amritsar, Delhi and Lucknow situated in the northern plains of India. The diagnostic method is based on the thresholds of relative humidity, dew point depression and wind speed for the formation of fog. The thresholds are computed at each of the station using the observations of winter months (December-February) for three years 2016-2019 during fog. The output of NCUM is used to predict fog with diagnostic method over Amritsar, Delhi and Lucknow. The study includes the performance analysis of NCUM in predicting surface temperature, dew point temperature, relative humidity and wind speed at three stations. The verification of diagnostic method is also carried out using the Yes/No forecast for the winter months of 2018-2019. The main findings of the study are summarized as follows:

The threshold of relative humidity for the formation of fog is found lowest over Delhi (83.86%) and highest over Amritsar (93.23%). The threshold of dew point depression is highest over Delhi and lowest over Amritsar. For wind speed the minimum threshold is lowest and maximum threshold is highest over Delhi.

The performance of NCUM in predicting temperature, dew point temperature and wind speed is found comparable to observations at all the stations, however the relative humidity is over-predicted by NCUM at all the stations.

Considering the three sites, the diagnostic method is able to predict fog in the 18-30 hour forecast with an overall accuracy of 0.54 and a probability of false detection equal to 0.11. The performance of the diagnostic method is found best over Delhi and comparable to Amritsar, whereas the fog is poorly predicted over Lucknow.

The averaged bias of 0.42 together with low value of probability of false detection indicates that the method produces a consistent number of missed fog events.

The average of success ratio is 0.94, which means that 94% of the fog events forecasted by the model have been actually observed.

Acknowledgements

The authors acknowledge the National Centre for Medium Range Weather Forecasting (NCMRWF), Noida, India for the global NCUM products. There is no funding source and no conflict of interest.

Conflict of Interest

There is no conflict of interest.

References

[1] Gultepe, I., Tardif, R., Michaelides, S.C., et al., 2007. Fog research: A review of past achievements and future perspectives. Pure and Applied Geophysics. 164(6), 1121-1159.

[2] Jenamani, R.K., Tyagi, A., 2011. Monitoring fog at IGI Airport and analysis of its runway-wise spatio-temporal variations using Meso-RVR network. Current Science. 100, 491-501.

[3] Bergot, T., 2013. Small-scale structure of radiation fog: a large eddy simulation study. Quarterly Journal of Royal Meteorological Society. 139, 1099-1112.

[4] Haeffelin, M., Laffineur, Q., Bravo-Aranda, J.A., et al., 2016. Radiation fog formation alerts using attenuated backscatter power from automatic lidars and ceilometers. Atmospheric Measurement Techniques. 9(11), 5347-5365.
DOI: https://doi.org/10.5194/amt-9-5347-2016

[5] Singh, A., George, J.P., Iyengar, G.R., 2018. Prediction of fog/visibility over India using NWP Model. Journal of Earth System Science. 127(2), 26.
DOI: https://doi.org/10.1007/s12040-018-092-2

[6] Croft, P.J., 2003. Fog. Encyclopedia of atmospheric

sciences. J. R. Holton, J. A. Pyle, J. A. Curry (Eds.), Academic Press. pp. 777-792.
[7] Forthun, G., Johnson, M., Schmitz, W., et al., 2006. Trends in fog frequency and duration in the southeast United States. Physical Geography. 27, 206-222. DOI: https://doi.org/10.2747/0272-3646.27.3.206
[8] Gultepe, I., Tardif, R., Michaelides, S.C., et al., 2007. Fog research: A review of past achievements and future perspectives. Pure and Applied Geophysics. 164(6), 1121-1159.
[9] Gultepe, I., Pearson, G., Milbrandt, J.A., et al, 2009. The fog remote sensing and modeling field project. Bulletin of American Meteorological Society. 90, 341-359. DOI: https://doi.org/10.1175/2008BAMS2354.1
[10] Kulkarni, R.G., et al., 2019. Loss to aviation economy due to winter fog in New Delhi during the winter of 2011–2016. Atmosphere. 10, 198-210.
[11] Tardif, R., Rasmussen, R.M., 2007. Event-based climatology and typology of fog in the New York City region. Journal of Applied Meteorology and Climatology. 46, 1141-1168.
[12] Ghude, S.D., Bhat, G.S., Prabhakaran, T., et al., 2017. Winter fog experiment over the Indo-Gangetic plains of India. Current Science. 112, 767-784. DOI: https://doi.org/10.18520/cs/v112/i04/767-784
[13] Izett, J.G., et al., 2019. Dutch fog: On the observed spatio-emporal variability of fog in the Netherlands. Quarterly Journal of Royal Meteorological Society. 145, 2817-2834.
[14] Guerreiro, P.M.P., et al., 2020. An Analysis of Fog in the Mainland Portuguese International Airports. Atmosphere. 11, 1239-1260.
[15] Brown, R., Roach, W.T., 1976. The physics of radiation fog II-a numerical study. Quarterly Journal of Royal Meteorological Society. 102, 351-354.
[16] Holtslag, A.A.M., De Bruijin, E.I.F., Pan, H.L., 1990. A high resolution air mass transformation model for short-range weather forecasting. Monthly Weather Review. 118, 1561-1575.
[17] Bergot, T., Guedalia, D., 1994. Numerical forecasting of radiation fog. Part I. Numerical model and sensitivity tests. Monthly Weather Review. 122, 1218-1230.
[18] Fisak, J., Rezacova, D., Mattanen, J., 2006. Calculated and measured values of liquid water content in clean and polluted environments. Studia Geophysica et Geodaetica. 50, 121-130.
[19] Bergot, T., Terradellas, E., Cuxart, J., et al., 2007. Intercomparison of single-column numericalmodels for the prediction of radiation fog. Journal of Applied Meteorology and Climatology. 46, 504-521.
[20] Gultepe, I., Pagowski, M., Reid, J., 2007. A satellite-based fog detection scheme using screen air temperature. Weather and Forecasting. 22, 444-456. DOI: https://doi.org/10.1175/WAF1011.1
[21] Haeffelin, M., Bergot, T., Elias, T., et al., 2009. Paris fog: Shedding new light on fog physical processes. Bulletin of the American Meteorological Society. 91(6), 767-783.
[22] Liu, D.Y., Yang, J., Niu, Sh.J., et al., 2011. On the evolution and structure of a radiation fog event in Nanjing. Advances in Atmospheric Sciences. 28(1), 223-237.
[23] Sun, K., 2015. WRF-chem simulation of a severe haze episode in the Yangtze River Delta, China. Aerosol and Air Quality Research. DOI: https://doi.org/10.4209/aaqr.2015.04.0248
[24] Lin, C.Y., Zhang, Zh.F., Pu, Zh.X., 2017. Numerical simulations of an advection fog event over Shanghai Pudong International Airport with the WRF model. Journal of Meteorological Research. 31, 874-889.
[25] Boutle, I., Price, J., Kudzotsa, I., et al., 2018. Aerosol–fog interaction and the transition to well-mixed radiation fog. Atmospheric Chemistry and Physics. 18(11), 7827-7840. DOI: https://doi.org/10.5194/acp-18-7827-2018
[26] Pithani, P., Ghude, S.D., Chennu, V.N., et al., 2018. WRF model Prediction of a dense fog event occurred during Winter Fog Experiment (WIFEX). Pure and Applied Geophysics. DOI: https://doi.org/10.1007/s00024-018-2053-0
[27] Price, J.D., Lane, S., Boutle, I.A., et al., 2018. LANFEX: A field and modeling study to improve our understanding and forecasting of radiation fog. Bulletin of e American Meteorological Society. 99(10), 2061-2077. DOI: https://doi.org/10.1175/BAMS-D-16-0299.1
[28] Pasricha, P.K., et al., 2003. Role of water vapour green house effect in the forecasting of fog occurrence. Boundary Layer Meteorology. 107, 469-482. DOI: https://doi.org/10.1023/A:1022128800130
[29] Dimri, A.P., Barros, N., Ridley, P.A., et al., 2015. Western disturbances: A review. Reviews of Geophysics. 53, 225-246. DOI: https://doi.org/10.1002/014RG000460
[30] Choudhury, S., Rajpala, H., Sarafa, A.A., et al., 2007. Mapping and forecasting of north Indian winter fog: an application of spatial technologies. International Journal of Remote Sensing. 28, 3649-3663.
[31] Chakraborty, A., Gupta, T., Tripathi, S.N., 2016. Combined effects of organic aerosol loading and fog

processing on organic aerosols oxidation, composition and evolution. Science of Total Environment. 573, 690-698.

[32] Jenamani, R.K., 2007. Alarming rise in fog and pollution causing a fall in maximum temperature over Delhi. Current Science. 93, 314-322.

[33] Syed, F.S., Körnich, H., Tjernstrom, M., 2012. On the fog variability over South Asia. Climate Dynamics. 39, 2993-3005.
DOI: https://doi.org/10.1007/s00382-012-1414-0

[34] Kulkarni, R.G., et al., 2019. Loss to aviation economy due to winter fog in New Delhi during the winter of 2011–2016. Atmosphere. 10, 198-210.

[35] Stull, R.B., 1988. An Introduction to Boundary layer Meteorology, Kluwer Academic Publishers. pp. 666.

[36] Kunkel, B.A., 1984. Parameterization of droplet terminal velocity and extinction coefficient in fog models. Journal of Climate and Applied Meteorology. 23, 34-41.

[37] Zhou, B., Du, J., 2010. Fog prediction from a multimodel mesoscale ensemble prediction system. Weather and Forecasting. 25, 303-322.

[38] Zhou, B.B., Du, J., Gultepe, I., et al., 2011. Forecast of Low Visibility and Fog From NCEP– Current Status and Efforts. Pure and Applied Geophysics. 169, 895-909.

[39] Aditi, et al., 2015. Verification of Visibility Forecast from NWP model with Satellite and Surface Observations. Mausam. 66, 603-616.

[40] Zhou, B., Ferrier, B.S., 2008. Asymptotic analysis of equilibrium in radiation fog. Journal of Applied Meteorology and Climatology. 47, 1704-1722.

[41] Payra, S., Mohan, M., 2014. Multirule Based Diagnostic Approach for the Fog Predictions Using WRF Modelling Tool. Advances in Meteorology. pp. 1-11.
DOI: https://doi.org/10.1155/2014/456065

[42] Wood, N., Staniforth, A., White, A., et al., 2014. An inherently mass-conserving semi-implicit semi-Lagrangian discretization of the deep-atmosphere global nonhydrostatic equations. Quaterly Journal of Royal Meteorological Society. 140, 1505-1520.
DOI: https://doi.org/10.1002/qj.2235, 2014

[43] Arakawa, A., Lamb, V.R., 1977. Computational design of the basic dynamic processes of the UCLA general circulation model. Methods in Computational Physics. Advances in Research and Applications. 17, 173-265.

[44] Charney, J.G., Phillips, N.A., 1953. Numerical integration of the quasi-geostrophic equations for barotropic and simple baroclinic flows. Journal of Meteorology. 10, 71-99.

[45] George, J.P., et al., 2016. NCUM data assimilation system. NMRF/TR/01/2016.

[46] Edwards, J.M., Slingo, A., 1996. Studies with a flexible new radiation code. I: Choosing a configuration for a largescale model. Quarterly Journal of Royal Meteorological Society. 122, 689-719.

[47] Lock, A.P., Brown, A.R., Bush, M.R., et al., 2000. A new boundary layer mixing scheme. Part I: Scheme description and single-column model tests. Monthly Weather Review. 128, 3187-3199.

[48] Lock, A.P., 2001. The numerical representation of entrainment in parametrizations of boundary layer turbulent mixing, Monthly. Weather Review. 129, 1148-1163.

[49] Brown, A.R., et al., 2008. Upgrades to the boundary-layer scheme in the Met Office numerical weather prediction model. Boundary Layer Meteorology. 128, 117-132.
DOI: https://doi.org/10.1007/s10546-008-9275-0

[50] Best, M.J., Pryor, M., Clark, D.B., et al., 2011. The Joint UK Land Environment Simulator (JULES), model description –Part 1: Energy and water fluxes. Geoscientific Model Development. 4, 677-699.

[51] Clark, D.B., Mercado, L.M., Sitch, S., et al., 2011. The Joint UK Land Environment Simulator (JULES), model description – Part 2: Carbon fluxes and vegetation dynamics. Geoscientific.Model Development. 4, 701-722.

[52] Gregory, D., Rowntree, P.R., 1990. A massflux convection scheme with representation of cloud ensemble characteristics and stability dependent closure. Monthly Weather Review. 118, 1483-1506.

[53] Wilson, D.R., Ballard, S.P., 1999. A microphysically based precipitation scheme for the UK Meteorological Office Unified Model. Quarterly Journal of Royal, Meteorological, Society. 125, 1607-1636.
DOI: https://doi.org/10.1002/qj.49712555707

[54] Walters, D., Brooks, M., Boutle, I., et al., 2017. The Met Office Unified Model Global Atmosphere 6.0/6.1 and JULES Global Land 6.0/6.1 configurations. Geoscientific Model Development. 10, 1487-1520.
DOI: https://doi.org/10.5194/gmd-10-1487-2017

[55] WWRP/WGNE Joint Working Group on Forecast Verification Research. Available online: https://www.cawcr. gov.au/projects/verification/ (Accessed on 13 December 2019).

BILINGUAL PUBLISHING CO.

Journal of Atmospheric Science Research

https://ojs.bilpublishing.com/index.php/jasr

ARTICLE

Indoor Particulate Matter Assessment in a Northern Nigerian Abattoir and a Residential Building

Francis Olawale Abulude[1*] Abigail Oluwakemi Feyisetan[2] Kikelomo Mabinuola Arifalo[3] Akinyinka Akinnusotu[4] Lateef Johnson Bello[4]

1. Science and Education Development Institute, Akure, Ondo State, Nigeria
2. Department of Chemistry, Federal University of Technology, Minna, Niger State, Nigeria
3. Department of Chemistry, Bamidele Olomilua University of Education, Science and Technology, Ikere-Ekiti, Ekiti State, Nigeria
4. Department of Science Laboratory Technology, Rufus Giwa Polytechnic, Owo, Ondo State, Nigeria

ARTICLE INFO

Article history

Received: 26 September 2022

Revised: 19 October 2022

Accepted: 21 October 2022

Published Online: 24 October 2022

Keywords:

Pollutants

Health risks

Air quality index

Living room

Office

Indoor pollution

ABSTRACT

Indoor air pollution in buildings puts people at risk of developing respiratory and cardiovascular diseases. Particulate matter (PM) exposure is known to cause these health issues. Preliminary efforts were made in this study to assess the quantity and quality of $PM_{1.0}$, $PM_{2.5}$, and PM_{10} present in an abattoir and a residential building in northern Nigeria. Canree A1 low-cost sensor was used to monitor the locations, 8 hourly for two weeks. The results showed that the average values (μg/m^3) of $PM_{1.0}$, $PM_{2.5}$, and PM_{10} in an abattoir were 62.74, 161.94, and 199.08, respectively, and in a residential building were 28.70, 83.31, and 103.71. The average Air Quality Index (AQI) of the abattoir office was Very Unhealthy, while the living room of the residential building was unhealthy. The $PM_{2.5}$, and PM_{10} levels were higher than the international (WHO) and national (FMEnv) standard limits, indicating a potential danger to building occupants. It is expected that the indoor environment of the locations will be improved by the use of good ventilators (adequate windows and doors) and the provision of good extractors.

1. Introduction

World Health Organisation reported that air pollution killed more people in one year than AIDS, malaria, and tuberculosis combined. Over 91% of the world-wide people resides in polluted areas which are elevated more than WHO standards for particulate matter ($PM_{2.5}$ and PM_{10}), ozone (O_3), nitrogen dioxide (NO_2), and sulfur dioxide (SO_2) which are four important pollutants in terms of pub-

*Corresponding Author:
Francis Olawale Abulude,
Science and Education Development Institute, Akure, Ondo State, Nigeria;
Email: walefut@gmail.com

DOI: https://doi.org/10.30564/jasr.v5i4.5104

lic health. According to Cohen et al. [1] and Wambebe and Duan [2], ambient $PM_{2.5}$ (particulate matter less than 2.5 micrometers in diameter) is present in up to 16.5% of the reported premature deaths each year (4.2 million), they also reported an estimated 1.7 million lung cancer-related deaths.

Particulate matter (PM) exposure has been linked to negative health outcomes. PM sensitivity has been reported to be higher in children under the age of 15, the elderly (over the age of 65), and people who have weakened immune systems and/or pre-existing medical problems [3]. According to surveys of human activity patterns, the average individual spends 87% of their day in confined building structures [4]. As a result, individual contact is mainly due to indoor PM.

Indoor Air Pollution in buildings is the cause of high risk of respiratory and cardiovascular diseases which has affected many people especially the vulnerable. Results of studies with respect to the microbial contaminants in indoor air have been reported in different locations which include residential, hospitals, schools, museums, abattoirs, office and other environments [5-8] but, there were little or no work of indoor air assessment in abattoirs. Literature (Table 1) from abattoirs related research delved on the effects (health risk) of oxides of gases and volatile organic compounds on the people present [7-11]. Also many studies on the microbial contaminants have been studied [6,12-15]. To close or remove the above gap, in this work, we made efforts in quantifying the indoor air quality of an abattoir and living room of a residential building. We are of the opinion that this work will add knowledge to the issues on abattoirs in terms of indoor air quality. An office in the abattoir is the case study in this work.

The study was aimed at reporting the findings of an assessment of $PM_{1.0}$, $PM_{2.5}$, and PM_{10} held at an abattoir and a residential building.

Table 1. Summary of relevant previous studies of PM concentrations in indoor microenvironments on the study of other cities

Saudi Arabia (Dammam)	Assessment of air quality in Dammam slaughter houses, Saudi Arabia	Average levels of NO_2 and CO were lower than their AQGs. SO_2 and VOCs exceeded the air quality guidelines. Bacterial and fungal strains contaminated slaughterhouse	[6]
Nigeria (Obinze and Egbu)	Assessment Of Air Quality In Livestock Farms And Abattoirs In Selected LGAs Of Imo State	The result of air quality parameters were above Federal Ministry of Environment (FMEnv) air quality standard. Abattoir Results: 31.2 µg/m^3, 0.64 ppm, 0.17 ppm, 1.04 ppm and 1.93 ppm for $PM_{2.5}$, SO_2, NH_3, NO_2 and H_2S in the wet season and 29.8 µg/m^3, 0.67 ppm, 0.13 ppm, 0.53 ppm and 1.7 ppm for $PM_{2.5}$, SO_2, NH_3, SO_2, and H_2S in the dry season.	[10]
Nigeria (Ntak Inyang)	Determination of Some Air Pollutants and Meteorological Parameters in Abattoir, Ntak Inyang in Uyo L.G.A of Akwa Ibom State in Nigeria	The result showed that NO_2, SO_2, H_2S, CO, NH_3, Cl_2, HCN, TVOC, $PM_{2.5}$ and PM_{10} were higher than that of FEPA standard limit. Results revealed correlations between particulate matter, the gases, and meteorological parameters.	[16]
Nigeria (Ilorin)	Integrated Assessment of the Air Quality around the Environs of Dr. Abubakar Sola Saraki Memorial Abattoir, Ilorin, Kwara State, Nigeria	The $PM_{2.5}$, PM_{10}, HCHO and Volatile Organic Compounds were higher than WHO limits. High temperature was favorable to thermophiles biological activities.	[14]
Nigeria (Ile-Ife)	Assessment of the impacts of abattoir activities on ambient air quality and health risk associated with exposure to $PM_{2.5}$ and PM_{10}, H_2S, SO_2 and NH_3	The results indicated that the average concentrations of $PM_{2.5}$, PM_{10} and NO_2 were higher than the WHO, NAAQS, and FMEnv) limits. Air Quality Index showed that the ambient air quality in respect of CO and NH_3 was very good, moderate for PM_{10} and was very poor for NO_2 and SO_2. All the HQ values exceeded the threshold value, set at the unity.	[7]
Saudi Arabia (Abha)	Particulate matter concentration and health risk assessment for a residential building during COVID-19 pandemic in Abha, Saudi Arabia	PM concentration was exceeding 300 μg/m^3 (unhealthy) for all particle sizes of $PM_{0.3}$, $PM_{0.5}$, PM_1, and $PM_{2.5}$ except for PM_{10}. CO_2 concentration was 700 ppm. With influential habit (aromatic smoke), these concentrations increased 2–28 times for PM. The hazard quotient value greater than 1 revealed potential health risk to the inhabitants.	[11]

Table 1 continued

Country (City)	Study	Main Findings	References
Cameroon (Yaounde)	Air Quality and Human Health Risk Assessment in the Residential Areas at the Proximity of the Nkolfoulou Landfill in Yaound´e Metropolis, Cameroon	At the location 30% of the daily mean concentrations of $PM_{2.5}$ and PM_{10} crossed the daily safe limits. The values of cancer risk (CR) due to the inhalation of CH_2O were >10−6 while those of hazard index (HI) due to the inhalation of CH_2O, H_2S, and SO_2 were <1. The landfill operations might be supplying air pollutants to the neighbouring residential areas.	[9]
South Korea	Measurement of Particulate Matter ($PM_{2.5}$) and Health Risk Assessment of Cooking-Generated Particles in the Kitchen and Living Rooms of Apartment Houses	The $PM_{2.5}$ concentration increased 3.8 times more than the 24 h standard (50 μg/m^3). The $PM_{2.5}$ concentration in the living room was slightly greater than that in the kitchen.	[17]

2. Materials and Methods

Nigeria is one of the countries in West Africa with the capital at the Federal Capital Territory (FCT), Abuja. Nigeria has 36 states and has the highest population in Africa. Nigeria shares the boundaries in the north with Niger, in the east Chad and Cameroon, south - the Gulf of Guinea, and the west - Benin. The country derived its named from the Niger River [18]. The country has two climates - rainy and dry periods. Each period lasts six months. This study took place at FCT, Abuja in the northern part of Nigeria (Table 2).

A low-cost monitoring device (Canāree A1) was used in this study. $PM_{1.0}$, $PM_{2.5}$, and PM_{10} concentrations were monitored at the indoor locations of an abattoir (Office) and a residential building (Living room) in FCT, Abuja (Figure 1). The floors of the locations were made of ceramic. The office of the abattoir has a fan working during the monitoring period (August to September 2022). The only window and door were left opened during the periods. At the building location, there was an air conditional operating during the periods for at least 20 h per day, but all the windows and doors were locked during the period. At the abattoir, slaughtering, burning of woods and tyres to roast goats and cows, and commercial activities were the anthropogenic activities recorded, but at the residential building, there were cooking activities such as baking, roasting, frying, and the use of perfume. The monitoring took place during the school vacation and so lots of inhabitants' time were spent in the living room in which the sensor was mounted. The methodology of the manufacturer was strictly followed. The device was configured and registered to a SenseiAQ Cloud Account using SenseiAQ Software Version 1.2.3 (Download: https://github.com/PieraSystems/SenseiAQ). The data obtained was subjected to analysis with Minitab and Excel software.

Table 2. The Location, Description, and the Coordinates of the PM Monitoring

Location	Description	Coordinate
New Karu	Abattoir	9°0'40.794" N; 7°34'46.698" E; Altitude: 444 m a.s.l
Abacha Road	Residential	9°1'22.416" N; 7°35'19.812" E; Altitude: 409 m a.s.l

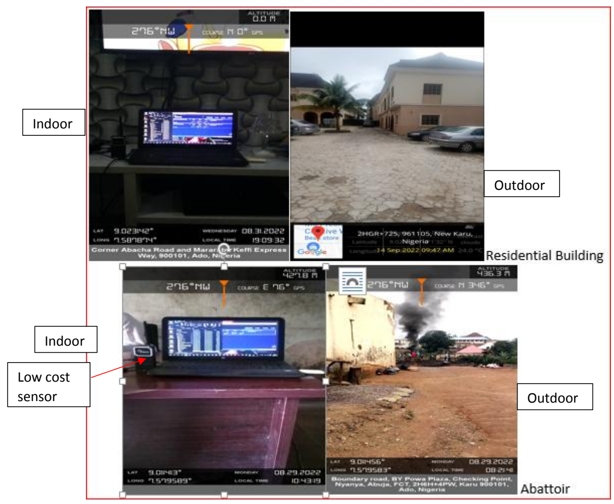

Figure 1. Description of the Locations

3. Results and Discussion

Table 3 shows the particulate matter concentrations of the two locations. The results showed the average values (μg/m^3) of abattoir as 62.74, 161.94 and 199.08 and residential building as 28.70, 83.31, and 103.71 of $PM_{1.0}$, $PM_{2.5}$, and PM_{10} respectively. It is evident from the results that abattoir indoor (office) values were more compared to that of residential. The reasons can be explained by the more anthropogenic activities (the burning of tyres and woods for roasting of goats and cows) which released more PM, another reason was due to the small door and window of the office which trapped the emissions indoor, the available fan present in the office could not extract much because there was no cross ventilation. In the case of the residential building, although high values were reported, this was due to the emission released from the cooking (especially from frying and baking) activities from the kitchen. The air conditional working during the monitoring assisted by extracting the excess fumes. When there was no cooking, the elevated PM recorded was due to the activities (use of perfume and sweeping) of the occupants in the room. The StDev and CofVar were high especially in $PM_{2.5}$, and PM_{10} this showed that there were large variations between the minimum and maximum concentrations. These can be picked when there were no activities that will trigger the elevations. From the table, it was observed that the results obtained were far above the WHO and FEPA the implication of this is that the individuals within the environment are prone to health hazard.

Figure 2 depicts the particulate matter contributions in each location. $PM_{2.5}$ was the most heavily contributed (66%) in the residential, followed by $PM_{1.0}$ (23%), implying that more $PM_{2.5}$ was emitted during cooking activities, which is supported by Kumar et al. [21]. More PM_{10} (47%) was emitted in the case of the abattoir. The findings agreed with those of Jonah [16] and Sawyerr et al. [14], who found higher levels of PM_{10} than $PM_{2.5}$ in abattoirs.

The time series of the results are depicted in Figures 3 and 4. The trends in the abattoir show a high increase during heavy smoke emission, followed by a decrease during smoke dispersal away from the location. The high concentration of PM indoors was caused by the high concentrations of smoke in the office. The increase in recorded concentrations could be attributed to the insufficient ventilation provided by the rotating fan, small window, and door. The concentrations of PM in residential buildings vary as well; the lowest trend (value) was obtained during normal occupant activities in the living room, while the highest values up to the maximum trend were obtained during frying activities in the kitchen (the escape of the emission into the living room). The presence of a working air conditioner helped contribute to the low trends observed.

Figures 3 and 4 show that the trends in PM are irregular, the increases in the concentration for specific measurements in specific locations at specific times, could be due to the burning of tyres, woods, and frying activities both in the abattoir and residential building. The high PM trends were higher than the international (WHO) and national (FMEnv) standard limits.

Table 3. Particulate Matter Concentrations in the two locations (Abattoir and Residential)

	Abattoir			Residential		
	$PM_{1.0}$	$PM_{2.5}$	PM_{10}	$PM_{1.0}$	$PM_{2.5}$	PM_{10}
Mean	62.74	161.94	199.08	28.70	83.31	103.71
StDev	76.14	224.61	262.34	58.07	229.73	274.23
CoffVar (%)	121.36	138.69	131.78	202.30	275.76	264.42
Minimum	6.91	15.60	19.52	2.51	7.12	10.03
Maximum	720.62	3038.45	3468.66	642.40	2567.33	2069.37
Q1	77.97	201.02	249.69	13.05	28.84	38.68
Q3	17.80	37.68	49.30	26.60	60.46	76.87
Skewness	2.82	4.33	4.00	7.64	8.01	8.01
Kurtosis	10.52	33.8	29.19	66.65	71.77	71.78
*WHO [19] FEPA/	-	15	45			
FMEnv [20]	-	-	150			

*24 h, FEPA-Federal Environmental Protection Agency, Federal Ministry of Environment

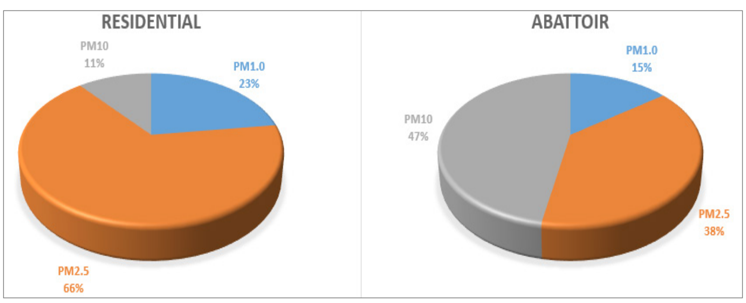

Figure 2. Contributions of Particulate Matter from the Locations

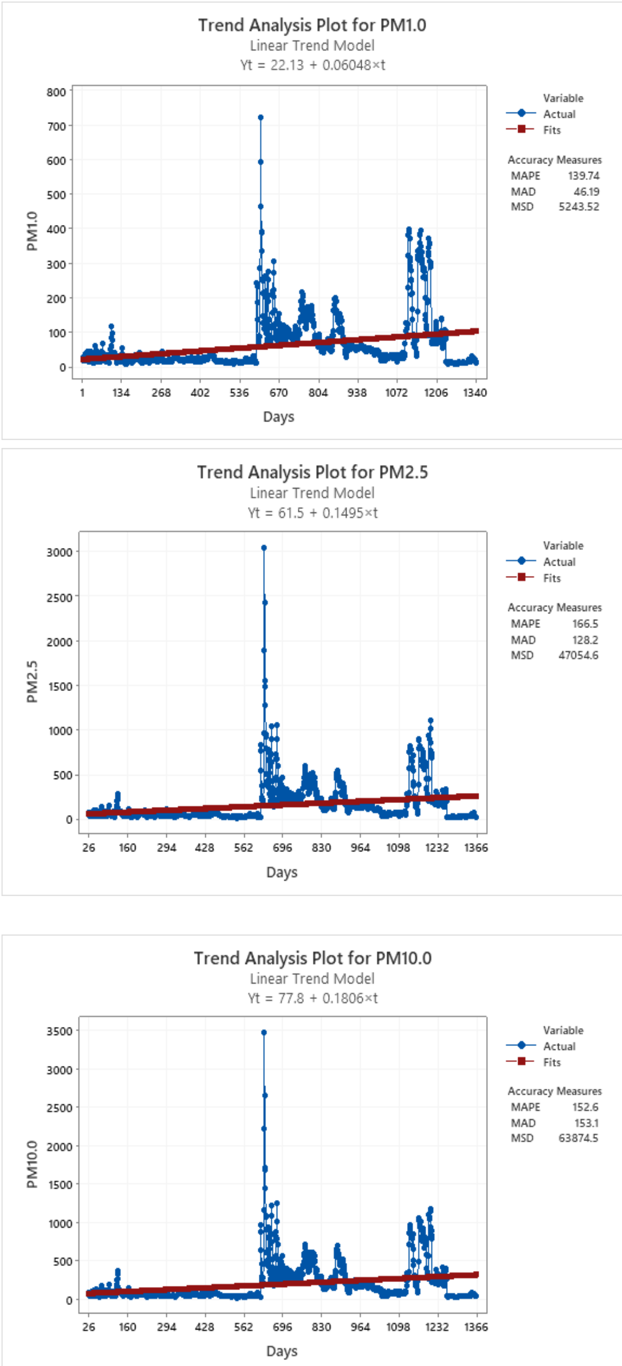

Figure 3. Trends Analysis of the Particulate Matter (Abattoir)

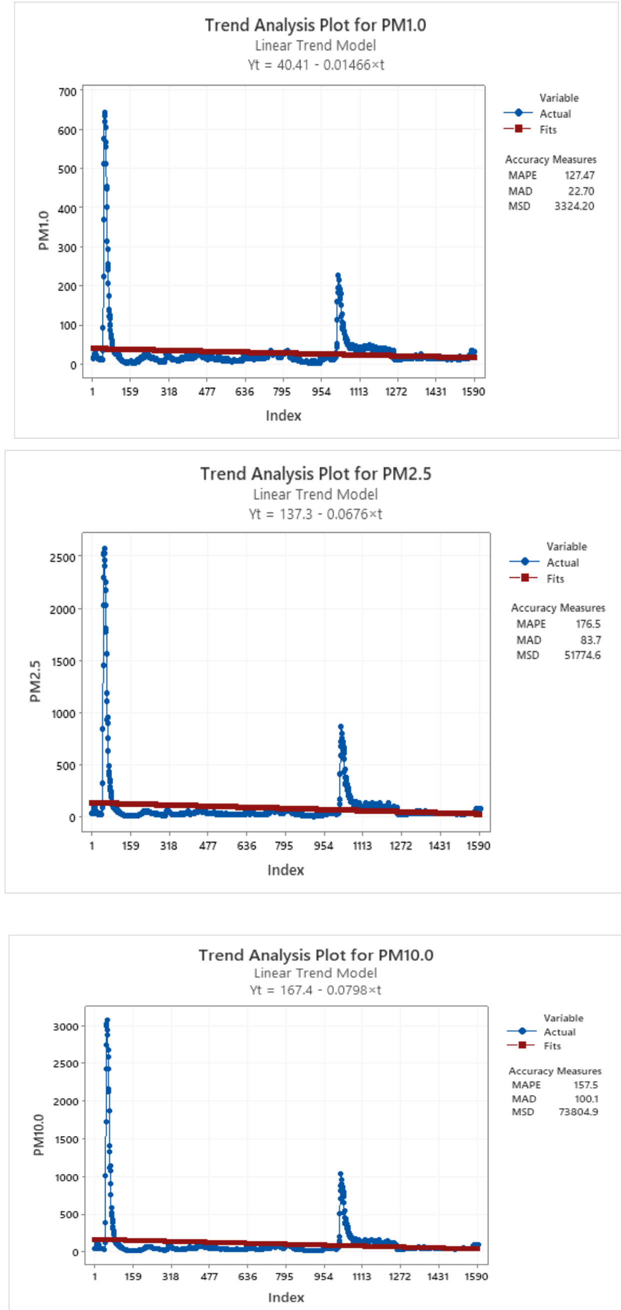

Figure 4. Trends Analysis of the Particulate Matter (Residential)

The AQI for the two locations is shown in Tables 4 and 5. These figures were derived from the USEPA [22]. The Abattoir $PM_{2.5}$ mean value was 161.94 (μg/m^3), translating to an AQI of 212, and the category was Very Unhealthy. While the minimum and maximum values were moderate and hazardous, respectively. The hazardous to sensitive group implies that everyone should take steps to minimize their risk when particle pollution levels are in this range. Remaining indoors – in a building or a room with filtered air – and reducing your activity levels are the best methods for lowering the amount of particulate emissions you inhale in to the lungs. Regrettably, the suggestion was not followed because there were no extractors or adequate ventilation. In the same location, the average AQI (123) for PM_{10} was Unhealthy for Sensitive Groups, while the maximum was above > 500, as with $PM_{2.5}$. When particle pollution levels are within this range, every individual should strive to take bold and significant steps to reduce their contact. The average AQI in the residential building was unhealthy; the minimum (30), while good, put people with respiratory or heart disease, the elderly, and children at risk. Individuals who are unusually sensitive to PM_{10} AQI values of 75 should avoid prolonged or heavy exertion. The moderate AQI category for PM_{10} in the residential building matched the findings of Odekanle et al. [7] in an abattoir in Ile-Ife, Nigeria.

Table 4. *Explanations and Conversions of Particulate Matter Concentrations to AQI Using AQI Calculator (Abattoir)

Concentration (μg/m^3)	**161.94 (mean)**
AQI	212
AQI Category	Very Unhealthy
Sensitive Group	People with respiratory or heart disease, the elderly and children are the groups most at risk
Effects	Significant aggravation of heart or lung disease and premature mortality in persons with cardiopulmonary disease and the elderly; significant increase in respiratory effects in general population
Cautionary Statement	People with respiratory or heart disease, the elderly and children should avoid any outdoor activity; everyone else should avoid prolonged exertion
Concentration (μg/m^3)	**15.60 (Minimum)**
AQI	58
AQI Category	Moderate
Sensitive Group	People with respiratory or heart disease, the elderly and children are the groups most at risk
Effects	People with respiratory or heart disease, the elderly and children are the groups most at risk
Cautionary Statement	Unusually sensitive people should consider reducing prolonged or heavy exertion
Concentration (μg/m^3)	**3038.45 (Maximum)**
AQI	**Above > 500 level**
AQI Category	Hazardous
Sensitive Group	Pollution is hazardous at these levels. Everyone should take steps to reduce their exposure when particle pollution levels are in this range
Effects	
Cautionary Statement	Staying indoors – in a room or building with filtered air – and reducing your activity levels are the best ways to reduce the amount of particle pollution you breathe into your lungs
	PM_{10}
Concentration (μg/m^3)	**199.08 (mean)**
AQI	123
AQI Category	Unhealthy for Sensitive Groups
Sensitive Group	People with respiratory disease are the group most at risk
Effects	Increasing likelihood of respiratory symptoms and aggravation of lung disease, such as asthma
Cautionary Statement	People with respiratory disease, such as asthma, should limit outdoor exertion
Concentration (μg/m^3)	**19.52 (minimum)**
AQI	18
AQI Category	Good
Sensitive Group	People with respiratory disease are the group most at risk
Effects	None
Cautionary Statement	None

Table 4 continued

	$PM_{2.5}$
Concentration (μg/m^3)	
AQI	**3468.66**
AQI Category	Hazardous
Sensitive Group	Pollution is hazardous at these levels. Everyone should take steps to reduce their exposure when particle pollution levels are in this range
Effects	
Cautionary Statement	Staying indoors – in a room or building with filtered air – and reducing your activity levels are the best ways to reduce the amount of particle pollution you breathe into your lungs.

*There is no standards for $PM_{1.0}$ so the explanations and conversions could not be made

Table 5. *Explanations and Conversions of Particulate Matter Concentrations to AQI Using AQI Calculator (Residential)

Concentration (μg/m^3)	**83.31 (mean)**
AQI	165
AQI Category	Unhealthy
Sensitive Group	People with respiratory or heart disease, the elderly and children are the groups most at risk
Effects	Increased aggravation of heart or lung disease and premature mortality in persons with cardiopulmonary disease and the elderly; increased respiratory effects in general population
Cautionary Statement	People with respiratory or heart disease, the elderly and children should avoid any outdoor activity; everyone else should avoid prolonged exertion
Concentration (μg/m^3)	**7.12 (Minimum)**
AQI	30
AQI Category	Good
Sensitive Group	People with respiratory or heart disease, the elderly and children are the groups most at risk
Effects	None
Cautionary Statement	None
Concentration (μg/m^3)	**2567.33 (Maximum)**
AQI	**Above > 500 level**
AQI Category	Hazardous
Sensitive Group	Pollution is hazardous at these levels. Everyone should take steps to reduce their exposure when particle pollution levels are in this range
Effects	
Cautionary Statement	Staying indoors – in a room or building with filtered air – and reducing your activity levels are the best ways to reduce the amount of particle pollution you breathe into your lungs
	PM_{10}
Concentration (μg/m^3)	**103.71 (mean)**
AQI	75
AQI Category	Moderate
Sensitive Group	People with respiratory disease are the group most at risk
Effects	Unusually sensitive people should consider reducing prolonged or heavy exertion
Cautionary Statement	Unusually sensitive people should consider reducing prolonged or heavy exertion
Concentration (μg/m^3)	**10.03 (minimum)**
AQI	9
AQI Category	Good
Sensitive Group	People with respiratory disease are the group most at risk
Effects	None
Cautionary Statement	None
Concentration (μg/m^3)	
AQI	**3069.37**

Table 5 continued

	$PM_{2.5}$
AQI Category	Hazardous
Sensitive Group	Pollution is hazardous at these levels. Everyone should take steps to reduce their exposure when particle pollution levels are in this range
Effects	
Cautionary Statement	Staying indoors – in a room or building with filtered air – and reducing your activity levels are the best ways to reduce the amount of particle pollution you breathe into your lungs.

*There is no standards for $PM_{1.0}$ so the explanations and conversions could not be made

4. Conclusions

A low-cost monitoring device (Canāree A1) was used in this study to assess the indoor $PM_{1.0}$, $PM_{2.5}$, and PM_{10} concentrations at an abattoir (Office) and a residential building (Living room) in FCT, Abuja. The results depicted that abattoir PM concentrations were higher than those of the residential building due to the continuous activities (burning of tyres and woods) at the abattoir. Also, the results obtained in this study showed that the PM values both locations surpass the recommended standard limits of WHO and FEPA/FMEnv. The AQI obtained in the study for the average and maximum fell between moderate and hazardous which are potential danger or threat to the occupants of the buildings and the environment. Mitigation efforts should be ensured to either reduce or stop the man-made activities causing the emission of the particles into the air and efforts too should be made to provide adequate ventilation and air extractors within the buildings in the two locations.

Acknowledgment

The authors are grateful for the management and staffs of the Karu abattoir, FCT, Abuja, Nigeria for granting the permission to use their facility for the study. Also, the authors are grateful to Piera Systems Inc., Canada for making available the low-cost sensor (Canāree A1).

Conflict of Interest

The authors declare no conflict interest.

References

[1] Cohen, A.J., Brauer, M., Burnett, R., et al., 2017. Estimates and 25-year trends of the global burden of disease attributable to ambient air pollution: an analysis of data from the Global Burden of Diseases Study 2015. The Lancet. 389(10082), 1907-1918.

[2] Wambebe, N.M., Duan, X., 2020. Air quality levels and health risk assessment of particulate matters in Abuja municipal area, Nigeria. Atmosphere. 11(8), 817.

[3] Mohammadyan, M., Ghoochani, M., Kloog, I., et al., 2017. Assessment of indoor and outdoor particulate air pollution at an urban background site in Iran. Environmental Monitoring and Assessments. 189, 235.

[4] Mahmoud Mohammadyam, M., Keyvani, S., Bahrami, A., et al., 2019. Assessment of indoor air pollution exposure in urban hospital microenvironments. Air Quality, Atmosphere & Health. 12, 151-159. DOI: https://doi.org/10.1007/s11869-018-0637-6

[5] Wemedo, S.A., Ede, P.N., Chuku, A., 2012. Interaction between building design and Indoor airborne microbial load in Nigeria. Asian Journal of Biological Sciences. 5(4), 183-191.

[6] Salama, K.F., Berekaa, M.M., 2016. Assessment of air quality in Dammam slaughter houses, Saudi Arabia. International Journal of Medical Science and Public Health. 5(2), 287-291.

[7] Odekanle, E.L., Sonibare, O.O., Odejobi, O.J., et al., 2020. Air emissions and health risk assessment around abattoir facility. Heliyon. 6(7), e04365. DOI: https://doi.org/10.1016/j.heliyon.2020.e04365

[8] Abulude, F.O., Ratford, V., Ratford, J., et al., 2022. Canāree, a Novel Low-Cost Sensor for Indoor Air Quality Monitoring: A Case Study of Indoor Assessments from Akure, Nigeria. DOI: http://dx.doi.org/10.2139/ssrn.4054652v

[9] Feuyit, G., Nzali, S., Lambi, J.N., et al., 2019. Air Quality and Human Health Risk Assessment in the Residential Areas at the Proximity of the Nkolfoulou Landfill in Yaound´e Metropolis, Cameroon. Journal of Chemistry. DOI: https://doi.org/10.1155/2019/3021894

[10] Uyo, C.N., Njoku, J.D., Iwuji, M.C., et al., 2021. Assessment of Air Quality in Livestock Farms and Abattoirs in Selected LGAs of Imo State. International Journal of Advanced Academic Research. 7(8), 54-68.

[11] Algarni, S., Khan, R., Khan, N., et al., 2021. Particulate matter concentration and health risk assessment for a residential building during COVID-19 pandemic in Abha, Saudi Arabia. Environmental Science and Pollution Research. 28(46).
DOI: https://doi.org/10.1007/s11356-021-15534-6

[12] Lues, J.F.R., Theron, M.M., Venter, P., et al., 2007. Microbial composition in bioaerosols of a high-throughput chicken-slaughtering facility. Poultry Science. 86, 142-149.

[13] Veskoviã-Moraåanin, S.M., Boroviã, B.R., Velebi, B.M., et al., 2009. Dentification of mycobiota in Serbian slaughter-houses. Proceedings of Natural Sciences, Matica Srpska. 117, 45-49.

[14] Sawyerr, H.O., Opasola, O.A., Oluwatuyi, S.V., et al., 2020. Integrated Assessment of the Air Quality around the Environs of Dr. Abubakar Sola Saraki Memorial Abattoir, Ilorin, Kwara State, Nigeria. International Journal of Research and Scientific Innovation. 7(11), 142-146.

[15] Szulc, J., Okrasa, M., Dybka-Stępień, K., et al., 2020. Assessment of Microbiological Indoor Air Quality in Cattle Breeding Farms. Aerosol and Air Quality Research. 20, 1353-1373.
DOI: https://doi.org/10.4209/aaqr.2019.12.0641

[16] Jonah, A.E., 2020. Determination of Some Air Pollutants and Meteorological Parameters in Abattoir, Ntak Inyang in Uyo L.G.A of Akwa Ibom State in Nigeria. International Journal of Science and Management Studies. 3(6), 1-8.
DOI: https://doi.org/10.51386/25815946/ijsms-v3i6p101

[17] Kim, H., Kang, K., Kim, T., 2018. Measurement of Particulate Matter ($PM_{2.5}$) and Health Risk Assessment of Cooking-Generated Particles in the Kitchen and Living Rooms of Apartment Houses. Sustainability. 10, 843.
DOI: https://doi.org/10.3390/su10030843

[18] Abulude, F.O., Abulude, I.A., Oluwagbayide, S.D., et al., 2022. Air Quality Index: a Case of 1Day Monitoring in 253 Nigerian Urban and Suburban Towns. Journal of Geovisualization and Spatial Analysis. 6, 5.
DOI: https://doi.org/10.1007/s41651-022-00100-6

[19] WHO, 2021. WHO global air quality guidelines. Particulate matter ($PM_{2.5}$ and PM_{10}), ozone, nitrogen dioxide, sulfur dioxide and carbon monoxide. Geneva: World Health Organization.

[20] FEPA/FMEnv, 1999. National Guidelines for Environmental Audit in Nigeria. Federal Environmental Protection Agency. Federal Government Press, Abuja, Nigeria.

[21] Kumar, P., Hama, S., Abbass, R.A., et al., 2022. In-kitchen aerosol exposure in twelve cities across the globe. Environment International. 162, 107155.
DOI: https://doi.org/10.1016/j.envint.2022.107155

[22] AirNow, 2022. Concentration to AQI Calculator. AirNow.gov - Home of the U.S. Air Quality Index. https://www.airnow.gov/aqi/aqi-calculator-concentration/. (Accessed 28th August, 2022)

BILINGUAL PUBLISHING CO.
Pioneer of Global Academics Since 1984

Journal of Atmospheric Science Research
https://ojs.bilpublishing.com/index.php/jasr

ARTICLE
On the Impact of Bell Sound on Ambient Particulates

Konstantinos Kourtidis* **Ageliki Andrikopoulou**

Department of Environmental Engineering, Democritus University of Thrace, Xanthi, 67100, Greece

ARTICLE INFO

Article history
Received: 04 October 2022
Revised: 05 November 2022
Accepted: 07 November 2022
Published Online: 14 November 2022

Keywords:
Sound
Aerosols
Particulate matter
Sound pressure level

ABSTRACT

Here the authors examine whether bell sounds can have an impact on ambient aerosol levels and size distribution under atmospheric conditions. The authors present calculation results for acoustic coagulation by church bell sounds for a range of ambient aerosol types. The results show that for orthokinetic sonic agglomeration, while the frequency spectrum of church bells is ideal for causing coagulation of ambient aerosols, the sound pressure level (SPL) becomes too low for an effect. However, for very polluted conditions, at extremely short distances from the bell dust aerosols can readily undergo sonic coagulation.

1. Introduction

People have tried to influence atmospheric properties with sound for a long time. In the French wine-growing regions, church-bells were traditionally rung in the case of incoming storms to suppress hail. In 1575 Pope Urban VIII authorized a prayer for consecrating church bells that called for "driving away the harmful storms, hail and strong winds" [1]. Church-bell ringing was, near the turn of the 19th century, replaced by firing upward rockets or cannons. Numerous loud sound producing devices have been deployed in Europe at around that time [2]. In the last two decades, hail canons have been employed in California vineyards, parking lots for newly manufactured cars in the NISSAN Motor Corporation factory in Canton, United States of America (U.S.A.), the Volkswagen plant in Puebla, Mexico, and elsewhere. There is no evidence for the effectiveness or ineffectiveness of these devices. A recent review [3] summarized a variety of measurements, concluding against the use of cannons or explosive rockets. Both church bells as well as sonic hail canons, use sound to potentially impact the hail generation process.

*Corresponding Author:
Konstantinos Kourtidis,
Department of Environmental Engineering, Democritus University of Thrace, Xanthi, 67100, Greece;
Email: kourtidi@env.duth.gr

DOI: https://doi.org/10.30564/jasr.v5i4.5121

Particle agglomeration, the increase of the size of particles, contributes to cloud formation and aerosol sedimentation. Sound is known to cause agglomeration at high SPLs, termed acoustic agglomeration or acoustic coagulation, due to particle resonance and the resulting relative motion of particles, and hence could potentially impact atmospheric particles. Acoustic agglomeration in air pollution control devices has been studied for some decades now and is an effective method for removing fine particles from industrial exhausts by coagulating them into coarser particles [4-7].

The main identified mechanisms for agglomeration are orthokinetic collision and hydrodynamic collision, the latter through mutual scattering interaction, mutual radiation pressure interaction and acoustic wake influence. Orthokinetic collision is the main mechanism of sonic agglomeration for polydisperse particles at low frequencies and medium particle size ratios. The orthokinetic mechanism refers to collisions between differently sized particles located within a distance that is approximately equal to the displacement amplitude of the acoustic field and with their relative motion substantially parallel to the direction of vibration [8]. It is based on the different resonance rate η of the particles due to their different sizes d_1, d_2 (different amplitudes for different sizes resulting in increased collisions) and is not very effective for particles much smaller than 1 μm. The orthokinetic model does not explain the observation of interactions between particles initially separated at distances much larger than the acoustic displacements and the agglomeration of particles of similar sizes [9,10]. In these cases, the main mechanism is hydrodynamic collision (less drag on the trailing particle). Hydrodynamic interaction refers to collisions caused by the viscous interaction between particles and their surrounding medium (air in our case), and can occur for particles that are separated at distances much larger than their acoustic displacement amplitudes. In general, two approaches to account for hydrodynamic forces have been proposed—mutual radiation pressure interaction and the acoustic wake effect. The mutual radiation pressure interaction is based on the Bernoulli principle and is possible only for interparticle distances $< 5(d_1+d_2)$ whereas for interparticle distances $> 10(d_1+d_2)$ it is negligible. It results in more relative motion of two particles when $d_1/d_2=1/3$ and no relative motion when $d_1/d_2 = 1$ (i.e. monodisperse particles), hence other mechanisms have to bring first the particles near each other. The mutual scattering interaction is due to the reflection of the sound wave on a particle and the resulting interaction between nearby particles. The acoustic wake effect is the main mechanism of sonic agglomeration for monodisperse particles < 1 μm at high sound frequencies, increasing with increasing particle size. It is not of significant influence when the orthokinetic collision prevails. It is based on the asymmetry of the air flow field around a moving particle at mean and high Reynolds numbers. Particles are excited by the sonic field and move, air wake is created, the pressure drops behind the particle (wake area), and causes particle attraction in the wake area (perpendicular to flow field) and particle repulsion (in line to flow field), and temporary pseudo-agglomerates form.

Factors influencing acoustic agglomeration are the sound frequency, the sound pressure level, and the particle sizes. For orthokinetic collision, sound frequencies around 50 Hz ~ 500 Hz are more effective, while for the acoustic wake effect the effect increases with frequency, being more effective at frequencies above 800 Hz. For both types of agglomeration, the interparticle distance that in the event of a collision leads to agglomeration increases exponentially with SPL. The acoustic wake effect increases with particle size, while for orthokinetic collision the effect is more pronounced for sizes around 2 μm (depending on frequency and relative particle sizes).

So, it is not a trivial problem and it is interesting to explore whether bell sounds can have an effect on the size distribution of atmospheric aerosols under ambient conditions. The present paper addresses the problem and is also a contribution towards a better understanding of the influence of ambient sounds on atmospheric aerosols. We present here calculations for acoustic orthokinetic agglomeration for different types of atmospheric particles by bell sounds. The reasons for the use of bell sounds in this work as agglomeration excitation input are many: Bell sounds are ubiquitous in many parts of the world [11-13], are quite loud, and can be heard at large distances. Additionally, they have a multitude of peak frequencies over a wide range of the audible spectrum, making the study interesting and more promising. When a bell is struck its sound has a number of simultaneously produced single frequency components generated by the excitation of normal modes of the particular bell. It has been shown [14,15] that the frequency spectra of bell-like sounds can be approximately described by a law of the form $f_{m.n} = c(m + bn)^p$ where m and n are non-negative integers while b, c and p are constants such that $1 \leq b \leq 2$ and $1.4 \leq p \leq 2.4$. Finally, using bell sound as the agglomeration excitation input, some insight might be attained on earlier notions that bell sounds might influence atmospheric properties.

2. Materials and Methods

2.1 Bell Sound Measurements

The bell sound measurements (Figure 1) were made in Xanthi at distances 40 m, 80 m and 170 m from the bell of St. Prodromos church with a Casella CEL 490 sound level meter combined with a Casella CEL 920 frequency analyzer. The particular church bell provides the advantage of being in the old part of the city which is under historical conservation status and hence traffic and other anthropogenic sounds are very limited.

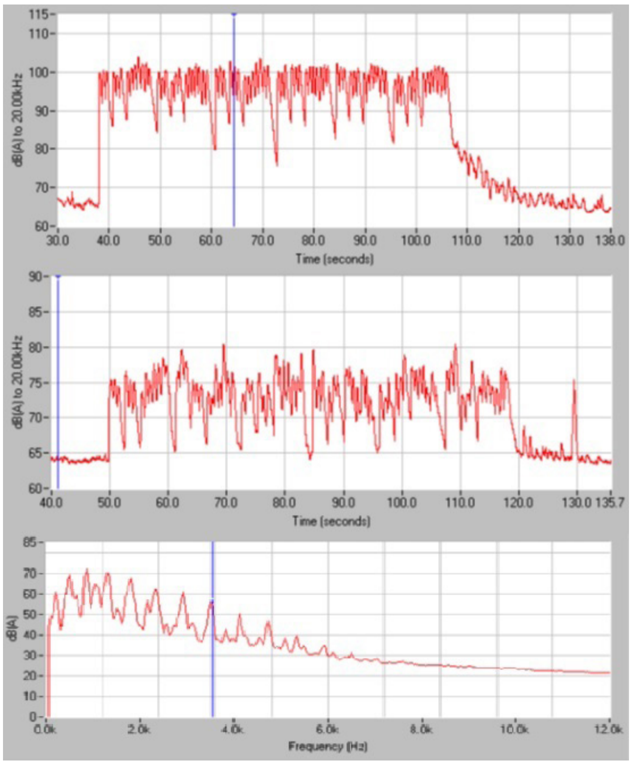

Figure 1. SPL at 40 m (top) and 170 m (middle) from the bell, and frequency spectrum up to 12 kHz (bottom) of the bell of St. Prodromos Church. Note the different y-axis scales of the panels.

2.2 Calculations of Acoustic Agglomeration

As Rayleigh showed in 1879 [16], the fundamental vibration frequency of a droplet of radius r_0 is $\omega_0 = (2\sigma/\pi^2\rho r_0^3)^{1/2}$, where σ is the surface tension and ρ is the density of the fluid. The resonance of particles in a sonic field can be characterized by the resonance rate $\eta = U_p/U_o = 1/[sqr(1+(\omega\tau_p)^2)]$ [17-20] with η being the resonance rate with values from 0 (no resonance) to 1 (complete resonance) and ω the radial velocity of the sound wave, $\omega=2\pi f$. U_p and U_o are representations of the particle and fluid velocity, respectively, and τ_p is the relaxation time of the particle, i.e. the time the particle needs to react to an external influence, in our case the sonic field, $\tau_p = 2\rho\omega r^2/9\mu$, μ being the dynamic viscosity of the fluid.

Effective agglomeration length, L_{eff}, is the maximum interparticle distance that in the event of a collision leads to agglomeration. $L_{eff} = \varepsilon\cdot L$, where ε is the collision efficiency $0<\varepsilon<1$ and L is the maximum interparticle distance that can cause collision.

For the calculation of the orthokinetic effective agglomeration length $L_{eff} = \varepsilon\cdot L$ we used first $U_g = [10\text{^}(SPL-94)/20]/(c_0\rho_0)$ which gives the range of oscillation speed of the excited medium [21], with c_0 the speed of sound in air. Then, we calculate the relative resonance between two particles $\eta_{12} = \omega(\tau_1-\tau_2)/sqr[1+(\omega\tau_1)^2(\omega\tau_2)^2]$, where τ_1, τ_2 are the relaxation times of the two particles. The collision efficiency ε can then be calculated from $\varepsilon = [St/(St+A)]^B$ with A = 0.65, B = 3.7 constants [22], and St the Stokes number $St = \rho_p\eta_{12}U_g d_2^2/18\mu d_1$, and the maximum separation distance between two oscillating particles of different size L can be calculated from $L = |x_{p2}-x_{p1}| = \eta_{12}U_g/\omega$, with x_{p2}, x_{p1} being the displacement range of the small and large particle, respectively.

3. Results and Discussion

At distances 40 m, 80 m and 170 m from the bell, the respective mean SPL was 90, 82 and 74 db[A]). Higher SPLs are observed in the range 20 Hz to 2 kHz (Figure 1), while the range of the bell frequency extends beyond 12 kHz.

We performed a range of calculations to study the impact of bell sound on aerosol agglomeration under ambient conditions [23]. For the concentrations and size ranges of particulate matter, we used data reported for Athens [24]. For Athens, the dominant range for number concentrations is 0.11 μm ~ 0.28 μm and > 10 μm for volume concentrations. So, for the large particles we use d_1 = 10 μm and for the small particles d_2 = 0.11 μm or d_2 = 0.28 μm. The number concentrations have been set at 2×10^6 particles/lt. For the mass density of particles we use 1000 kg/m^3 (density of water, representing liquid particles) and 2500 kg/m^3 (mean density of limestones, representing dust particles). For resonance rate calculations with constant particle diameter we use sound frequencies ∈ [20 Hz ~ 20 kHz], range of aerodynamic diameters between 0.01 μm ~ 40 μm, potential air viscosity μ = 18.27 μPa s and air density ρ_g = 1.2 kg/m^3.

The resonance rate results (Figure 2) show that lower frequencies are more effective at inducing resonance than higher ones. They also show that the lighter liquid particles have higher resonance rates than the heavier dust ones at any given frequency in the range 20 Hz ~ 20 kHz. We observe complete resonance up to very high sound frequencies for very fine particles with aerodynamic diameters 1 μm or less. For very low f = 50 Hz, liquid particles up to 28 μm and dust particles up to 18 μm have resonance rates > 0.8. At 150 Hz, liquid particles up to 16 μm and dust particles up to 10 μm have resonance rates > 0.8, while at 500 Hz, liquid particles up to 10 μm and dust particles up to 5.6 μm, respectively, have resonance rates > 0.8. Hence, the frequency spectrum of a bell, especially its lower part, can induce resonance to a variety of particle sizes and may have the potential to cause agglomeration if the SPL is high enough.

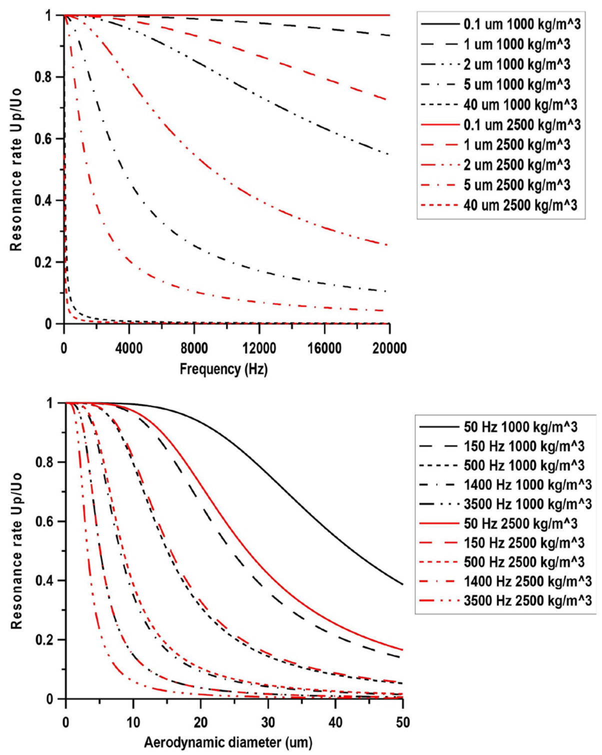

Figure 2. Upper panel: Resonance rate as a function of sound frequency and particle diameter for particle mass densities of 1000 kg/m^3 (black lines) and 2500 kg/m^3 (red lines). Lower panel: Calculations of resonance rate with constant sound frequency for particle mass densities of 1000 kg/m^3 and 2500 kg/m^3.

Now we calculate the effective agglomeration length for a large particle d_1 = 10 μm and a smaller one d_2 = 0.28 or d_2 = 0.11 for the SPLs at the different frequencies observed 40 m from the bell (Figure 1). The effective agglomeration length results show that L_{eff} is between 10^{-15} μm and 10^{-28} μm for f < 6000 Hz and even smaller for higher frequencies (Table 1). For particle number concentrations near 2 × 10^6 particles/lt, the interparticle distance at rest is 800 μm, hence, particle agglomeration in the atmosphere of Xanthi under the bell influence does not seem possible under these conditions, as the interparticle distance is orders of magnitude larger than L_{eff}.

Now we study two cases at high SPL = 160 dB. We use again ρ= 1000 kg/m^3 for liquid particles or 2500 kg/m^3 for dust particles, and f ∈ [250 Hz ~ 9200 Hz]. Case 1 (Figure 3, upper panel): For particles with diameters d_1 = 10 μm, d_2 = 0.28 μm, L_{eff} is in the range 0.07 μm ~ 14.7 μm, which is much smaller than the inter-particle distance of 800 μm at 2×10^6 particles/lt. If $N_{aerosol}$ = 10^9 particles/lt, i.e. very polluted conditions, the inter-particle distance becomes 100 μm, which is again larger than L_{eff} even at low frequencies.

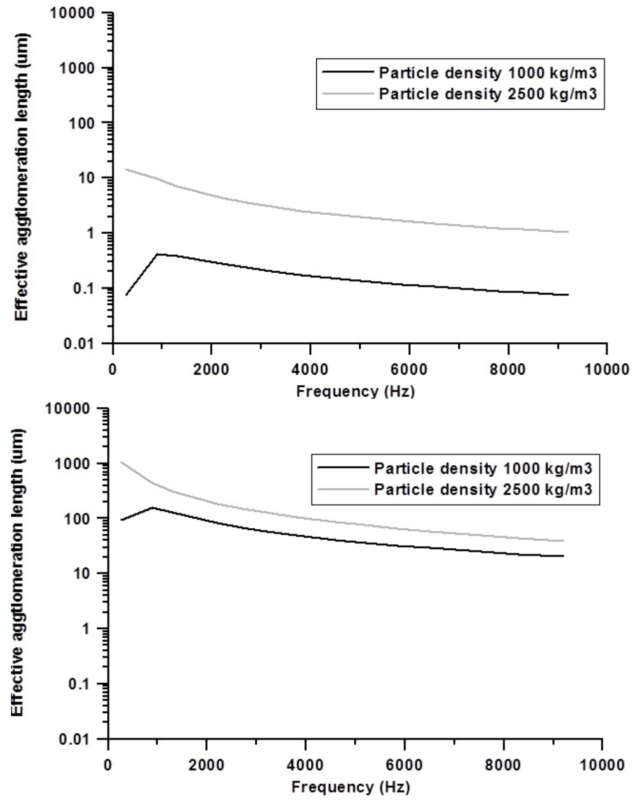

Figure 3. Calculation of the effective agglomeration length versus frequency for Case 1 (upper panel) and Case 2 (lower panel) for particle mass densities of 1000 kg/m^3 and 2500 kg/m^3. See text for explanation of Case 1 and Case 2 conditions.

Case 2 (Figure 3, lower panel): For particles with diameters d_1 = 10 μm, d_2 = 1 μm, L_{eff} is in the range 20 μm ~ 1076 μm. For dust particles and frequencies < 4000 Hz (which is the range of maximum SPL of the bell), L_{eff} is above the inter-particle distance of 800 μm (2×10^6 particles/lt) at frequencies < 500 Hz. At very polluted conditions (10^9 particles/lt), where the interparticle distance becomes 100 μm, L_{eff} for dust particles is larger than the interparticle distance for all frequencies < 4000 Hz and L_{eff} for liquid water particles is larger than the interparticle distance for frequencies in the range 500 Hz ~ 1500 Hz. Hence, at very close distances near the bell (a few centimeters), where SPL can be near 160 dB, agglomeration of particles becomes possible.

Table 1. Effective agglomeration length (L_{eff}, in μm) calculations[1]. Particle density is denoted by ρ.

	d_2=0.28		d_2=0.11 μm	
	ρ=2500 kg/m^3	ρ=1000 kg/m^3	ρ=2500 kg/m^3	ρ=1000 kg/m^3
Min value	2.6×10^{-28}	8.7×10^{-30}	2.6×10^{-31}	8.6×10^{-33}
Max value	2.2×10^{-17}	1.1×10^{-19}	2.2×10^{-20}	1.1×10^{-22}

[1]Potential air viscosity μ=18.27 × 10^{-6} Pa s, air density 1.2 kg/m^3, sound velocity 344 m/s @20 ^{o}C, particle size d_1 = 10 μm, d_2 = 0.11 μm or 0.28 μm.

The results show under some circumstances noise can influence the aerosol pollution, through coagulation of particles, which will increase their size. This will have two consequences on the aerosol pollution: First, lower concentrations of small particles, which is of interest as smaller particles are of more concern to health. Second, as particles grow larger due to agglomeration, the might be removed gravitational more quickly from the atmosphere. Clearly, more research is needed in this direction to clarify the matter. In future work we plan to access the agglomeration potential for a wider range of particle sizes. Also, there are still open questions which could be addressed in the future: 1) Are there other atmospheric conditions regarding SPL, sound frequency spectrum and aerosol characteristics that can cause agglomeration under atmospheric conditions? Thunder is an interesting candidate, as SPL can be very high [25], and, additionally, has frequency spectra with peaks around 50 Hz ~ 100 Hz [26], where orthokinetic agglomeration can be very effective. 2) Can other mechanisms of sound impact on particulates cause measurable modulations of aerosol size distributions under ambient conditions? It is known that liquid droplets can undergo deformation and breakup if exposed to a gas stream of sufficient velocity [27,28]. Especially for thunder, which is loud and occurs in cloud environments where large numbers of droplets are present, this might be an interesting and important mechanism.

4. Conclusions

The aerosol characteristics (size distribution, number density) in the atmosphere of Xanthi, as in most small towns in Europe, are not ideal for acoustic agglomeration under church bell sound. Church bell spectra have ideal frequencies to cause acoustic agglomeration but the SPL of the bell at distances larger than a few cm from the bell is prohibitive for acoustic agglomeration. At very close distances however, SPL can be large enough for acoustic agglomeration, especially under very polluted conditions. In this case, dust particles agglomerate more readily than liquid particles.

Author Contributions

Konstantinos Kourtidis performed the theoretical work, the bell sound measurements, and wrote the manuscript. Ageliki Andrikopoulou performed the calculations.

Conflict of Interest

No conflict of interest.

Funding

This research received no external funding.

References

[1] Oddie, B.C.V., 1965. The hail cannon, an early attempt at weather control. Weather. 20, 154-156.

[2] Changnon, S.A. Jr., Ivens, J.L., 1981. History Repeated: The Forgotten Hail Cannons of Europe. Bulletin of the American Meteorological Society. 62(3), 368-375.

[3] Wieringa, J., Holleman, I., 2006. If cannons cannot fight hail, what else? Meteorologische Zeitschrift. 15(6), 659-669.
DOI: https://doi.org/10.1127/0941-2948/2006/0147

[4] Scott, D.S., 1975. A new approach to the acoustic conditioning of industrial aerosol emissions. Journal of Sound and Vibration. 43(4), 607-619.

[5] Hoffmann, T.L., Koopmann, G.H., 1996. Visualization of acoustic particle interaction and agglomeration: Theory and experiments. The Journal of the Acoustical Society of America. 99, 2130.
DOI: https://doi.org/10.1121/1.415400

[6] Gallego-Juárez, J.A., De Sarabia, E., RodrÍguez-Corral, G., et al., 1999. Application of Acoustic Agglomeration to Reduce Fine Particle Emissions from Coal Combustion Plants. Environmental Science & Technology. 33(21), 3843-3849.
DOI: https://doi.org/10.1021/es990002n

[7] Ng, B.F., Xiong, J.W., Wan, M.P., 2017. Application of acoustic agglomeration to enhance air filtration efficiency in air-conditioning and mechanical ventilation (ACMV) systems. Plos one. 12(6), e0178851.
DOI: https://doi.org/10.1371/journal.pone.0178851

[8] Riera, E., González, I., Rodríguez-Corral, G., et al., 2015. Ultrasonic agglomeration and preconditioning of aerosol particles for environmental and other applications. Gallego-Juárez, J.A., Graff, K.F. (Eds.),

Power Ultrasonics; Woodhead Publishing. pp. 1023.
DOI: https://doi.org/10.1016/B978-1-78242-028-6.00034-X

[9] de Sarabia, E., Gallego-Juárez, J.A., Rodríguez-Corral, G., et al., 2000. Application of high-power ultrasound to enhance fluid/solid particle separation processes. Ultrasonics. 38, 642-646.
DOI: https://doi.org/10.1016/S0041-624X(99)00129-8

[10] González, I., Gallego-Juárez, J.A., Riera, E., 2003. The influence of entrainment on acoustically induced interactions between aerosol particles—an experimental study. Journal of Aerosol Science. 34, 1611-1631.
DOI: https://doi.org/10.1016/S0021-8502(03)00190-3

[11] Kim, S.H., Lee, C.W., Lee, J.M., 2005. Beat characteristics and beat maps of the King Seong-deok Divine Bell. Journal of Sound and Vibration. 281, 21-44.

[12] Samolov, A., 2010. Analysis of just Noticeable Difference in Spectrum of Church Bell Sound. Telfor Journal. 2(2), 82-85.

[13] Zhang, D., Kong, K., Zhang, M., et al., 2020. Courtyard Sound Field Characteristics by Bell Sounds in Han Chinese Buddhist Temples. Applied Sciences. 10, 1279.
DOI: https://doi.org/10.3390/app10041279

[14] Perrin, R., Charnley, T., Banu H., et al., 1985. Chladni's law and the Modern English Church Bell. Journal of Sound and Vibration. 102, 11-19.

[15] Swallowe, G.M., Charnley T., Perrin, R., 1993. New Musical Scales. The Journal of the Acoustical Society of America. 94, 1166-1167.

[16] Rayleigh, J.W.S., 1879. On the capillary phenomena of jets. Proceedings of the Royal Society of London. 29, 71-97.

[17] Brandt, O., Freund, H., Hiedemann, E., 1937. Suspended matter in a sound field. Zeitschrift fuer Physik. 104, 511-533.

[18] Temkin, S., Leung, C.M., 1976. On the velocity of a rigid sphere in a sound wave. Journal of Sound and Vibration. 49(1), 75-92.

[19] Hoffmann, T.L., Koopmann, G.H., 1997. Visualization of acoustic particle interaction and agglomeration: Theory evaluation. The Journal of the Acoustical Society of America. 101, 3421.
DOI: https://doi.org/10.1121/1.418352

[20] González, I., Hofmann, T.L., Gallego-Juarez, J., 2000. Precise measurements of particle entrainment in a standing-wave acoustic field between 20 and 3500 Hz. Journal of Aerosol Science. 31, 1461-1468.

[21] Noorpoor, A.R., Sadighzadeh, A., Habibnejad, H., 2012. Experimental Study on Diesel Exhaust Particles Agglomeration Using Acoustic Waves. International Journal of Automotive Engineering. 2(4), 252-260.

[22] Loeffler, F., 1988. Staubabscheiden; George Thieme Verlag: Stuttgart-New York.
DOI: https://doi.org/10.1002/star.19890410313

[23] Andrikopoulou, A., 2013. A study of the influence of sound level pressure variations on the levels and size disributions of atmospheriuc aerosols. M.Sc. Thesis, Department of Environmental Engineering, Demokritus University of Thrace.

[24] Flocas, H., Asimakopoulos, V.D., Helmis, C.G., 2006. An experimental study of aerosol distribution over a Mediterranean area. Science of the Total Environment. 367, 872-887.

[25] Few, A.A., Dessler, A.J., Latham, D.J., et al., 1967. A Dominant 200-Hertz Peak in the Acoustic Spectrum of Thunder. Journal of Geophysical Research. 72(24), 6149-6154.

[26] Bodhika, J.A.P., Fernando, M., Cooray, V., 2014. A preliminary study on characteristics of thunder, pulses of lightning. 2014 International Conference on Lightning Protection (ICLP), Shanghai, China. pp. 260-264.

[27] Wierzba, A., 1990. Deformation and breakup of liquid drops in a gas stream at nearly critical Weber numbers. Experiments in Fluids. 9, 59-64.
DOI: https://doi.org/10.1007/BF00575336

[28] Guildenbecher, D.R., López-Rivera, C., Sojka, P.E., 2011. Droplet Deformation and Breakup. Ashgriz N. (eds) Handbook of Atomization and Sprays. Springer, Boston, MA.
DOI: https://doi.org/10.1007/978-1-4419-7264-4_6

Journal of Atmospheric Science Research
https://ojs.bilpublishing.com/index.php/jasr

ARTICLE

Ensemble Cloud Model Application in Simulating the Catastrophic Heavy Rainfall Event

Vlado Spiridonov[1] Mladjen Curic[2] Marija Grcic[3] Boro Jakimovski[4]

1. Faculty of Natural Sciences and Mathematics, "Ss Cyril and Methodius" University – Skopje, Macedonia
2. Physical Faculty, Institute of Meteorology, University of Belgrade, R. Serbia
3. Independent scholar, Vienna, Austria
4. Faculty of Computer Sciences and Engineering, "Ss Cyril and Methodius" University – Skopje, Macedonia

ARTICLE INFO

Article history
Received: 22 September 2022
Revised: 18 November 2022
Accepted: 21 November 2022
Published: 30 November 2022

Keywords:
WRF triple nested model
Convective cloud model
Ensemble initialization
3-D numerical simulation
Flash-flood event
Super-cell storm

ABSTRACT

An attempt has been made in the present research to simulate a deadly flash-flood event over the City of Skopje, Macedonia on 6 August 2016. A cloud model ensemble forecast method is developed to simulate a super-cell storm's initiation and evolutionary features. Sounding data are generated using an ensemble approach, that utilizes a triple-nested WRF model. A three-dimensional (3-D) convective cloud model (CCM) with a very fine horizontal grid resolution of 250-m is initialized, using the initial representative sounding data, derived from the WRF 1-km forecast outputs. CCM is configured and run with an open lateral boundary conditions LBC, allowing explicit simulation of convective scale processes. This preliminary study showed that the ensemble approach has some advantages in the generation of the initial data and the model initialization. The applied method minimizes the uncertainties and provides a more qualitative-quantitative assessment of super-cell storm initiation, cell structure, evolutionary properties, and intensity. A high-resolution 3-D run is capable to resolve detailed aspects of convection, including high-intensity convective precipitation. The results are significant not only from the aspect of the cloud model's ability to provide a qualitative-quantitative assessment of intense precipitation but also for a deeper understanding of the essence of storm development, its vortex dynamics, and the meaning of micro-physical processes for the production and release of large amounts of precipitation that were the cause of the catastrophic flood in an urban area. After a series of experiments and verification, such a system could be a reliable tool in weather services for very short-range forecasting (now-casting) and early warning of weather disasters.

*Corresponding Author:
Vlado Spiridonov, "Ss. Cyril and Methodius" University - Skopje.
Faculty of Natural Sciences and Mathematics, Institute of Physics-Meteorology
E-mail : vlado.spiridonov@pmf.ukim.mk

DOI: https://doi.org/10.30564/jasr.v5i4.5081

1. Introduction

Numerous studies have shown that timescale atmospheric non-hydro static models are reliable tools for forecasting severe convective systems, their initiation, and evolution, but they tend to underestimate the intensity of convective rainfall and their right location. This uncertainty mainly origins from the nonlinear atmospheric nature, small-scale convective processes as well as the initial conditions (IC), lateral boundary conditions (LBC), model configuration, horizontal grid resolution, choice of microphysics, treatment of convection, parameterize, and other factors [1,2]. Many studies have focused on the effect of horizontal grid resolution, to improve the convective precipitation, forecast [3-7]. The first numerical simulation with an explicit treatment of convection using a temporal timescale model was performed by Bernadet, et al. [6].

In addition to the approach to the better discretionary of the grid of points [8] also estimated that the forecast of convective systems also depends on surface processes such as differential heating, and soil moisture, which affects the perturbation of temperature and pressure, and affects the dynamic effect of voracity in the boundary layer, which are responsible for initiating convection. Other studies [9-11] were also conducted, which were devoted to the investigation of the physical processes of convective storms, which used the Weather Research Forecast Non-Hydrostatic Mesoscale Model WRF-NMM [12]. Further efforts were to develop an efficient and flexible system based on the Weather Research and Forecasting (WRF) model configuration [13] with the optimal 4-km resolution, with the corresponding microphysics, and the surface characterizations schemes for the treatment of the planetary boundary layer (PBL) processes, radiation schemes, including an explicit treatment of moist convection—avoiding cumulus characterization [14]. Some studies indicated that the deterministic forecasts of convective systems produced with heavy rainfall could be also improved by the increase in resolution. Weisman, et al. [15] showed an advantage in forecasting different modes of convection, using the WRF 4-km run, with an explicit treatment of the convection. However, uncertainty, when it came to the precise location and intensity of convective precipitation remained. Research has also shown, that with an increase in resolution, there may be an increase (overestimation) of convective precipitation or a delay in the onset of convection [16-20]. To adequately address the problem related to uncertainty in the initial data and to improve the forecast accuracy of convective rainfall, a new ensemble technique was initiated and applied in real-time storm forecasting [21]. A fine convective-permitted 1-km resolution has been applied in the Advanced Regional Prediction System (ARPS) [22], as part of the National Oceanic and Atmospheric Administration (NOAA) 2008 Spring Experiment. Elmore, et al. [23] developed an ensemble approach to forecasting thunderstorms. The results showed that this system has an advantage in forecasting different modes of convection, during the thunderstorm life cycle. There is no doubt that the ensemble approach is more reliable, but a computationally more expensive method, that mostly depends on computer performance. However, numerous experiments and sensitivity tests showed, that by appropriate model setup and turning to a fine grid discretionary (from 4 km to 1 km), a more reliable forecast of convective systems could be achieved. Many other studies [24-26] focused on evaluating various nested WRF model configurations in the simulation of severe convective weather and flash floods, which occurred in different geographic regions. In addition, real-time convection-allowing ensemble forecasts, are conducted in the frame of the NCAR's experiment [27]. In addition, Zittis, et al. [28] showed in their work that the WRF model configured in this way can successfully forecast extreme precipitation over the Mediterranean. Considering the importance of small-scale convective processes on the evolution of the system and the formation of intense precipitation in many centers, the development of numerical prognostic systems that use modern convective-scale data assimilation techniques and a very fine resolution of 1 km grid points in routine forecasting [29]. In doing so, the ensemble approach is also used in providing the initial data and model initialization, or they use several models with the same initial fields. The verification showed that the numerical forecast of convective scales could forecast different modes of convection but failed to accurately predict extreme cases related to the accurate forecast of location and relative intensity of heavy rainfall, which we already have mentioned. To address this problem to some extent [30] proposed a method of coupling the WRF model and the cloud model for detailed qualitative-quantitative assessments of extreme convective precipitation. The cloud model was initialized using a homogeneous horizontal field applying the standard perturbation technique and the single vertical meteorological profile based on WRF model outputs. Recently, a diagnostic tool has been developed, based on selected complex instability criteria [31], for more accurate convective-scale forecasts and severe weather alerts.

The present study is focused on a catastrophic flash-flood event that occurred on 6 August 2016 in the city of Skopje. The flash flood that happened in urban areas had catastrophic consequences because it took human lives and caused great material damage. For these reasons, it is very important to evaluate each severe weather event, especially in the era of accelerated climate changes and the increased frequency of weather extremes. In this context, the study by Milevski [32] provided an overview of natural disasters in Macedonia, with a special emphasis on the torrential flash-flooding event over Skopje. There is also a diagnostic overview of the extreme case of flooding in Skopje [33] and an overview of possible morphological, hydro-logical, and other risks for sudden flooding. The main goal of this research is to examine the possibility of the connective cloud model in the simulation of the super-cell storm evolved from a limescale convective system MCS, which produced heavy rainfall and caused a catastrophic flash flood in Skopje on August 6, 2016. The main goal of the present research was to evaluate the cloud model performances in a more realistic simulation of the super-cell storm evolution and its skill in a more accurate quantitative assessment of heavy rainfall. Section 1, in addition to the synoptic overview, provides a brief description of the urban flash flooding event, with catastrophic consequences. The next section is devoted to the description of the forecasting system, the ensemble technique, and the cloud model overview. The main results are shown and discussed in the next chapter, where the main conclusions are given about the performance of the system and its potential advantages in making quantitative forecasts and the most abundant convective precipitation.

2. Observational Analysis

On August 6, 2016, the Skopje city area and its surroundings were hit by very severe convective weather which took on the dimensions of a devastating super-cell storm with intense rainfall (Figure 1a) a flash flood caused the loss of 23 human lives and caused significant material damage. However, considering that the intense development of the storm occurred over a very specific topography shown in (Figure 1b) where there is no observation, most likely more convective precipitation fell. The total estimated amount of rainfall evidenced within 2 hours reached about 100 mm. Figure 2a illustrates the consequences of a flash flood, especially in the vicinity of the ring road, the most affected area. A significant amount of rainfall was recorded in Skopje, Macedonia on 6 Aug 2016. The local maximum value of 106.3 mm was measured at the automated meteorological station AWS- "Gazi Baba", located northeast of Skopje valley in the vicinity of the most affected area. The heavy rainfall period occurred from 1530 UTC to 1640 UTC with a peak rainfall intensity evidenced at 1550 UTC (Figure 2b) recorded at AWS - "Gazi Baba" in the vicinity of the most affected flooding area.

Analysis of the observational material points to several interesting details. On 6 August 2016 at noon UTC, the cut-off low positioned over the Ionian Sea was approaching from the southwest. It is seen that there is no

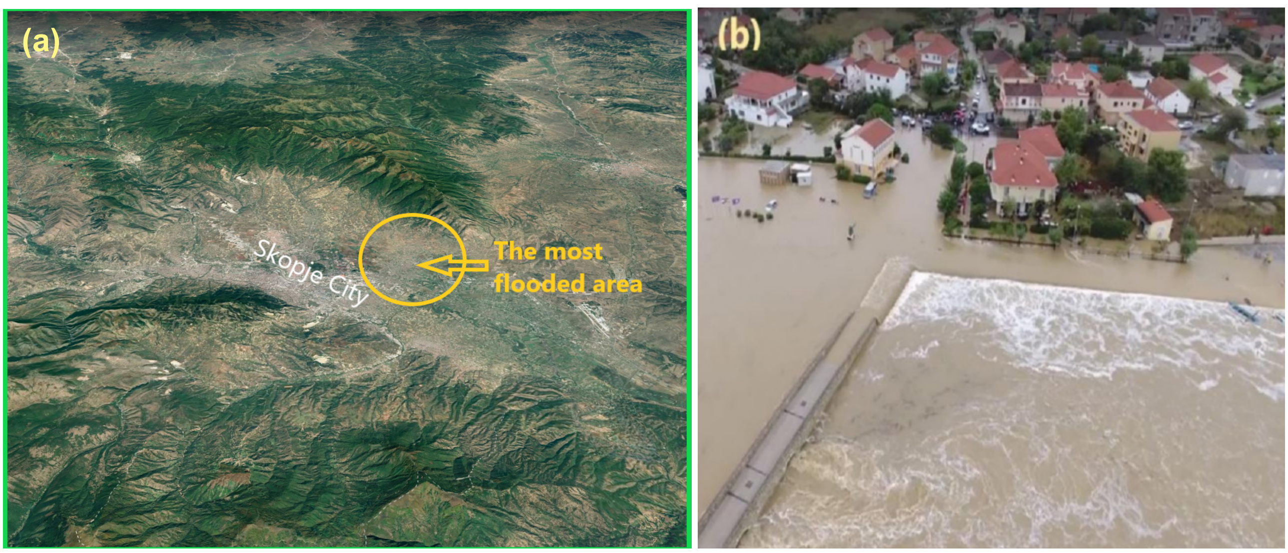

Figure. 1 (a) Geographic map of Skopje valley and the surrounding mountains. A white circle denotes a flash-flood heavy rainfall area. (b) Photo of the most affected flooding area, located northeast of Skopje, around the ring road. (Credit: WMO).

pronounced carcinogenicity or significant convection of positive voracity, which could contribute to the development of convective systems. The mean-sea level pressure distribution shown in Figure 3a and the ISO-potentiality field patterns at 500 hPa (see Figure 3b), favor a warm and moist air convection across the western part of Macedonia. Under such conditions, the individual convective cells were initiated, helped by orographic forcing, and gravity-produced waves associated with the mountain-induced timescale convective system. This long-lasting convective disturbance in the afternoon hours over Skopje valley transformed into a limescale convective vortex (a mid-level, warm-core low-pressure center) of a limescale convective system (MCS) because of favorable topographical characteristics of the area, surface wetness, differential heating, and the latent heat release over a longer period.

This implies that heavy convective precipitation is formed due to a locally forcing environment that is not the result of a synoptic-driven system. From the satellite image, two convective systems can be distinguished, one around the Ionian Sea in the high-altitude cyclone (the center of low pressure), and the other that extends NE to NW of Macedonia, due to a prefrontal disturbance. Regarding the atmospheric lighting (see Figure 3d), the atmosphere above the urban area was very unstable and active, so more than 1000 lightning were registered in a very short period.

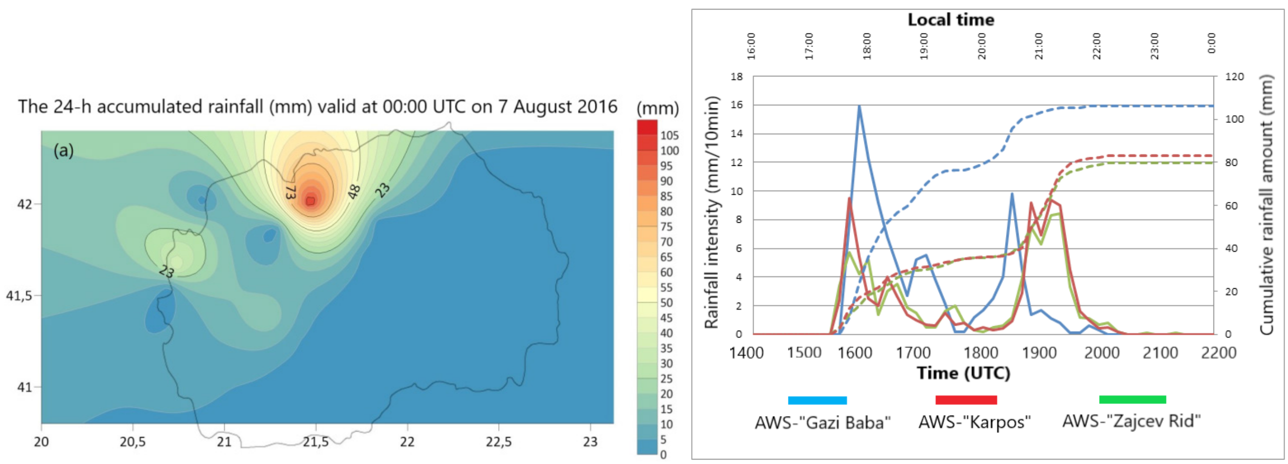

Figure 2. (a) An isohyet chart with a total 24-h accumulated rainfall (mm) in Macedonia valid at 0600 UTC on 7 Aug 2016. (b) Rainfall intensity (mm/10min) obtained at the AWS- "Gazi Baba" whose position is closer to the main target area (blue curve), AWS- "Karpos" located in the central part of Skopje City (red curve), and AWS- "Gazi Baba" located westerly from the target area at the Hydrometeorological Service of Macedonia (HSM). The dotted lines represent a cumulative rainfall amount registered for the 24 hours.

3. The Design of the System

For cloud initialization, the perturbation method is usually used, which is an approximation for the missing information about temperature deviations (deviations) when initiating the development of a convective cell, in the center of a thermal balloon with a certain radial dimension and the center is positioned above the ground. Initial vertical fields of meteorological parameters, taken from sounding or prognostic model output in the selected area, by users. horizontally homogeneous environment. In this research, the ensemble approach is used in the initialization of the cloud model, which implies the run of the model based on prognostic soundings obtained with the help of the WRF model in several network points in the selected domain of interest. In this way, a more average representative cloud development is obtained, which uses the disturbance of the basic state of the atmosphere in a smaller domain.

3.1 Numerical Model Description

The numerical experiments have been performed using the Advanced Research version of the WRF triple nested model, version 4.0 [1, 13]. The parent domain (D1) with a horizontal grid resolution of 10 km covers the Southeast Europe SEE domain. The first inner nested domain (D2) with a grid spacing of 3.3-km captures the whole territory of Macedonia (Figure 4a). A 1.1-km nested domain (D3) is positioned in the northeast position of D2 in the most flooded area (Figure 4b). The initial conditions (IC) and the lateral boundary conditions (LBCs) are taken from the National Center of Environmental Prediction, Global Forecast Model (NCEP GFS) with a resolution of 0.25 deg at 3-h intervals.

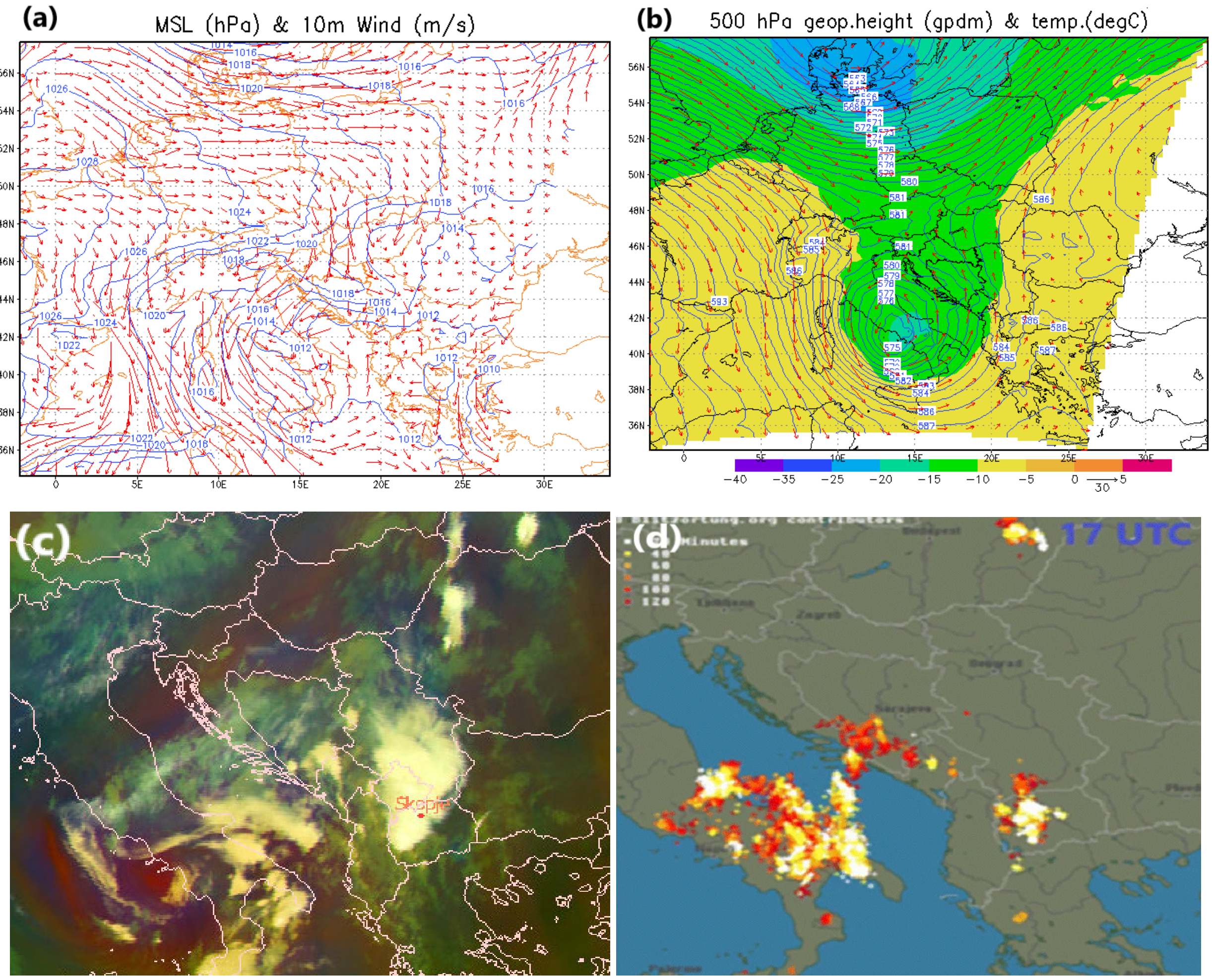

Figure 3. (a) MSL pressure chart valid on 6 Aug 2016 12:00UTC. (b) The 500 hPa geopotential height (gpdm) and the temperature (ºC), valid on 6 Aug 2016 at noon UTC. (c) Meteosat-10 Airmass RGB, valid on 6 August 19:30 UTC. (d) The real-time lightning map, valid on 6 Aug 2016 at 17:00 UTC.

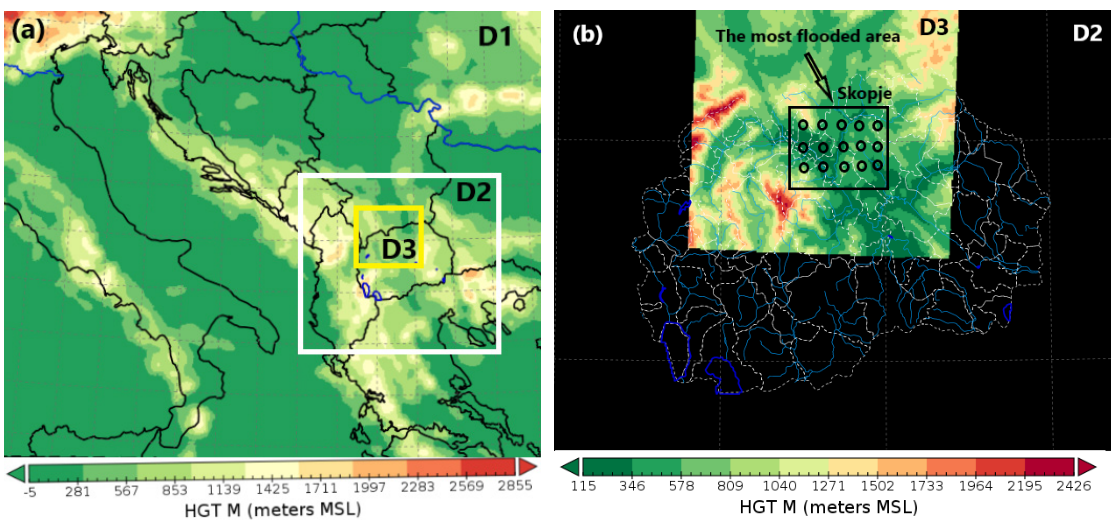

Figure 4. System design. (a) A triple-nested model configuration. (b) Schematic of ensemble generation approach. Vertical meteorological profiles are derived from the WRF 1.1-km nested run (domain 3), in three consecutive hourly outputs of the WRF model, taken during the period of intensive development of the convective system. Note: Skopje is labeled in the center of the inner plotted area which denotes the heaviest flooding area. Dotes indicate grid points from which soundings are generated.

3.2 Ensemble Approach

The initial conditions for running the cloud model are obtained from the WRF 1.1-km forecast outputs in a period of intense convective activity and heavy rainfall. The fifteen soundings are extracted from a grid spacing of 0.05 º E-W × 0.05 º N-S on the area of interest. The soundings are derived from the 00:00 UTC WRF run (+24 hours) that verify at three successive times at 1500, 1600, and 1700 UTC, which coincides with a period of intense convection. Thus, the system contains 15 sounding at every three times, or 45 -ensemble members. Such design using forecast soundings over the spatial domain of interest, to the extent level minimizes the effect of uncertainty in the initial conditions and cloud model initialization [23]. Such design of the system, illustrated in Figure 4b is applicable across the entire cloud model domain, as the result of implicit recognition of spatial and temporal uncertainty in the forecast sounding. In this way, the perturbation technique could be avoided, as the cloud model initialization is less dependent on the modeler. This advanced approach is more suitable for the initiation of the convection, and it is a highly unstable atmosphere to trigger a severe convective storm.

3.3 A Three-dimensional Cloud Model Setup

A cloud-resolving model (CRM) is a three-dimensional (3-D), non-hydrostatic, time-dependent system, with dynamics, thermodynamics, and cloud microphysics [34-36]. The present version of the model contains ten prognostic equations: three momentum equations, the pressure, and thermodynamic equations, four continuity equations for the water substances, and a sub-grid kinetic energy equation.

Three-dimensional simulations are performed within a small model integration domain, with a size of 50×50×15 km^3 that covers the most flooded area and suburbs of Skopje city. The horizontal grid resolution is 500-m while the vertical discretionary is 250-m, respectively. The refined vertical grid resolution of 50 m grid length near the surface layer resolves boundary layer structures. The total number of grid points in a 3-D simulation is 201×201×66. The time step of the model is 5 s and the smaller one is 0.5 s for solving the sound waves. The cloud model is integrated for a 2-hour simulation to capture the life cycle of this very severe convective case. Model equations are solved on a semi-staggered grid. Since the model equations are compressible, a time-splitting procedure with a second-order leapfrog scheme is used for the portions that do not involve sound waves to achieve numerical efficiency. The lateral boundaries are open and time-dependent, so disturbances can pass through with minimal reflection. Crucially, the cloud model's open lateral boundary conditions allow it to freely evolve and produce strong net ascent/convergence/divergence across its domain, without being constrained by LBCs from the WRF model. Initial conditions are taken by soundings derived from the WRF triple-nested (10 km × 3.3 km × 1.1 km) forecast outputs for the inner domain of WRF (D3). One forecast sounding, with a vertical profile of meteorological parameters (e.g., potential temperature, specific humidity, and horizontal wind components) represents an individual ensemble member (Figure 5). More detailed information about the WRF nested model configuration and the convective cloud model parameters could be found in Table 1.

Table 1. The list of WRF and Cloud Model Parameters

Parameter/Run	**WRF triple nested forecast**	**Cloud Resolving Model 3-D simulation**
Domain used and size	Domain 1 (parent) 10 km hor. grid res. Domain 2 (nested) 3.3 km Domain 3 (nested) 1.1 km	Covers domain 3
Model dynamics and thermodynamics	WRF-non-hydrostatic mesoscale model [13]	Klemp and Wilhelmson [34-35]
Microphysics	Thomson microphysics [37], Thompson microphysics scheme with aerosol climatology [38]	Orville and Kopp [36]
PBL scheme	Yonsei University YSU PBL Scheme [39]	Turbulent kinetic energy equation TKE with first-order closure
Land surface scheme	Noah's land-surface scheme [40]	Homogeneous field
Cumulus parameterization	Domain 1-scale and aerosol aware scheme NCEP GFS Cumulus Convection Scheme with scale and aerosol awareness [41, 42] Domain 2 and 3 Explicit treatments	Explicit treatment convection
Long wave radiation	Mlawer and Taubman [43]	

Table 1 continued

Parameter/Run	WRF triple nested forecast	Cloud Resolving Model 3-D simulation
Short wave radiation	Dudhia Scheme: Simple downward integration allowing for efficient cloud and clear-sky absorption and scattering. [44]	
Hor. grid resolution	10 km; 3.3 km; 1.1 km	0.5 km
Vertical discretization	50	0.250 km
Time step (DT)	60, 20, and 6.6 sec., respectively	5 sec
Time step for solving the sound waves (DTAU)		1 sec
Simulation time	24 hours	90 min
Total grid points (x,y,z) direction	120×120 91×121 121×121	100×100×66
Radial dimensions of thermal bubble		15 × 15 ×3.5 km^3
The maximum temperature perturbation		Ensemble approach
Lateral boundary conditions (LBC)	LBC at each 3-hrs	Opened LBC
Initial conditions/initial meteorological fields	NCEP GDAS/FNL GFS 0.25 deg LBC at every 3 hours	WRF output-derived soundings
Computing Processing Unit	26 CPU hours	90 CPU hours

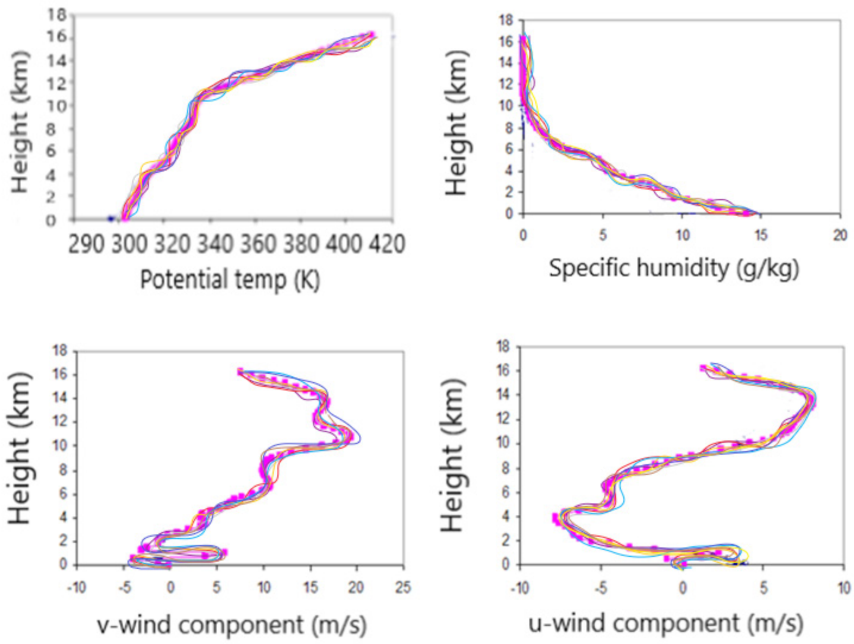

Figure 5. Initial vertical profiles of the equivalent potential temperature (θ_e), mixing ratio (q), horizontal (u) and (v) wind components, extracted from WRF 1.1 km scale forecast outputs

4. Results

The obtained results indicate that a 3-D run with an ensemble initialization demonstrated a high model skill and potential in the realistic simulation of a flash-flooding produced supercell storm that passed through a different phase of evolution and convective modes. The first part of this section deals with storm dynamics and the main triggering factors for convective cell initiation and evolution, during the life cycle. Then, the key micro-physical processes responsible for the formation of large water content and heavy rainfall are examined. Finally, the results are discussed in light of the comparative analysis with the available observations.

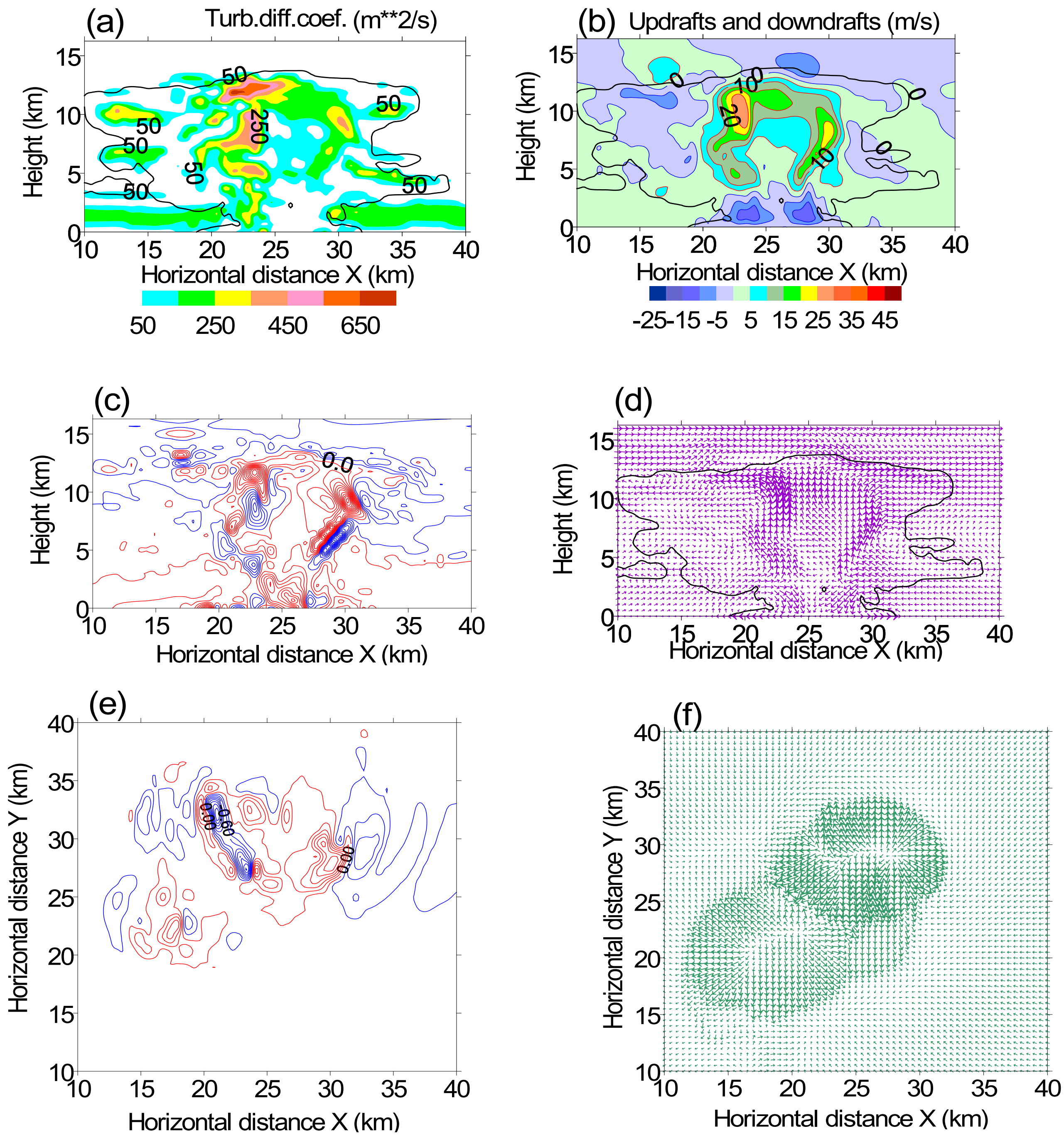

Figure 6. Dynamic characteristics of a super-cell storm in the most intense phase of development. (a) Vertical section of the turbulent diffusion coefficient. (b) Same as Fig. 6a, but for updrafts and downdrafts. (c) Same as Fig. 6a, but for the vertical component of relative voracity. (d) x-z cross-section of the vertical wind profile. (e) horizontal x-y cross-section of the vertical component of voracity at 2 km height. (f) Horizontal wind profile at ground level.

4.1 Super-cell Storm Dynamics

Turbulence plays a key role in convection, primarily through a process of turbulent mixing of updrafts with the surrounding air, which often has a low equivalent potential temperature. This reduces both the buoyancy force and the vertical velocity. Figure 6a shows the vertical profile of a turbulent diffusion coefficient derived from a turbulent kinetic energy equation. Weak to moderate turbulence occurs in the updraft portion of the simulated storm in the middle and upper troposphere. But what is indicative, is that the maximum turbulence coefficient value is evidenced in the forward flank core in the region of upward motions, on the edge of the updraft, which contributes to the significant hail growth. In the initial phase of cloud evolution, directional wind shear in the lower portions of the atmosphere, allows the horizontal component of voracity to transfer into a vertical component of voracity (ζ). At the place of intense convection, the vortex column of air ascends, maintaining the direction of rotation. This process is responsible for the formation of a pair of vertices with quasi-vertical axes, rotating in opposite directions. Such vertices are produced by linear effects. When precipitation and a downdraft form in such a storm, the vortex tube descends, and an additional pair of vertices is generated. This pair of vertices form as the result of non-linear effects, which later separate the single cloud mass into two separate cells. The disturbance of the voracity occurs due to the vertical wind shear-twisting term of the vortex tube. As it is shown in Figure 6c, a pair of vertices, with a positive disturbance of ($\zeta_t^{'}$), (left portion of updrafts) relative to the storm motion and a negative voracity disturbance (right portion of updrafts). The area with large values of vertical velocity is located near the top and bottom of the updraft, where maximum disturbance of voracity occurs (Figure 6b, d). In addition to the tilting term, the stretching term ($\zeta^{'} w_z$) becomes significant. The cloud model run was able to simulate a persistent rotating updraft with a lonesomeness, as typical for the development of a tornado super-cell. A divergence signature shown in Figure 6f, with two distinct cores occurs as the result of downdrafts (vertical columns of sinking air), observed in the mature phase of storm evolution at the onset of precipitation.

4.2 Evaluation of the Micro-physical Processes

Figure 7 shows the radar reflectivity fields for this specific case associated with a flood over an urban area due to a large amount of precipitation, with a strong intensity over a smaller area and for a very short period. In the first two columns, vertical and horizontal radar reflectivity profiles are shown in the most developed phase of the super-cell storm, at 1530 UTC; 1545 UTC; and 1600 UTC. The 3rd column in Figure 7, displays the horizontal transects of composite radar reflectivity patterns at 2 km altitude (Constant Altitude Plan Position Indicator-CAPPI). The strong convective cells that passed over the Skopje area, oriented in the SW-NE direction are captured well with the cloud model simulation. There is a large similarity in the simulated relative to the observed reflectivity patterns. The maximum radar reflectivity value of 70 db Z recorded at 1545 UTC, was successfully simulated with a cloud model. In addition, the bow-echo signature that is visible on the vertical transects of the reflectivity field (1545 UTC) along the NW-SE direction, as well as the specific hook shape of the radar reflection on the horizontal view, clearly indicate the formation of a super-cell storm.

Micro-physical processes play a crucial role in the internal storm structure and distribution of hydrometers during the storm life cycle. The simulation in Figure 8 indicates a rapid super-cell storm evolution, micro physical transfer, and transformations among different phase transitions, associated with large water production and heavy rainfall occurrence. The simulation gives a clear micro physical picture of the dominant processes and nucleation phases that are initiated by the dynamics of the storm (rotating updrafts and lonesomeness, and strong ascent that keeps the ice structure at higher altitudes, as well as downdrafts in the heavy rainfall phase.

The simulation gives a clear micro physical picture of the dominant processes and nucleation phases that are initiated by the dynamics of the storm (rotating updrafts and lonesomeness, and strong ascent that keeps the ice structure at higher altitudes, as well as downdrafts in the heavy rainfall phase. It is seen that in a very short time the simulation period of 20-32.5 min, which corresponds to the time from 1545 UTC to 1600 UTC, intense processes of formation of cloud elements, and ice structures take place, snow, and cloud ice in the upper part of the cloud, hail along two ascending areas of updrafts in the central inflow region, and raindrops in the lower part of the atmosphere. At about 22.5 min simulation time, a new cell develops in the front right wing, which gradually strengthens and contains only super cooled water and snow and ice crystals and gradually merges with the leading cloud.

A few minutes later (25 min.) downdrafts begin with updrafts, so that the core of the city gradually descends, intensifying the process of rain formation through accretion and ice melting so that the first precipitation on the surface is also registered. 27.5 min is the most intense development with two formed channels and heavy rain

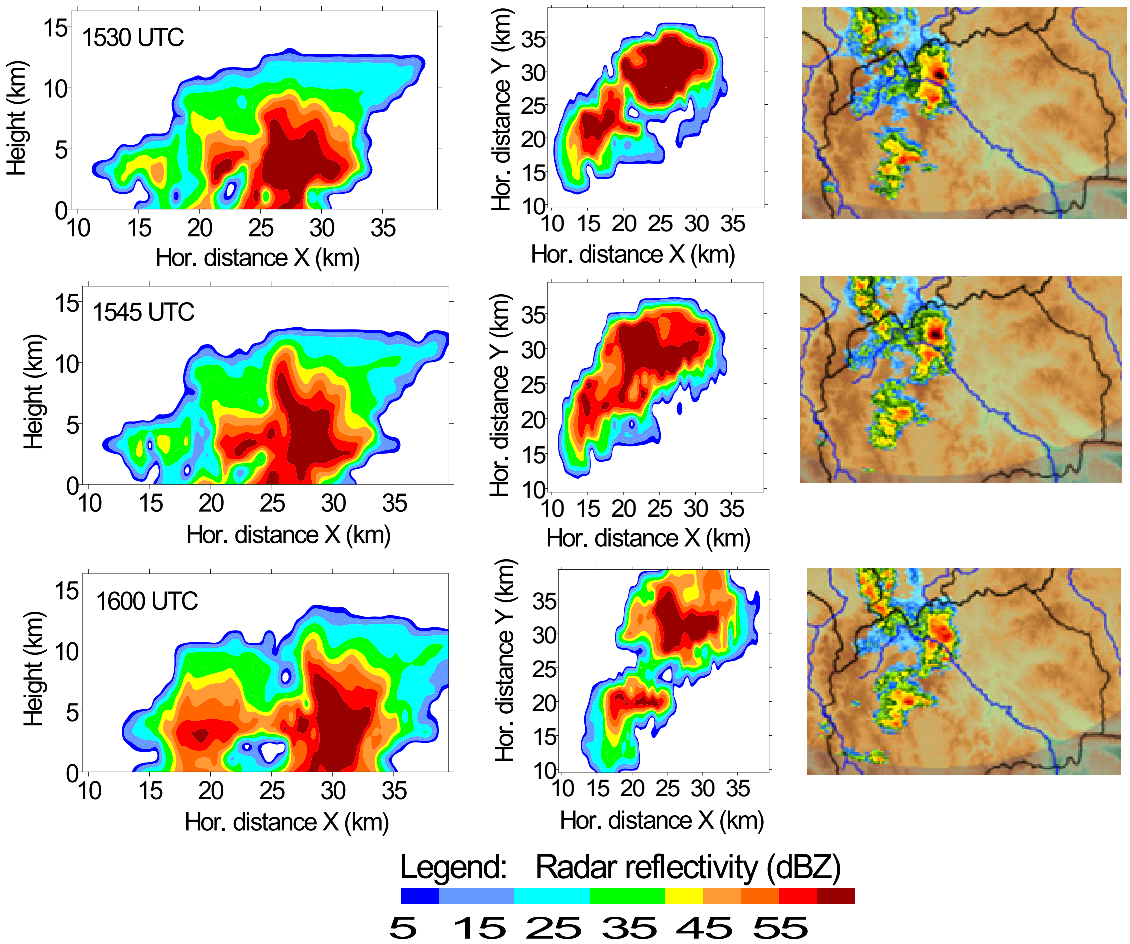

Figure 7. (1st column) Vertical cross-sections of simulated radar reflectivity (dBZ) at 1530 UTC, 1545 UTC, and 1600 UTC, respectively. (2nd column) Same as Figure 7a, but for the horizontal transects at 2.0 km height along NW-SE. (3rd -column) Same as Figure 7a, but with 2.0 km height -CAPPI composite radar image (dBZ). Source: Republic Hydrometeorological Institute of Serbia (RHIS)

fluxes. The anvil in the upper part of the cloud is visible. The intensity of a supercell storm.

A significant amount of rainfall with the torrential flash flood was evidenced on 6 August 2016 in the city of Skopje, and northeast in the surrounding rural parts in the vicinity of the mountain complex "Skopska Crna Gora" (SCG). From the isohyet chart (Figure 2a) it is evident that most of the accumulated precipitation is recorded in Skopje at the Automated Weather Station (AWS)- "Gazi Baba" with a total amount of 106.0 mm/24 hours and the maximum rainfall intensity of 36.0 mm/hour at 1545 UTC. Details about the rainfall intensity were discussed in the observational section. However, is well to mention that over the area of Skopje about 100 mm of rainfall has been evidenced, within two hours, which is twice the average amount of rain for all month of August, according to climate statistics. The WRF-10 km run (domain 1) produced rainfall close to the target area (Figure 9a), while the total amount was underestimated. The simulation with a finer resolution of 3.3 km (nested domain 2) showed better results in terms of not only the total amount of precipitation, but also in the detection of two precipitation zones, the first one positioned southwest of Skopje with a total amount of about 80 mm, which is a slight deviation from the measured values, and another heavy rainfall area shifted to the NE, from the location of the flash flood with a total rainfall of about 90 mm. Finally, the WRF 1.1-km run quite successfully simulates a convective system and cores with intense precipitation, one positioned SW from the Skopje valley. The heavy rainfall zone of about 90-100 mm/24 hrs. is positioned northeast in the vicinity of the border with Serbia.

WRF 1.1-km nested run with explicit microphysics and without parameterization of convection, produced a more total accumulated rainfall closer to the most affected flood area but underestimated the observed amount (Figure 9c). The cloud model simulation using the ensemble method (Figure 9b) indicates two distinct rainfall zones. The first

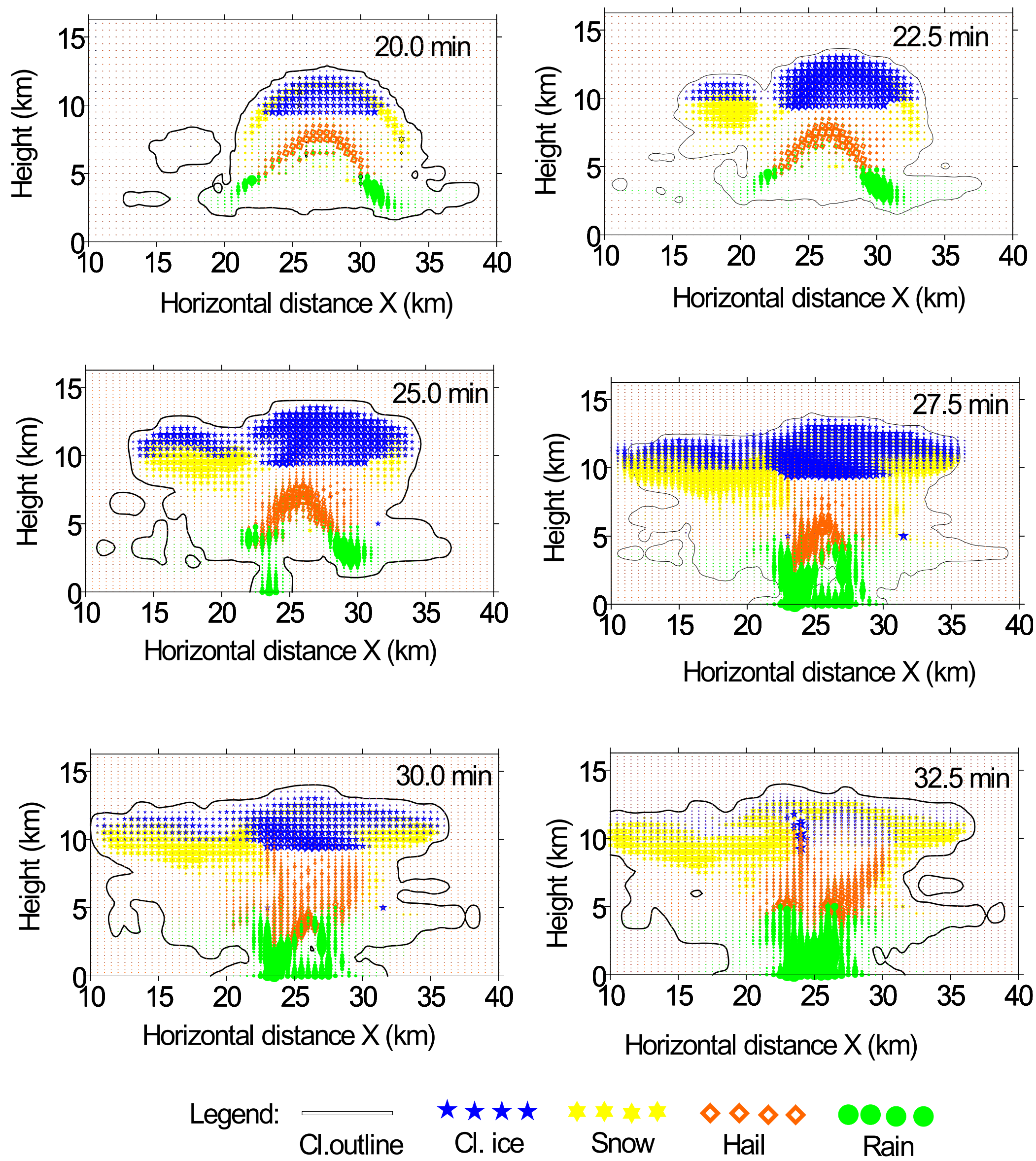

Figure 8. Vertical cross sections of micro-physical structure of the simulated super-cell storm during simulation time starting from 20.0 to 32.5 min at 2.5 min time intervals. Hydro-meteors (cloud water, cloud ice, snow, graupel or hail, and rain) are expressed through their corresponding mixing ratios (g/kg).

is distributed over the mountain "Vodno", located in the southeast part of Skopje, spreading towards the municipalities, "Gazi Baba" and "Butel". The heaviest rainfall and flash-flood occurred in the municipality of "Stajkovci", which belongs to the rural part of Skopje. The total accumulated rain averaged over the cloud model domain of about 100 mm precipitation is in good agreement with the observed pattern of heavy rainfall. The peak rainfall amount exceeds 120 mm and largely overestimates the observed peak rainfall of 106 mm at the AWS- "G.Baba". However, considering the catastrophic consequences of the flash-flood, there is a high probability that in the rural part of Skopje City and in the vicinity towards the mountainous part of SCG, where there is no coverage with meteorological observation stations, the total precipitation will be even higher.

The three-dimensional view gives a more realistic view of the structure, evolution, and strength of the super-cell storm. Cloud elements and dynamics with characteristic rotating vertical velocities are observed. The cloud hydrometeors, expressed through their mixing ratios are displayed in Figure 10 with the cloud outline mixing ratio of 0.1 g/kg. The light grey fields denote cloud water, dark gray-cloud ice, yellow snow, red hail, and green rainwater mixing ratio, respectively.

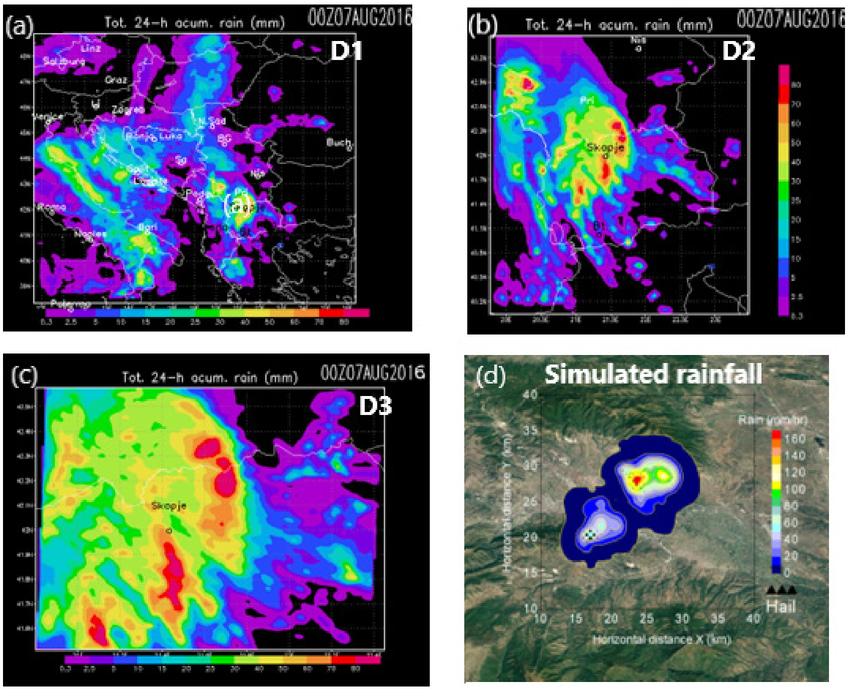

Figure 9. (a) WRF 10-km total 24 h-acc. rainfall (mm) ending at 0000 UTC 7 Aug 2016, (b) Same as 9a, but for the simulation of domain 2 (3.3-km grid) (c). WRF 1.1-km (domain 3). (d) Total simulated rainfall from 1500-1630 UTC on 6 August 2016, obtained from the cloud model simulation. The topography of the Skopje basin in 3-D is shown as a basis in the picture.

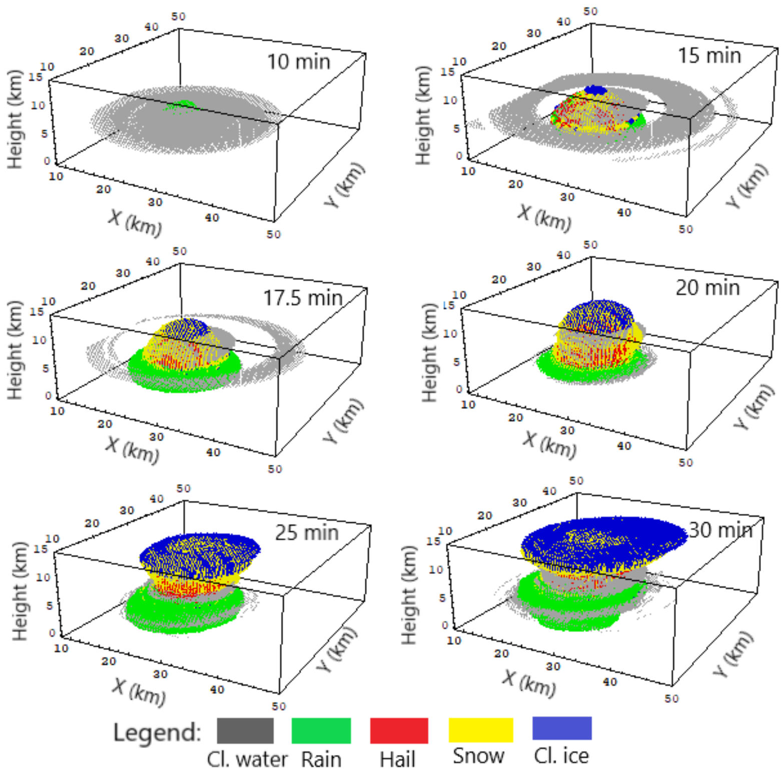

Figure 10. A three-dimensional cloud sequence of simulated storm micro-physics fields, viewed from NW-SE direction at the most intense phase of evolution, starting from 10 min simulation on 2.5 min time intervals. Hydrometeors are expressed through their mixing ratios (g/kg). The light gray fields denote cloud water, dark grey-cloud ice, yellow snow, red hail, and green rainwater. The cloud outline is 0.1 g/kg.

5. Conclusions and Discussions

The present research study is focused on the evaluation of the cloud model performances in the simulation of a deadly super-cell storm, which caused an urban flash-flooding in the Skopje valley on August 6, 2016. A new ensemble method of cloud initialization has been implemented, using WRF triple-nested model run, with hourly forecast outputs in a period of severe convection. Then the initial vertical meteorological profiles are extracted in the corresponding grid points of the selected target area (domain 3). Thus, the cloud model is run in ensemble mode with 45 members, avoiding the standard perturbation method, and minimizing the uncertainties in the initial conditions.

The WRF model reasonably simulated the initial formation of a cluster of convective clouds or Mesoscale Convective System (MCS) and its successive transition to a Mesoscale Convective Vortex (MCV), evolution over the urban area in the city of Skopje. WRF 1.1-km scale nested run showed an advantage in the simulation of a more detailed aspect of convection over the smaller domain, in a local-scale area where a flash-flood occurred. However, it failed to predict the accurate location of heavy rainfall and the relative intensity of rainfall.

A three-dimensional cloud model (3-D) simulation using the ensemble method, showed the ability to simulate the initiation of individual convective cells, persistent rotating updrafts, downdrafts, and formation of the mesocyclone. The cloud micro-physics associated with the production of large water content, cloud ice structure, transfer, and transformation processes responsible for intense rainfall fluxes and heavy torrential downpours are reproduced well. The simulated horizontal cross-section of the radar reflectivity fields, indicated a hook echo while the vertical transects of reflectivity showed a bow echo region as typical signatures for the development of a super-cell storm. As a summary of this research, it can be pointed out that the cloud model with a fine resolution successfully solves small-scale convective processes, which are significant not only from the aspect of dynamics and the initiation of a super-cell storm but also for micro-physics, which was crucial for the occurrence of extreme rainfall in a smaller urban area caused a catastrophic local-scale urban flooding. The initialization of the model using the ensemble approach enabled the development of the storm in perturbed atmospheric conditions, which gave an improvement to a far more realistic simulation of the storm, which was also shown by radar measurements, as well as data on extreme precipitation in the Skopje area. We believe that the first experiment with this ensemble approach showed certain advantages compared to the standard method, but we are not yet able to give a subjective assessment of the success of this method because more cases are needed to verify the real-time ensemble Cloud Resolving Model (CRM) applications to forecasting severe thunderstorms and to improve the reliability of this tool and use it in the context of very short-range forecasting (now-casting) and severe convective weather warning.

Conflict of Interest

There is no conflict of interest.

References

[1] Skamarock, W. C., Klemp, J. B., Dudhia, J., et al., 2005. A description of the advanced research WRF version 2 (No. NCAR/TN-468+STR). University Corporation for Atmospheric Research. DOI: 10.5065/D6DZ069T.

[2] Zheng, Y., Xue, M., Li, B., et al., 2016. Spatial characteristics of extreme rainfall over China with hourly through 24-hour accumulation periods based on national-level hourly rain gauge data. Advances in Atmospheric Sciences. 33, 1218–1232. https://doi.org/10.1007/s00376-016-6128-5.

[3] Weisman, M. L., Klemp J. B., Rotunno, R, 1988. Structure and evolution of numerically simulated squall lines. Journal of the Atmospheric Sciences. 45, 1990–2013.

[4] Skamarock, W. C., Weisman M. L., Klemp J. B., 1994. Three-dimensional evolution of simulated long-lived squall lines. Journal of the Atmospheric Sciences. 51, 2563–2584.

[5] Droegemaier, K. K. G., Bassett, D. K., Lilly, et al., 1994. Very high resolution, uniform grid simulations of deep convection on a massively parallel processor: Implications for small-scale predictability. Preprints, Tenth Conf. on Numerical Weather Prediction, Portland, OR, American. Meteorological Society. 376–379.

[6] Bernadet, L. R., Grasso L. D., Nachamkin J. E., et al, 2000. Simulating convective events using a high-resolution mesoscale model. Journal of Geophysical Research. 105(14), 963–982.

[7] Kuo, Y.H., Wang, W., Zhang, Q. et al., 2001. High-resolution simulation of Hurricane Danny (1997): Comparison with radar observations. Preprints, 11th PSU/NCAR Mesoscale Modelling System Workshop, Boulder, CO, PSU/NCAR, 94–97.

[8] Petch, J. C, Brown, A. R., Gray, M. E. B., 2002. The impact of horizontal resolution on the simulations of

convective development over land. 128, 2031–2044.

[9] Done, J., Davis, C. A., Weisman, M. L, 2004. The next generation of NWP: Explicit forecasts of convection using the weather research and forecast (WRF-NMM) model. Atmospheric Science Letter. 5, 110–117. DOI: 10.1002/asl.72.

[10] Levit, J.J., Baldwin, M. E., Bright, D. R. 2006. Examination of convective allowing configurations of the WRF-NMM model for the prediction of severe convective weather: The SPC/NSSL spring program 2004. Weather and Forecasting. 21, 167–181.

[11] Kain, J. S., Weiss, S. J., Levit, J. J., et al., 2006. Examination of convection-allowing configurations of the WRF-NMM model for the prediction of severe convective weather: The SPC/NSSL spring program 2004. Weather and Forecasting. 21, 167–181.

[12] Janjic, Z., Black, T., Pyle, M., et al., High-resolution applications of the WRF-NMM. Preprints, 21st conference on weather analysis and forecasting/17th conference on numerical weather prediction, American. 2005. Meteorological Society, Washington, DC. CD-ROM. 16A.4.

[13] Skamarock, W. C., Klemp, J. B., Dudhia, J., et al., 2008. A description of the advanced research WRF version 3 (No. NCAR/TN-475+STR). University Corporation for Atmospheric Research. DOI:10.5065/D68S4MVH.

[14] Klemp, J. B., 2006. Advances in the WRF model for convection-resolving forecasting, and advances in geosciences. 7, 25–29. https://doi.org/10.5194/adgeo-7-25-2006.

[15] Weisman, M. L., Davis C., Wang, W., et al. 2008. Experiences with 0-36h explicit convective forecasts with the WRF-ARW model. Weather and Forecasting. 23, 407–437.

[16] Brooks, H. E., Doswell C. A., Maddox, R. A., 1992. On the use of mesoscale and cloud-scale models in operational forecasting. Weather and Forecasting. 7, 120–132.

[17] Brooks, H. E., Doswell C. A., 1993. New technology and numerical weather prediction—A wasted opportunity? Weather. 48, 173–177.

[18] Zhang, F. C., Snyder, Rotunno, R., 2003. Effects of moist convection on mesoscale predictability. Journal of the Atmospheric Sciences. 60, 1173–1185.

[19] Bryan, G. H., Rotunno, R., Statistical convergence in simulated moist unstable layers. Preprints, 11th Conf. on mesoscale processes, Albuquerque, NM, American. 2005. Meteorological Society. CD-ROM 1M.6.

[20] Petch, J. C., 2006. Sensitivity studies of developing convection in a cloud-resolving model. Quarterly Journal of the Royal Meteorological Society. 132, 345–358.

[21] Xue, M. F., Kong, K. W., Thomas, J., et al., CAPS real-time storm-scale ensemble and high-resolution forecasts as part of the NOAA hazardous weather testbed 2008 spring experiment. 2008. Preprints, 24th Conference on Severe Local Storms, American Meteorological Society, Savannah, GA. CD-ROM 12.2

[22] Xue, M., Droegemeier, K. K., Wong, V., 2000. The advanced regional prediction system (ARPS): A multi-scale nonhydrostatic atmospheric simulation and prediction model. Part I: Model dynamics and verification. Meteorology and Atmospheric Physics. 75, 161-193.

[23] Elmore, K.L., Stensrud, D.J, Crawford, K.C., 2002. Ensemble cloud model applications to forecasting Thunderstorms. J. Applied Meteorology and Climatology. 41, 363-383. DOI: https://doi.org/10.1175/1520-0450(2002)041<0363: ECMATF>2.0.CO;2

[24] Stein, J., Richard, E., Lafore, J., et al. 2000. High-resolution non-hydrostatic simulations of flash-flood episodes with grid-nesting and ice-phase parameterization. Meteorology and Atmospheric Physics. 72, 203–221. https://doi.org/10.1007/s007030050016

[25] Hong, S., Y., Lee, J., 2009. Assessment of the WRF model in reproducing a flash-flood heavy rainfall event over Korea. Atmospheric Research. 93, 818-831. 10.1016/j.atmosres.2009.03.015.

[26] Shin, H., Hong, S., Y., 2009. Quantitative precipitation forecast experiments of heavy rainfall over Jeju Island on 14-16 September 2007 using the WRF model. Asia-Pacific Journal of the Atmospheric Sciences. 45, 71-89.

[27] Schwartz, C., Glen, R., Ryan, S., et al., 2015. NCAR's experimental real-time convection-allowing ensemble prediction system. Weather and Forecasting. 30. DOI: 150904135422005. 10.1175/WAF-D-15-0103.1.

[28] Zittis, George, Bruggeman, et al. 2017. The added value of convection-permitting simulations of extreme precipitation events over the eastern Mediterranean. Atmospheric Research. 191. DOI: 10.1016/j.atmosres.2017.03.002.

[29] Yano, J. I., Ziemiański, M. Z, Cullen M, et al. 2017. Scientific challenges of convective-scale numerical weather prediction. Bulletin of the American Meteorological Society. 99(4), 699–710.

[30] Spiridonov, V., Baez, J., Telenta, B. et al., 2020. Prediction of extreme convective rainfall intensities using a free-running 3-D sub-km-scale cloud mod-

el initialized from WRF km-scale NWP forecasts. Journal of Atmospheric and Solar-Terrestrial Physics. 209, 105–401. 10.1016/j.jastp.2020.105401.

[31] Spiridonov, V., Curic, M., Sladic, N., et al. 2021. Novel thunderstorm alert system (NOTHAS). Asia-Pacific Journal of Atmospheric Sciences. 57, 479–498. https://doi.org/10.1007/s13143-020-00210-5

[32] Milevski, I. 2017. Natural hazards in the Republic of Macedonia, with special emphasis on flood and earthquake in Skopje in 2016. Geographical Reviews. 50, 5-22

[33] Blinkov I., Trendafilov, A., Mincev, I., 2016. Rapid diagnostic of the catastrophic event happened on 6th August 2016 in the Skopje region – initial findings. The third world conference of World Association of Soil and Water Conservation - New challenges and strategies of soil and water conservation in the changing world sustainable management of soil and water resources, August 22-26, 2016, Belgrade/Serbia; https://www.researchgate.net/publication/348971728_RAPID_DIAGNOSTIC_OF_THE_CATASTROPHIC_EVENT_HAPPENED_ON_6_TH_AUGUST_2016_IN_THE_SKOPJE_REGION

[34] Klemp, J. B., Wilhelmson, R. B., 1978. The simulation of three-dimensional convective storm dynamics. Journal of the Atmospheric Sciences. 35, 1070–1096.

[35] Orville, H. D., Kopp, F. J., 1977. Numerical simulation of the history of a hailstorm. Journal of the Atmospheric Sciences. 34, 1596–1618.

[36] Lin, Y. L., Farley, R. D., Orville, H. D., 1983. Bulk water parameterization in a cloud model. Journal of Climate and Applied Meteorology. 22, 1065–1092.

[37] Thompson, G., Field, P.R., Rasmussen, R. M., et al., 2008. Explicit forecasts of winter precipitation using an improved bulk microphysics scheme. Part II: Implementation of a new snow parameterization. Monthly weather review. 136, 5095–5115

[38] Thompson, G. T., Eidhammer, 2014. A study of aerosol impacts on clouds and precipitation development in a large winter cyclone. Journal of the Atmospheric Sciences. https://doi.org/10.1175/JAS-D-13-0305.1

[39] Hong, S. Y., 2010. A new stable boundary-layer mixing scheme and its impact on the simulated East Asia summer monsoon. Quarterly Journal of the Royal Meteorological Society. 136(651), 1481-1496. DOI: 10.1002/qj.665

[40] Chen, F., Dudhia, J., 2001. Coupling an advanced land surface–hydrology model with the penn state–ncar mm5 modelling system. Part 1: Model implementation and

sensitivity. Monthly Weather Review. 129, 569–585. https://doi.org/10.1175/1520-0493 (2001)129<0569:CAALSH>2.0.CO;2.

[41] Shin, H., Hong, S.Y., 2015. Representation on the subgrid-scale turbulent transport in convective boundary layers at grey-zone resolutions. Monthly Weather Review. 143, 250-271.

[42] Han, J.Y., Hong, S.Y., 2018. Precipitation forecast experiments using the weather research and forecasting (WRF) model at gray-zone resolutions. Weather and Forecasting. 33, 1605-1616. DOI: https://doi.org/10.1175/WAF-D-18-0026.1

[43] Mlawer, Eli, Taubman, et al., 1997. Radiative transfer for inhomogeneous atmospheres: RRTM, A validated correlated-k model for the longwave. Journal of Geophysical Research. 102, 16663-16682. DOI: 10.1029/97JD00237.

[44] Dudhia, J., 1989. Numerical study of convection observed during the winter monsoon experiment using a mesoscale two-dimensional model. Journal of the Atmospheric Sciences. 46, 3077–3107

BILINGUAL PUBLISHING CO.
Pioneer of Global Academics Since 1984

Tel.:+65 65881289
E-mail: contact@bilpublishing.com
Website:ojs.bilpublishing.com

2630-5119